

Utilization of Surface enhanced Raman scattering in biomolecular detection and characterization

A Thesis

Submitted for the Degree of
DOCTOR OF PHILOSOPHY

by

G.V. PAVAN KUMAR



CHEMISTRY AND PHYSICS OF MATERIALS UNIT
JAWAHARLAL NEHRU CENTRE FOR ADVANCED SCIENTIFIC
RESEARCH

(A Deemed University)

Bangalore – 560 064

APRIL 2008

*To my inspiration, **Enrico Fermi***

DECLARATION

I hereby declare that the matter embodied in the thesis entitled “**Utilization of Surface enhanced Raman scattering in biomolecular detection and characterization**” is the result of investigations carried out by me at the Chemistry and Physics of Materials Unit, Jawaharlal Nehru Centre for Advanced Scientific Research, Bangalore, India under the supervision of Prof. Chandrabhas Narayana and that it has not been submitted elsewhere for the award of any degree or diploma.

In keeping with the general practice in reporting scientific observations, due acknowledgment has been made whenever the work described is based on the findings of other investigators.

G.V. Pavan Kumar

CERTIFICATE

I hereby certify that the matter embodied in this thesis entitled “**Utilization of Surface enhanced Raman scattering in biomolecular detection and characterization**” has been carried out by Mr. G.V. Pavan Kumar at the Chemistry and Physics of Materials Unit, Jawaharlal Nehru Centre for Advanced Scientific Research, Bangalore, India under my supervision and that it has not been submitted elsewhere for the award of any degree or diploma.

Prof. Chandrabhas Narayana
(Research Supervisor)

Acknowledgments

It is my great pleasure to acknowledge the people with whom I shared my intellectual excitement during my Ph.D. at JNCASR.

I would start with Prof. Chandrabhas Narayana (fondly called as Bhas) for being one of the most friendly research supervisor one could ask for. His amazing knowledge of optical instrumentation: design and construction, has always awed me to great extent. If at all I have learnt some *art of optical design*, then I owe it to Bhas. Our journey of research on SERS was an adventure, and Bhas gave me a great amount of freedom to think and valued my ideas in this pleasant endeavor. I would cherish the memory of working with him forever.

I would like to thank the chairman of our unit, Prof.C.N.R. Rao. He has been a great source of inspiration and encouragement to science enthusiast like me. I admire his infectious enthusiasm and interest towards science.

Probably, more than two thirds of my Ph.D. life was spent with my lab-mates: Dr.Motin, Dr.Nashiour, Kavitha, Gopal, Jyothirmayee, Partha, Rangarajan, Shruthi, Vibha and Sonia. I thank them for baring my scientific curiosity and for the conducive environment they created for pursuing research in our lab.

I had very fruitful collaborations with plenty of research groups both inside and outside JNCASR. Prof.Tapas Kundu and his magnanimous group at JNCASR have played an important role in my appreciation of biology. I like the concept of

their team work and learnt a lot from them. Prof.Ranga Udaykumar and his group at JNCASR is greatly acknowledged. I learnt a lot from Ranga Sir, and I thank him for some wonderful discussion and novel ideas. I had pleasant collaborations with Prof. Kulkarni and Bhuvana of JNCASR. I thank both of them for discussion. Prof.Pradeep and Subramaniam (Subbu) of IIT-Madras are pleasantly acknowledged. In Subbu I found a like-minded friend, and enjoyed discussing both scientific and non-scientific issues with him. I would also thank Prof.Yamuna of NCBS, with whom we collaborated on DNA work. A special thanks to Mr.Arokyanathan of JNCASR machine shop. He played a crucial role in executing our optical design. I thank all the faculties of CPMU and TSU, JNCASR for sharing their knowledge during and after my first year Ph.D. course-work. I thank Prof.P.Balaram of Indian Institute of Science for his outstanding course on molecular spectroscopy. I thank Prof.Srikanth Sastry of JNCASR for his guidance and discussion. I really admire his attitude towards science.

I had a great set of batchmates in Arif(my Biology handbook), Bhuvana, Vinay, Vengandesh, Javid, Gayathri, Manu, Vijay, Bhat, Sahoo, Saswathi at JNCASR from whom I learnt a lot of science. I would like to thank Mohan P.J. for helping me with some calculations on Raman spectra.

I thank my M.Sc. classmates Vishwas, Padmanabha and Prabhu, with whom I shared and explored my passion towards Physics.

I owe a lot to my Gurus: Prof.G.Srinivasan, Prof.G.S.Ranganath (both retired Professors at Raman Research Institute, Bangalore) and Prof. G. Ramachandran (retired Professor at Indian Institute of Astrophysics, Bangalore) who inspired me to take up research as a career. I will cherish their teaching for my lifetime.

I would also like to thank all the authors of great books. Finally, I would like to thank my family members for their constant support.

Preface

This thesis stems out of the research conducted on an emerging optical spectroscopy technique called as Surface enhanced Raman scattering (SERS). One of the foremost advantages of SERS is the rich blend of high sensitivity and chemical imaging capability, which vastly caters to the needs of ultra trace analysis of molecules. We have utilized this technique not only to probe the physical properties of plasmonic core-shell nanoparticles, but also to detect and characterize some important biomolecules like p300, RNA of HIV-1, etc. By harnessing the electromagnetic and chemical enhancement mechanisms of SERS, we have been able to devise strategies to optimize the detection methodologies. Following is the overview of the thesis:

Chapter 1 provides a substantive introduction to SERS phenomenon and methodologies related to it. Chapter 2 accounts the details of the design and construction of custom-built Raman microscopy system compatible for SERS measurements. Chapter 3 is about harnessing the physical properties of core-shell nanoparticles. In the first part of this chapter, the plasmonic property of Ag core-Au shell nanoparticles have been studied with special emphasis on identifying and utilizing SERS hot spots for molecular detection. The second part of the chapter is about SERS properties of metal-coated magnetic nanoparticles. Formation of hybrid plasmonic-magnetic films by employing an external magnetic field is also detailed.

Chapter 4 deals with Raman and SERS studies of two important drug molecules: CTB and CTPB. A comprehensive vibrational mode analysis is the main theme of this chapter. Ag-N modes at low wavenumbers have been identified in SERS studies which shed light on metal-molecule interactions. Chapter 5 reports comprehensive study on SERS of human transcriptional coactivator p300, which is a 300 kDa protein. SERS has been utilized as an effective probe to understand protein-molecule interactions. Small structural changes in p300 upon autoacetylation have also been identified through SERS. Chapter 6 details one of the diagnostic applications of Surface enhanced Resonant Raman Scattering (SERRS). HIV-1 subtype detection and discrimination using SERRS has been discussed in detail. The cost effectiveness of the method has been highlighted. The thesis ends with an outlook, in which some pros and cons of SERS and future prospects of the technique are discussed.

Publications

1. *Surface Enhanced Raman Scattering Studies of Human Transcriptional Coactivator p300*
G.V. Pavan Kumar, B.A. Ashok Reddy, Md. Arif, T.K. Kundu and Chandrabhas Narayana
Journal of Physical Chemistry B 110, 16787-16792 (2006).
2. *Hot spots in Ag core-Au shell nanoparticles potent for surface enhanced Raman scattering studies of biomolecules*
G.V. Pavan Kumar, S. Sruthi, B. Vibha, B.A.A. Reddy, T.K. Kundu and Chandrabhas Narayana
Journal of Physical Chemistry C 111, 4388-4392 (2007).
3. *Adapting a fluorescence microscope to perform surface enhanced Raman spectroscopy*
G.V. Pavan Kumar and Chandrabhas Narayana
Current Science 93, 778-781 (2007).
4. *Autoacetylation induced specific structural changes in histone acetyltransferase domain of p300: Probed by Surface enhanced Raman spectroscopy*
M.Arif, **G.V. Pavan Kumar**, C. Narayana and T.K. Kundu
Journal of Physical Chemistry B lett. 111, 11877-11879 (2007).

5. *Activation of p300 histone acetyltransferase by small molecules altering enzyme structure: Probed by Surface enhanced Raman spectroscopy*
K. Mantelingu, A. H. Kishore, K. Balasubramanyam, **G.V. Pavan Kumar**, M. Altaf, S. Najundaswamy, R. Selvi, C. Das, Chandrabhas Narayana, K.S. Rangappa and T.K. Kundu
Journal of Physical Chemistry B 111, 4427-4535 (2007).
6. *Specific inhibition of p300-HAT Alters Global Gene Expression and Repress HIV replication*
K. Mantelingu, B.A.A. Reddy, V. Swaminathan, A.H. Kishore, N. B. Siddappa, **G.V. Pavan Kumar**, G. Nagashankar, N. Natesh, S. Roy, P.P. Sadhale, U. Ranga, Chandrabhas Narayana and T. K. Kundu
Chemistry & Biology 14, 645-657 (2007).
7. *Raman and SERS studies of small molecule activators of histone acetyl transferase p300*
G.V. Pavan Kumar, K. Mantelingu, P.J.Mohan, K. Balasubramanyam, T.K. Kundu, C. Narayana
submitted(2007).
8. *Metal-coated magnetic nanoparticles for SERS applications*
G.V. Pavan Kumar, N. Rangarajan, N. Rohmon, Chandrabhas Narayana
submitted(2007).
9. *A high sensitivity assay for molecular typing of biological samples using Surface enhanced Raman scattering*
Indian Patent applied (2007).

Other miscellaneous publications:

1. *Visible fluorescence induced by metal-semiconductor transition in composites of carbon nanotubes with noble metal nanoparticles*
C. Subramaniam, T.S. Sreepad, T. Pradeep, **G.V. Pavan Kumar**, Chandrabhas Narayana, T.Yajima, Y.Sugawara, H. Tanaka, T. Ogawa, J.Chakrabarti
Physical Review Letters 99, 167404-167407(2007).
2. *The I-tetraplex building block: Rational Design and Controlled Fabrication of robust 1D DNA Scaffolds via non-Watson Crick self assembly*
H. B. Ghodke, R. Krishnan, K. Vignesh, **G.V. Pavan Kumar**, Chandrabhas Narayana and Y. Krishnan
Angewandte Chemie (International Edition) 46, 2646-2649 (2007).
3. *Carbon assisted electroless gold for Surface enhanced Raman scattering studies.*
T. Bhuvana, **G.V. Pavan Kumar**, G.U. Kulkarni and Chandrabhas Narayana
Journal of Physical Chemistry C 111, 6700-6705 (2007).
4. *Nanogranular Au films deposited on carbon covered Si substrates for enhanced optical reflectivity and Raman scattering*
T. Bhuvana, **G.V. Pavan Kumar**, Chandrabhas Narayana and G.U.Kulkarni
Nanotechnology 18, 145702 (2007).

Contents

Preface	vii
1 Introduction	1
1.1 Raman scattering	2
1.1.1 Quantum picture of Raman scattering	4
1.1.2 Resonant Raman scattering	8
1.2 Surface Enhanced Raman Scattering (SERS)	8
1.2.1 Electromagnetic enhancement mechanism	10
1.2.2 Chemical enhancement mechanism	11
1.2.3 Experimental calculation of SERS enhancement factor-G . .	14
1.2.4 Surface selection rules of SERS	16
1.3 Nanoparticles for SERS studies	19
1.4 Applications of SERS in biodetection	21
1.5 Role of atomic scale roughness in SERS	22
2 Adapting a Fluorescence Microscope to Perform Surface Enhanced Raman Spectroscopy	25
2.1 Motivation	26
2.2 Fabrication of SERS microscope	26

2.3	Performance of the constructed microscope	29
2.4	Role and usage of water immersion objective lens in SERS	31
2.5	Conclusion	33
3	SERS applications of core-shell nanoparticles	35
3.1	Hot spots in Ag core - Au shell nanoparticles for SERS applications	36
3.1.1	Motivation	36
3.1.2	Experimental details	37
3.1.3	Results and Discussion	39
3.1.4	Conclusion	45
3.2	SERS applications of metal coated magnetic nanoparticles	45
3.2.1	Motivation	45
3.2.2	Preparation of metal coated magnetic nanoparticles	47
3.2.3	Sample preparation for SERS	48
3.2.4	Results and discussion	49
3.2.4.1	Surface plasmon resonance of metal-coated mag- netic nanoparticles	49
3.2.4.2	Magnetic property of metal-coated magnetic nanopar- ticles	50
3.2.4.3	SERS properties of metal-coated magnetic nanopar- ticles	52
3.2.4.4	Temperature dependent SERS using Fe ₂ O ₃ @Ag . .	53
3.2.5	Conclusion	55
3.3	Gold-coated Fe ₂ O ₃ nanoparticular films	55
3.3.1	Motivation	55
3.3.2	Experimental details	56

3.3.3	Results and Discussion	57
3.3.3.1	Formation of Fe ₂ O ₃ @Au thin film in the presence of magnetic field	57
3.3.3.2	Magnetic and SERS property of Fe ₂ O ₃ @Au thin films	58
3.3.3.3	Magnetic field assisted alignment and rotation of Fe ₂ O ₃ @Au aggregates in solution	60
3.3.4	Conclusion	64
4	Raman and surface enhanced Raman spectroscopic studies of ac- tinator molecules of histone acetyltransferase p300	65
4.1	Motivation	66
4.2	Experimental details	67
4.3	Results and Discussion	69
4.3.1	Raman and SERS spectra of CTB	69
4.3.1.1	Vibrations of N-H group	70
4.3.1.2	Vibrations of methyl, methylene and C-H group	72
4.3.1.3	Vibrations of benzene ring C=C group	72
4.3.1.4	Amide I vibration	73
4.3.1.5	Vibrations of carbon-halogen bonds	73
4.3.2	Raman and SERS spectra of CTPB	74
4.4	Conclusion	76
5	SERS studies of human transcriptional co-activator p300 and its active domain	79
5.1	Motivation	81
5.2	SERS of p300	83
5.2.1	Experimental details	83

5.2.1.1	Processing of p300 for SERS studies	83
5.2.1.2	Sample preparation for SERS measurements	84
5.2.2	Results and Discussion	86
5.2.2.1	SERS Spectra of p300 in the solution phase	86
5.2.2.2	Chloride ion effect on SERS Spectra of p300	93
5.2.2.3	SERS Spectra of p300 adsorbed to silver nanoparticles dried over a glass substrate	95
5.2.3	Conclusions	96
5.3	Interaction of p300 with small molecules: Probed by SERS	97
5.3.1	Experimental Details	99
5.3.2	Results and Discussion	100
5.3.2.1	Interaction of p300 with activator molecules	100
5.3.2.2	Interaction of p300 with inhibitor molecules	104
5.3.3	Conclusion	108
5.4	Structural changes in p300 HAT domain: probed by SERS	109
5.4.1	Experimental details	110
5.4.2	Results and Discussion	110
5.4.3	Conclusion	114
6	Diagnostic application of SERRS: Detection and discrimination of HIV-1 subtypes	115
6.1	Motivation	116
6.2	Experimental details	118
6.3	Results and Discussion	121
6.4	Conclusions	124

7 Outlook	127
7.1 Fundamental issues	128
References	131

CHAPTER 1

INTRODUCTION

At the onset of twenty first century, molecular spectroscopy has been rejuvenated by the advances in various fields like optical instrumentation, nanoscience and biotechnology. By employing various spectroscopic techniques, rapid progress has been achieved in understanding molecules and unveiling their interactions. Molecular detection and characterization techniques have evolved as one of the most active research areas in science with a huge bandwidth of applications - from biology to astronomy.

Depending upon the energy scales probed, molecular spectroscopy can be mainly classified into three different categories: Electronic, vibrational and rotational spectroscopy. The electronic spectroscopy investigates the electronic energy states of a molecule, which can be probed by ultraviolet or visible radiation. The vibrational energy states can be probed either by infrared radiation or Raman scattering. The rotational energy states can be probed by microwave radiation. Lasers have the ability to produce monochromatic photons with a high degree of spatial and temporal coherence, and hence play a major role in the above mentioned spectroscopic techniques.

Of the various techniques used to probe molecules, vibrational spectroscopy has emerged as an effective method to study structure and dynamics of molecules, irrespective of the environment in which molecules are present. Every molecule has a characteristic vibrational spectrum which can be used as their finger prints.

This facilitates an advantage in molecular detection, sensing and characterization. Though both Infra-red spectroscopy and Raman scattering probe the vibrational states of a molecule, we employ the latter as a molecular probe, and is described in detail.

1.1 Raman scattering

When photons are incident on molecules, there are various energy pathways for the molecules to be excited. Due to this excitation, the electrons in the molecule make transition from their ground state to an excited state. This excited state has a finite life time, and hence the molecules relax back to their ground state by emitting photons. This emitted photons can be a resultant of either an elastic or an inelastic interaction between the photons and molecular vibration (vibrons/phonons). The former is generally categorized as Rayleigh scattering, and the latter may be due various interactions between photons and vibrational states of a molecule, where exchange of energy between them is prevalent. One such interaction which is essentially due to an inelastic scattering mechanism is called as Raman scattering. In Raman scattering, the photons can either gain or lose energy upon interaction with vibrational energy states of a molecule. The Raman scattered radiation is classified either as Stokes or anti-Stokes radiation depending on whether the photon has lost or gained energy, respectively. In 1928, Sir C. V. Raman and K. S. Krishnan experimentally discovered the Raman Effect [1]. Sir C.V. Raman went on to win the Nobel Prize in 1930 for this discovery.

When a molecule is placed in a static electric field \vec{E} , the positively charged nuclei and the negatively charged electrons are spatially distorted. The molecule is now polarized and the separation of charges create an induced dipole moment,

\vec{P} . The induced dipole moment of a molecule depends upon the applied electric field [2], and is given by the relation

$$\vec{P} = \tilde{\alpha} \cdot \vec{E}; \quad (1.1)$$

where $\tilde{\alpha}$ is the polarizability of the molecule. In its general form, both \vec{P} and \vec{E} are three dimensional vectors; so $\tilde{\alpha}$ can be expressed as a tensor, whose components can be represented as elements of a matrix. The general form of Eq. 1.1 is given by

$$\begin{bmatrix} P_x \\ P_y \\ P_z \end{bmatrix} = \begin{bmatrix} \alpha_{xx} & \alpha_{xy} & \alpha_{xz} \\ \alpha_{yx} & \alpha_{yy} & \alpha_{yz} \\ \alpha_{zx} & \alpha_{zy} & \alpha_{zz} \end{bmatrix} \begin{bmatrix} E_x \\ E_y \\ E_z \end{bmatrix} \quad (1.2)$$

Now, consider molecules subjected to electromagnetic radiation of frequency ν with an oscillatory magnitude of electric field given by

$$E = E_0 \sin 2\pi\nu t \quad (1.3)$$

This results in an oscillatory induced dipole moment whose magnitude is given by

$$P = \tilde{\alpha} \cdot \vec{E} = \alpha E_0 \sin 2\pi\nu t \quad (1.4)$$

This oscillation in dipole moment leads to secondary radiation, which is termed as Rayleigh scattering, and represents the elastic scattering component. Since the molecules have internal degrees of freedom like vibration or rotation which modulate the polarizability periodically, the oscillating dipole will be a superposition of varying electric field and polarizability. In such a case, the magnitude of polariz-

ability vector is given by

$$\alpha = \alpha_0 + \beta \sin 2\pi\nu_{vib}t; \quad (1.5)$$

where α_0 is the equilibrium polarizability, β is the rate of change of polarizability and ν_{vib} is the vibrational frequency of the molecule. In such a situation, the induced dipole moment is given by

$$P = \alpha E_0 \sin 2\pi\nu t + \frac{1}{2}\beta E_0 \{\cos 2\pi(\nu - \nu_{vib}) - \cos 2\pi(\nu + \nu_{vib})\} \quad (1.6)$$

Equation 1.6 indicates that the oscillating dipole has three frequency components, ν , $\nu - \nu_{vib}$ and $\nu + \nu_{vib}$. The component $\nu - \nu_{vib}$ and $\nu + \nu_{vib}$ are called as Stokes and anti-Stokes line, respectively. They represent the inelastically scattered components of the scattered radiation. It should be noted that if the vibration does not alter the polarizability of a molecule, then $\beta = 0$, and the dipole moment oscillates only with frequency of incident radiation. Therefore, for a vibrational mode to be Raman active, change in the component of molecular polarizability is a prerequisite.

1.1.1 Quantum picture of Raman scattering

Although classical theory of Raman scattering explains the origin of Stokes and anti-Stokes lines, they do not account for their differences in intensity. According to the basic principles of quantum mechanics, the energy associated with electronic, vibrational and rotational degrees of freedom of a molecule can assume values only from a discrete set, namely the quantized energy levels corresponding to the possible stationary states of the molecule. These states are characterized by a specific set of quantum numbers describing the level of excitation of each quantized degree of freedom, and by a corresponding wavefunction. In infrared absorption or

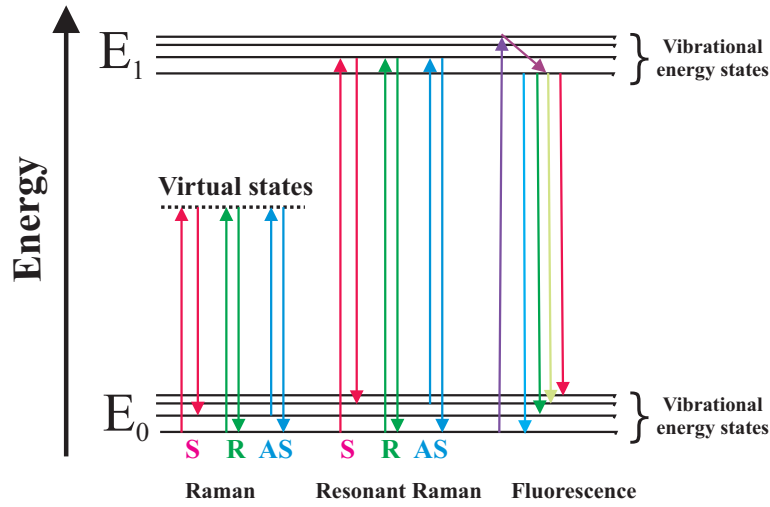


Figure 1.1: Energy level diagram comparing Raman, resonant Raman scattering and Fluorescence

emission, there is a direct transition between vibrational energy levels, most often between the vibrational ground state and the first excited state. In contrast to this, both Rayleigh and Raman scattering involve two, almost simultaneous transitions proceeding via virtual states in which one photon of the incident radiation is absorbed and another photon, either of the same energy (Rayleigh scattering) or of lower energy (Stokes Raman) or high energy (anti-Stokes Raman) is emitted.

Figure 1.1 shows a schematic of the energy levels involved in the process. Here, the virtual state refers to a transition state which does not correspond to an eigenstate of the molecule; so it is only an imaginary state, a practical convenience by which the energy exchange between the radiation field and the molecule during the scattering process can be split up into two one-photon transitions. To refine the classical description of Raman scattering, we can use partial quantum mechanical treatment in which molecule is treated quantum mechanically and radiation classically. Then for the description of the interaction of light with matter, electromagnetic radiation is treated as a source of perturbation of the molecular system.

Any direct transition between two energy levels is accompanied by emission or absorption of radiation if the dipole moment of the transition (which is called as the transition moment) is nonzero. The amplitude concerning a transition from an initial state i to a final state f induced by radiation of wavenumber $\tilde{\nu}_0$ is given as:

$$[\mu]_{fi} = \langle \psi_f | \alpha | \psi_i \rangle \cdot E; \quad (1.7)$$

where ψ_f and ψ_i are the wavefunctions of the initial and the final states respectively. The intensity of Raman scattered radiation will be determined by the properties of the transition polarizability tensor, whose components represent the matrix elements of transition from the state f to i . By neglecting electrical and mechanical anharmonicity, and exploiting the properties of the harmonic oscillator wavefunctions, we can realize that only those matrix elements differ from zero for which one vibrational quantum number changes by unity and all the other vibrational quantum numbers remain unchanged. Then for a typical matrix element of the transition polarizability associated with Stokes Raman scattering at Raman shift we obtain,

$$[\alpha_{xy}] = b\beta\sqrt{v+1}; \quad (1.8)$$

where v is the vibrational quantum number and $b = \hbar/(4\pi c\tilde{\nu})$, is the quantum mechanical analog of the amplitude of a classical oscillator. It is clear from the Eq. 1.7 that for such a transitions to be Raman active, it is also required that at least one component of the derived polarizability tensor be non zero, just as in classical theory. A very significant difference between the classical and quantum mechanical treatments is that in the latter there is a dependence on the quantum number, which has important consequences concerning the intensities of Raman scattering. When we consider scattering from an assembly of N molecules, the

initial distribution of molecules among the vibrational states at temperature T must be taken into account to establish the fraction of molecules capable of a given transition. This leads us to an important quantity which is the ratio of intensities with respect to Stokes to anti-Stokes line given by,

$$\frac{I_{Stokes}}{I_{anti-Stokes}} = \left(\frac{\tilde{\nu}_0 - \tilde{\nu}_k}{\tilde{\nu}_0 + \tilde{\nu}_k} \right)^4 \exp\left(\frac{hc\tilde{\nu}}{kT}\right) \quad (1.9)$$

In addition to correctly accounting for the observed intensity relationships, this equation allows one to determine the sample temperature, provided the measured Raman intensities are corrected for instrument response. Another important concept in Raman scattering is the Raman cross section which represents the scattering cross sectional area of a molecule interacting with the incident radiation [2]. The general expression for Raman cross section is as follows:

$$\sigma(i \rightarrow f) = \frac{8\pi\omega_s^4}{9\hbar c^4} \left| \sum_j \left(\frac{\langle \alpha_{ij} \rangle \hat{e}_L \langle \alpha_{jf} \rangle \hat{e}_s}{\omega_{ij} - \omega_L - i\gamma_L} + \frac{\langle \alpha_{ji} \rangle \hat{e}_L \langle \alpha_{ff} \rangle \hat{e}_s}{\omega_{jf} - \omega_L - i\gamma_j} \right) \right|^4; \quad (1.10)$$

where \hat{e}_L and \hat{e}_s are unit vectors representing the polarization of the incident laser beam and the scattered light. The sum extends over all molecular levels j with homogeneous width γ , accessible by single-photon transitions from the initial state. We see from Eq. 1.10 that the initial and final states are connected by two-photon transitions, which implies that both states have the same parity. It is interesting to note that the vibrational transitions in homo-nuclear diatomic molecules, which are forbidden for single-photon infrared transitions, are accessible to Raman transitions.

1.1.2 Resonant Raman scattering

The scattering cross section of a molecule can be increased by a few orders of magnitude when the Raman excitation frequency is in resonance with one of the electronic transitions (see Fig. 1.1) of the molecule [2]. In such a situation, the denominator of Eq. 1.10 reduces to a very small value, and several terms in the sum give large contribution to the signal intensity of the scattered light. This effect is generally called as Resonant Raman scattering. Unlike the non-resonant case, in resonance Raman scattering a larger number of Raman lines may appear that are shifted against the excitation line by several vibrational quanta. They correspond to Raman transitions terminating on higher vibrational levels of the ground electronic state. This is quite similar to laser-excited fluorescence [3], and opens the possibility to determine the anharmonicity constants of the molecular potential curve or potential surface of the lower electronic state [4]. Resonance Raman scattering is particularly advantageous for molecules with chromophores and samples with small densities [4, 5], for example, gases at low pressures, where the absorption of the incident radiation is not severe and where non-resonant Raman spectroscopy might not be sufficiently sensitive.

1.2 Surface Enhanced Raman Scattering (SERS)

Upon adsorption of molecules on metallic nano-surfaces exhibiting nanoscale roughness, the Raman signal intensity of the molecule is enhanced by many orders of magnitude. This phenomenon is called as Surface enhanced Raman scattering (SERS) [6, 7]. It was first observed by Fleischmann et al. [8] in 1974, and later, correctly interpreted by couple of groups in 1977 [9, 10]. Earlier to the

discovery of SERS, laser Raman scattering was not an ideal candidate to study vibration spectroscopy of molecules at low concentrations because the Raman cross section was too small when compared to other optical processes of a molecule. In a situation where a fluorescent molecule is under Raman scattering study, there is always a possibility that the Raman signal being masked due to the fluorescent background. This is because the non-resonant Raman cross section of a molecule is around 10^{-29} cm² per molecule, whereas the fluorescence cross section of molecule is around 10^{-17} cm² per molecule [11]. All these reasons had hampered the usage of Raman scattering for ultra trace analysis of molecules. SERS has the ability to circumvent this problem because the Raman cross section is no more the same as that for the conventional Raman scattering, but would be drastically changed to values comparable to Fluorescence [12]. Since its discovery, this enhanced Raman cross section in SERS has been harnessed as a tool for ultra trace analysis of molecules [13–20].

It is important to unveil the reason behind this increased cross section in SERS, as it has a significant bearing on understanding of metal-molecule interaction [21]. Since Raman intensities scale as the product of the incident field intensity and polarizability derivative, there are two commonly considered mechanisms for SERS, one of which involves enhancements in the field intensity as a result of plasmon resonance excitation [7], and the other is the enhancement in polarizability due to chemical effects such as charge-transfer excited states and formation of resonant intermediates [7]. These two important enhancement mechanisms underlying the SERS phenomenon are called as Electromagnetic and Chemical enhancement mechanisms.

1.2.1 Electromagnetic enhancement mechanism

Surface plasmons are collective oscillations of free electrons on the surface of a metal [6, 21–23]. At the near field of a metallic surface, the electric field is strong due to the plasmon resonance. Any molecule residing in the vicinity of a metallic surface is under the influence of this strong electric field [6, 21, 24].

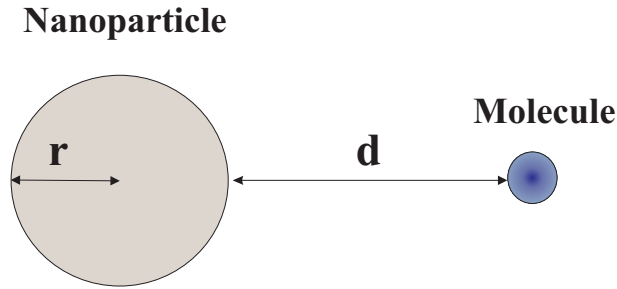


Figure 1.2: Schematic for the electromagnetic enhancement effect in SERS

Fig. 1.2 shows a simplified schematic diagram to understand the concept of electromagnetic SERS enhancement. The metallic nanostructure is a small sphere with the complex dielectric constant $\varepsilon(\nu)$ in a surrounding medium with a dielectric constant $\varepsilon(0)$. The diameter of the sphere ($2r$) is small compared with the wavelength of light (Rayleigh limit). A molecule in the vicinity of the sphere at a distance d is exposed to a field E_M , which is the superposition of the incoming field and the a dipole field induced in the metal sphere. The field enhancement factor $A(\nu)$ is the ratio of the field at the position of the molecule and the incoming field. The expression for this is as follows:

$$A(\nu) = \frac{E_M(\nu)}{E(\nu)} = \frac{\varepsilon - \varepsilon_0}{\varepsilon + 2\varepsilon_0} \left(\frac{r}{r + d} \right)^3 \quad (1.11)$$

The value of $A(\nu)$ is large when the real part of ε is equal to $-2\varepsilon_0$. Additionally, for a strong electromagnetic enhancement, the imaginary part of the dielectric

constant should be small. These conditions describe the resonant excitation of surface plasmons of the metal sphere. Metals like Ag, Au and Cu satisfy the above conditions at visible wavelengths, and hence exhibit SERS properties. As in the case of laser field, the Stokes or anti-Stokes field is enhanced if it is in resonance with the surface plasmons of the metal spheres. Taking into effect the enhancement due to laser field and the Stokes field, the electromagnetic enhancement factor for the Stokes scattering is given by

$$G_{em}(\nu_s) = |A(\nu_L)|^2 |A(\nu_S)|^2 = \left| \frac{\varepsilon(\nu_L) - \varepsilon_0}{\varepsilon(\nu_L) + 2\varepsilon_0} \right|^2 \left| \frac{\varepsilon(\nu_S) - \varepsilon_0}{\varepsilon(\nu_S) + 2\varepsilon_0} \right|^2 \left(\frac{r}{r+d} \right)^{12} \quad (1.12)$$

Following are the important implications of the above equation.

- The enhancement scales as fourth power of the local field at the vicinity of the metallic nanostructure and is particularly strong when the scattered and the plasmon field are in resonance.
- The electromagnetic enhancement is a distance dependent mechanism. The enhancement decays as $(r/(r+d))^{12}$. Interestingly, it is not necessary for the molecule to be in contact with the metal surface to exhibit enhancement.

The contribution of electromagnetic mechanism towards Raman signal enhancement is greater than any other mechanisms [6, 21]. It accounts for an enhancement factor of at least 10^4 to 10^6 in normal conditions.

1.2.2 Chemical enhancement mechanism

This mechanism is also called as the first layer effect because to observe this effect, molecule and metal surface need to be in contact with each other [7]. This mechanism is mainly attributed to electronic coupling between molecule and metal,

and leads to formation of an adsorbate-surface complex, resulting in an increased Raman cross section of the adsorbed molecule in the complex compared with the cross section of a free molecule in a normal Raman experiment.

Other possible electronic SERS mechanisms involve a resonance Raman effect, which becomes operative due to shifted and broadened electronic levels in the adsorbed molecule compared with the free one or due to a new (charge transfer) electronic transition in the metal-molecule system. Figure 1.3 shows energy level

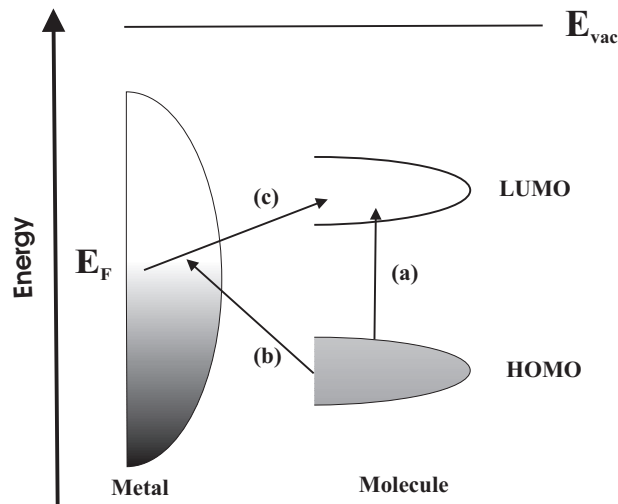


Figure 1.3: Schematic for the chemical enhancement mechanism in SERS

diagram for a molecule-metal system, where the energies of the highest occupied molecular orbital (HOMO) and the lowest unoccupied molecular orbital (LUMO) are approximately symmetric relative to the Fermi level of the metal, together with possible resonant Raman processes involving molecular states (path (a)) and molecular and metallic states (paths (b), (c)). The figure also explains the change of the resonance conditions for paths (b) and (c) when the Fermi level is shifted. This accounts for the potential-dependent SERS enhancement, which is commonly observed in case of metal electrodes [6, 23]. The dynamic charge transfer, which

forms another basis of this mechanism, can be explained as follows:

- The photon is absorbed by the metal which results in a hot electron state.
- The hot electron gets transferred in to the LUMO of the molecule.
- The hot electron is transferred from LUMO back to the metal.
- Return of the electron to its initial state by emitting Stokes photons.

The chemical enhancement mechanism contributes to an enhancement factor of 10 to 100 in magnitude. Interestingly, to observe this effect, the metallic surface need not be rough.

Apart from these two enhancement mechanisms, Surface enhanced Resonant Raman scattering can also be used to further improve the enhancement factors. The conventional resonant Raman scattering offers an advantage of enhancing the Raman scattering intensity of a chromophore by at least 10 to 100 times when compared to non-resonant Raman scattering. This enhancement can be utilized in SERS, where fluorescent molecules are adsorbed on metallic nanoparticles and excited with resonant radiation to obtain Raman scattered spectrum. This technique is generally called as Surface Enhanced Resonant Raman Scattering (SERRS). This method facilitates large enhancements (10^7 to 10^{14}) in the Raman signal, and can be utilized to detect single molecule within a confined volume. In chapter 6 of this thesis we show the optimization and usage of SERRS as an effective probe to detect molecules at extremely low concentrations, which finds relevance in disease diagnostic applications.

1.2.3 Experimental calculation of SERS enhancement factor-G

One of the quantitative methods to evaluate the increase in Raman signal intensity is to calculate the enhancement factors [6, 7, 21, 23]. Since the number of molecules in the probed volume at an instant of time is different for solution and solid phases, the enhancement factors would be different. Following is the procedure to calculate the G for both phases.

Solution phase: First, Raman spectra of a molecule of known concentration (C_R) is recorded in solution phase. Next, the Raman integral intensity of one of the strong bands (I_R) is calculated. This is followed by the recording of SERS spectra of the same molecule at lower concentration (C_S) and calculation of the SERS integral intensity (I_S) of the same band as considered for the Raman spectra. G is calculated using the formula

$$G = \frac{C_R}{C_S} \times \frac{I_S}{I_R} \quad (1.13)$$

It is to be noted that the laser power, signal accumulation time, scattering geometry, optical instrumentation etc., have to be the same for both Raman and SERS measurements. Generally, the sample quantity for these measurements should be at least 1 μL , and the molecule to nanoparticle ratio can be 1 : 9 by volume. The non resonant enhancement factor calculated by this method for thiophenol adsorbed to Ag and Au nanoparticles was of the order of 10^6 and 10^5 , respectively.

Solid phase: Many of the SERS substrates prepared by techniques like nanosphere lithography [25, 26], e-beam lithography [27] etc., are in solid state. In order to evaluate and compare the performance of these substrates, Raman signal enhancement is used as a benchmark. Unlike the solution phase, the concentration of the molecule cannot be directly considered to calculate the SERS enhancement factor.

One has to have a priori knowledge of the number of molecules probed by the laser within a confined volume. This information can be obtained by the method proposed by Zhu et al [28]. The enhancement factor, G can be calculated as follows:

$$G = \frac{I_{SERS}}{I_R} \times \frac{N_R}{N_{SERS}}; \quad (1.14)$$

where I_{SERS} is the measured SERS intensity for the probe molecules on the nanoparticle surface, I_R is the measured intensity of normal Raman scattering from the bulk sample, N_R is the number of the probe molecules under laser illumination in the bulk sample, and N_{SERS} is the number of the molecules probed on the nanoparticle surface. To find I_{SERS} and I_R it is ideal to choose the integral intensity of the same peak in Raman and SERS spectra. The N_{SERS} is given by

$$N_{SERS} = 4\pi r^2 C A N; \quad (1.15)$$

where r, C, A , and N are the average radius of nanoparticles, the surface density of the molecule under study, the area of the focussed laser spot, and the surface coverage of nanoparticles (from electron microscopy or AFM measurements), respectively. The N_R is given by

$$N_R = \frac{A h \rho}{m}; \quad (1.16)$$

where A, h, ρ , and m are the area of the laser spot, the penetration depth, the density of the molecule and the molecular weight, respectively.

1.2.4 Surface selection rules of SERS

When molecules adsorb to metal surfaces, they do so with a specific orientation with respect to the normal of the surface. This orientation of the molecule is mainly a consequence of the electrostatic interaction between the metal and the molecule. Electrostatic image dipoles are one of the main theoretical models to explain this interaction. When considered in the light of vibrational spectroscopy, especially the Raman scattering, adsorption geometry has important consequences on the intensities of the modes of vibration. One of the common features of SERS is that few modes of vibrations are enhanced when compared to others; this is due to the modified vibrational selection rules of a molecule which is in close proximity to a metallic surface. These rules are generally called as surface selection rules, and should not be considered in the view of the usual quantum mechanical selection rules, but rather as rules that explain the reduction in intensities of Raman bands of molecules interacting with metallic surfaces.

Consider a molecule placed at a distance d from a metallic surface. The molecule can be illuminated by two beams (direct and reflected) which superimpose coherently at the molecule. For simplicity, we can consider the molecule to be on the surface, so that d is equal to zero (Note: the final result will be equally applicable for molecules very close to the surface). The components of electric field are given by

$$\begin{aligned}
 E_x &= (r_s + 1)E_{0s}, \\
 E_y &= (r_p - 1) \cos \phi E_{0p}, \\
 E_z &= (r_p + 1) \sin \phi E_{0p};
 \end{aligned}
 \tag{1.17}$$

where r_s and r_p are the Fresnel reflection coefficients at the ambient metal interface for s-polarized (normal to the plane of incidence) and p-polarized (parallel to the plane of incidence) light; E_{0s} and E_{0p} are the magnitudes of the electric field components for s and p polarized configuration. The angle of incidence is represented by ϕ .

Now, if the two incident beams scatter the light by Raman process, then the scattered radiation, for a given angle of incidence, will be a superposition of two coherent waves. The s and p components of electric fields for the scattered light is given by

$$\begin{aligned} E'_s &= (1 + r'_s)p_x, \\ E'_p &= (1 - r'_p)p_y \cos \phi' + (1 + r'_p)p_z \sin \phi'; \end{aligned} \quad (1.18)$$

where the primes indicate the scattered beam, and r'_s and r'_p are their respective Fresnel reflection coefficients but calculated for ϕ' , the angle of scattered light. Four intensities components can be defined for the Raman experiments which refer to different polarizations of incident and scattered beam. Labeling the quantities as SS , PS , SP and PP , where the first and the second letters refer to the direction of electric vectors in the incident and the scattered light, respectively. Here, the scattered plane is defined as the plane containing both the direct and indirect reflection beams from the metal surface [99]. The expressions of the intensity components are given as:

$$SS \propto |\alpha_{xx}(1 + r_s)(1 + r'_s)|^2, \quad (1.19)$$

$$PS \propto |\alpha_{xy}(-1 + r_p)(1 + r'_s) \cos \phi + \alpha_{xz}(1 + r_p)(1 + r'_s) \sin \phi|^2, \quad (1.20)$$

$$SP \propto |\alpha_{yx}(1 + r_s)(1 - r'_p) \cos \phi' + \alpha_{zx}(1 + r_s)(1 + r'_p) \sin \phi|^2 \quad (1.21)$$

and

$$PP \propto |a + b|^2; \quad (1.22)$$

where

$$a = [\alpha_{yy}(1 - r_p) \cos \phi + \alpha_{yz}(1 + r_p) \sin \phi](1 - r'_p) \cos \phi',$$

$$b = [\alpha_{zy}(-1 + r_p) \cos \phi + \alpha_{zz}(1 + r_p) \sin \phi](1 + r'_p) \sin \phi'$$

In the limit of a good reflecting metal, the above equations reduces to

$$SS = 0, \quad (1.23)$$

$$SP = 0, \quad (1.24)$$

$$PS = 0, \quad (1.25)$$

$$PP = |\alpha_{zz}(1 + r_p)(1 + r'_p)|^2 \sin^2 \phi \sin^2 \phi'. \quad (1.26)$$

It is interesting to observe that the SS component, which is the strongest for the normal Raman scattering vanishes to zero, where as the PP component which is not measured in normal Raman scattering is the one which survives. One should bear in mind, however, that even in instances when the metal is not highly reflective, certain intensity components may vanish due to symmetry reasons. The experimental consequences of surface selection rules can be explained as follows. If X , Y and Z are considered as Cartesian co-ordinates representing surface frame of reference where Z is the surface normal, then vibrational modes transforming as Z^2 should have most intense spectral features, ZX and ZY modes will appear with lesser intensity, and X^2 , Y^2 and XY modes should be extremely weak and commonly absent. The selection rules play an important role in understanding the

adsorption behaviour of molecules over metal surfaces, as you would observe in coming chapters.

1.3 Nanoparticles for SERS studies

Two of the main prerequisites to observe considerable enhancement in Raman signal are intense surface plasmon resonance and nanoscale scale roughness of the metallic surface used [6, 7, 21]. Both these parameters have an important consequence on electromagnetic enhancement of SERS. Metallic nanoparticles are ideal candidates possessing the above attributes. Since the surface to volume ratio of a nanoparticle is high, most of their atoms reside on the surface. This feature not only facilitates plasmon oscillation on the surface, but also provides the required surface roughness. The most commonly used nanoparticles for SERS applications are of Ag and Au. Other metals like Cu, Pd and Pt have also been used [22, 23]. It is important to note that all the above mentioned metallic nanoparticles have their surface plasmon resonances in visible region. The present study mainly uses Ag and Au for SERS. Ag and Au are coinage metals with intense surface plasmon resonance in visible wavelength, and their preparation is simple. In SERS literature, there have been two methods of preparation of Ag and Au nanoparticles, which has been extensively used. The first and the most popular one is the citrate reduced method of Lee and Meisel [29], where citrate ions act as the capping agent and provide stability. The other one is the sodium borohydride method of Creighton et al. [30], where sodium borohydride is used to reduce silver nitrate. For the present study we have used the former method because of its stability and performance. Figure 1.4 shows the TEM image of citrate reduce Ag and Au nanoparticles and their surface plasmon resonance spectra in the visible

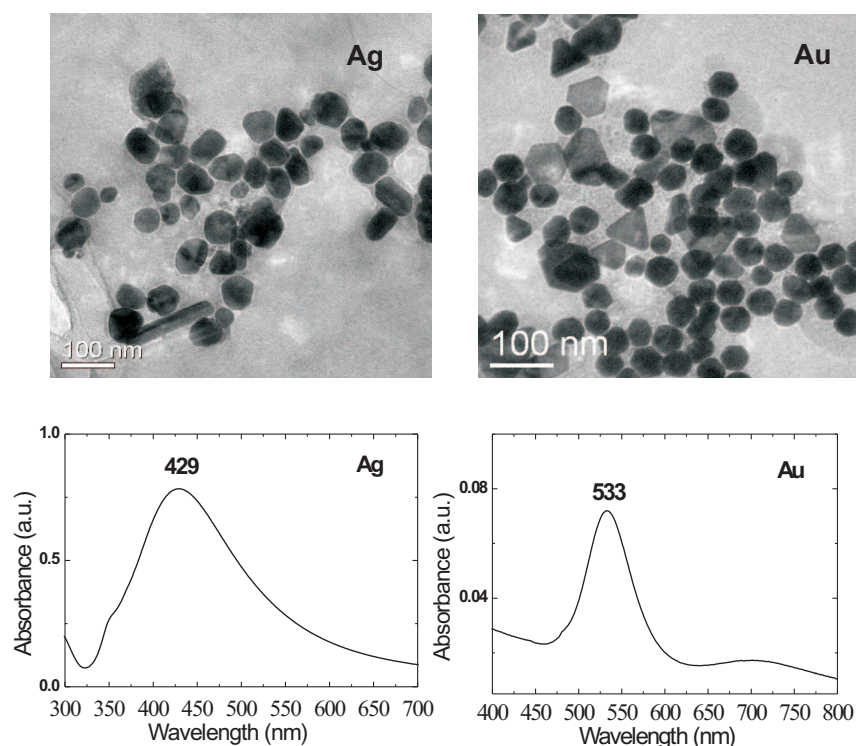


Figure 1.4: TEM images and their corresponding plasmon resonance plots of citrate reduced Ag and Au nanoparticles prepared by Lee-Meisel method.

region. This synthesis method leads to nanoparticles with an average diameter of 50 nm. Both Ag and Au nanoparticles prepared by this method were stable for more than 6 months unlike the nanoparticles prepared by borohydride method. The maximum SERS enhancement factor was observed for Ag nanoparticles. The commonly observed enhancement factor is of the order of 10^6 to 10^7 . Although Ag nanoparticles facilitate high SERS enhancements, they have not been extensively used for biomolecular detection, especially for in vivo experiments due to their bio-incompatibility. In such a case, Au nanoparticles have been the better candidates for studying biomolecules because of the inertness. However, the SERS enhancement factor obtained with Au was of the order of 10^3 to 10^5 , which may be insufficient for ultra trace analysis of molecules. To circumvent this problem

and create a trade off between the properties of Ag and Au nanoparticles, we have devised strategies to prepare core-shell nanoparticles, which constitute the theme of chapter 3.

1.4 Applications of SERS in biodetection

Various research groups across the world have used SERS as an effective tool for biomolecular detection and characterization . Direct detection of biomacromolecules like proteins were ventured as early as in 1980 by Cotton and coworkers [31], where they had used SERS to study adsorption behaviour of cytochrome C and myoglobin on silver electrodes. In recent years, Nabiev and coworkers have developed new techniques which utilized SERS as a probe to study interactions of biomolecules [19, 20]. In chapter 5 of this thesis, we too show that SERS technique can also be harnessed to detect and characterize large biomolecules like p300 in physiological environment at low concentrations. Another interesting strategy is to use SERRS for biomolecular detection. Duncan Graham and coworkers have pioneered methods in using SERRS as an efficient tool for DNA discrimination and analysis [13, 14]. Their strategy is to detect nucleic acids tagged to dye molecules which are in resonance with the Raman excitation frequency. This method has extremely high sensitivity, and has been extrapolated to detection of various kinds of nucleic acids. SERS detection of antigen-antibody interactions with multiplexing abilities were shown by Dou et al. in 1997 [32]. Their work, which used Raman markers (molecules with a large Raman cross-section) for the first time, has important applications in immunoassays and diagnostics. As an offshoot of their work, various research groups have come up with strategies to detect relevant molecules related to diseases like HIV and Cancer. The sixth chapter of

this thesis reveals some of the new strategies devised by us for HIV subtype detection and discrimination by SERRS. Apart from this, SERS has also been used for in vivo studies, wherein gold nanoparticles are introduced into the cell, which further help in enhancing the Raman signatures of different cellular components [33–36]. Van Duyne and coworkers have also used SERS as glucose sensor inside a mice at physiological conditions [37, 38]. Some researchers have also used SERS to detect molecules on the surface of bacteria and other organisms [39–41]. In 1997, Kneipp et al [11] proved one of the most potent abilities of SERS: the single molecule sensitivity. Further, Nie and Emory in 2000 [12] showed that SERS can be performed on single nanoparticle, whose sensitivity was on par with fluorescence techniques. Since then, the unique features of SERS like single molecule sensitivity concomitant to chemical imaging capabilities have added new dimensions to biodetection and sensing [42]. In recent years, these extraordinary abilities of SERS has been harnessed for ultra-trace analysis of molecules of biological interest. Note that, in physiological conditions, the concentrations of biomolecules are scarce, and hence a very sensitive tool like SERS is of primary importance.

1.5 Role of atomic scale roughness in SERS

One of the most rigorously debated concept in SERS literature is the role of atomic scale roughness (ASR) in Raman signal enhancement [134-138]. The physical picture is that if a uniform electric field is applied to a rough conductor, the electric field near the surface is not uniform but is largest at the sharpest feature. This is the familiar principle underlying the operation of lightning rod. In SERS experiments, if the size of roughness feature is less than the wavelength of light, apart from lightning rod effect, one has to treat the system using *adatom model*

where ASR play an important role. In 1983, Otto came up with a comprehensive theoretical treatment [135] with convincing experiments [135,138] on *adatom model* which exemplified the importance of ASR. In this model, ASR sites are those surface atoms for which the primitive translations within a (111), (100) or (110) lattice plane do not lead to full number of possible nearest neighbor within this lattice plane. In SERS, ASR are adsorption sites, where Raman enhancement is stronger than its local environment. The interaction of photon with metal electron increase at these sites compared to atomically smooth surface because local translational symmetry parallel to the surface is broken at sites of ASR[135]. This would lead to a greater charge transfer, and hence significantly influence the chemical enhancement mechanism as discussed before. It is to be noted that roughness at atomic scale have their bearing mainly on chemical enhancement mechanism, and would have no effect on electromagnetic enhancement.

Having laid the foundations to understand SERS, the subsequent chapters will unveil that indeed SERS can be harnessed as an effective tool to probe different aspects of materials and molecules with a fair degree of success.

CHAPTER 2

ADAPTING A FLUORESCENCE MICROSCOPE TO PERFORM SURFACE ENHANCED RAMAN SPECTROSCOPY

This chapter constitutes the following publication:

1. *Adapting a fluorescence microscope to perform surface enhanced Raman spectroscopy*

G.V. Pavan Kumar and Chandrabhas Narayana

Current Science 93, 778-781 (2007).

2.1 Motivation

Ever since the Raman effect was discovered in 1928 [1], it has played a significant role in elucidating structural properties of molecules and materials. Although the Raman scattering acts as an effective tool to probe molecular structure, it has some disadvantages like fluorescence overlap, small cross sections and low sensitivity. Of late, due to the emergence of nanotechnology and improvement in sensitivity of optical instruments, SERS has played an important role in overcoming the above-mentioned disadvantages [24, 42, 43]. Although commercial Raman microscopes have played a key role in the success of SERS, most of them are very expensive, sophisticated, and lack flexibility. There have been a few successful attempts to build Raman microscopes previously [44–46], but most of them require specialized knowledge to construct it. Therefore, it is important to design a SERS setup which is not only inexpensive, but also versatile to perform multiple experiments. In this chapter, we reveal the design and construction of a SERS spectrometer using a simple viewing microscope with an epi-fluorescence attachment, which is routinely used in biology laboratories for fluorescence studies. The salient features of this setup are: it is inexpensive, easy to build, as efficient as a commercial setup and retains the fluorescence imaging characteristics of the microscope.

2.2 Fabrication of SERS microscope

For the present work, we have selected a Nikon Eclipse 50i (Nikon, Japan) microscope with an epi-fluorescent attachment as the main part of the collection optics for the Raman spectrometer. It should be noted that any other fluorescence microscope could be used for the same purpose. Figure 2.1 shows the schematic diagram of the micro-Raman system. The Raman excitation light (532 nm) provided

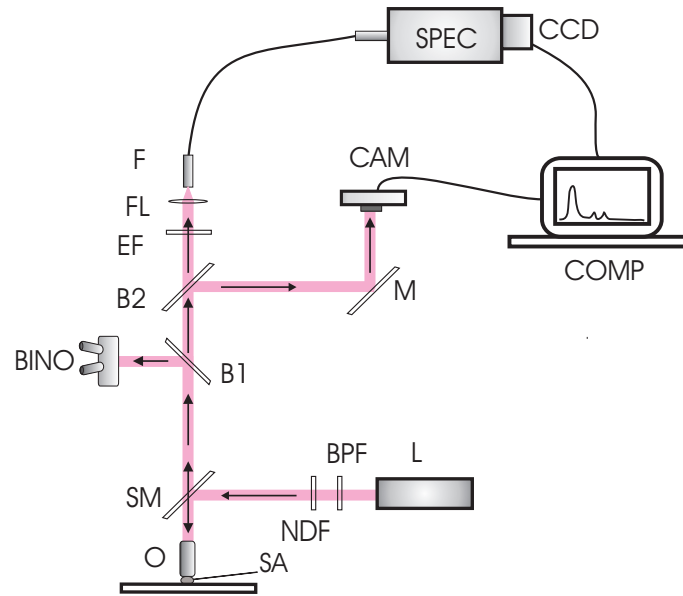


Figure 2.1: Schematics of the micro-Raman system built with a simple viewing microscope with an epi-fluorescent attachment. ST-stage; SA-sample; O - Objective lens; L-laser; BPF-Band pass filter; NDF- neutral density filter; SM -special mirror; B1 and B2-beam splitters; M-mirror; BINO-binocular; EF-edge filter; FL-focusing lens; F-optical fiber; SPEC-spectrometer; CCD - Charged Coupled Device; COMP-computer; CAM-camera.

by a solid-state frequency doubled Nd-YAG laser (Model G-SLM-015, Suwtech Inc., China), which traversed a band pass filter, (LL01-532-12.5, Semrock, UK) was used as the excitation source. The 632.8 nm laser source from a He-Ne Laser (Model No. 30994, Newport, USA) with appropriate band pass filter (LL01-633-12.5, Semrock, UK) was also used in some of the experiments. A special mirror was used in order to reflect the laser beam by 45 degree on to the sample. The scattered light passes through an edge filter (EF) (LP03-532RS-25, Semrock, UK) placed at the output camera port of the trinocular. The scattered light was focused on to the optical fiber using an objective lens (FL) with a NA of 0.4 to 0.5. The other end of the optical fiber was f-number matched at the factory to a 0.55 m spectrograph (Jobin-Yovn 550 Triax, Instruments SA, Inc., NJ, USA) attached with a liquid

nitrogen cooled CCD detector. The f-number matching could also be achieved by using a couple of achromatic doublet lens with appropriate focal lengths and clear apertures.

The spectrograph itself had a computer controlled adjustable slit and a turret, which holds three gratings for a range of measurements. For the present Raman studies, a 600 grooves mm^{-1} grating was used along with the 200 μm spectrograph entrance slit setting, providing approximately 5 cm^{-1} resolution. A digital camera (Nikon coolpix 5400, Nikon, Japan) atop the microscope allowed for registration of the focused laser spot and focusing the image of the laser spot on to the optical fiber (by back illuminating the optical fiber). Typically, for Raman studies on liquid samples, a $60\times$ infinity corrected water immersion objectives (Nikon Fluor, NA 1.00, Nikon, Japan) was used. The laser power was around 8 mW at the sample. The epi-fluorescent attachment, which is used for fluorescent imaging, contains the bayonet mount for placing the white light source. The laser of desired wavelength is launched through this mount. An aluminum disc with 1 mm hole in the center, sitting snugly on the epi-fluorescent lamp attachment, was used to align the laser beam along the axis of the microscope inlet. The adjustable field diaphragm present in the microscope, which restricts the white light illumination on the area of the specimen being viewed, is used as a second aperture to assist the alignment of the laser beam along the optical axis. The diaphragm can be used to focus the laser beam onto the sample under observation. The fluorescence microscopes are provided with dichroic mirror-cube holders. For fluorescence measurements a dichroic mirror is used, which is selected based on the excitation and emission band of the chromophore. In the case of Raman spectroscopy this would effectively block a large region of the Raman spectrum ($< 200 \text{ cm}^{-1}$) close to the Rayleigh scattering. There is an added disadvantage of using the dichroic mirror as it could

also cut off the high frequency Raman spectra ($> 3000 \text{ cm}^{-1}$).

In order to overcome this, we have replaced the dichroic mirrors of the fluorescence microscope with a special kind of mirror. This special mirror was designed by us, and fabricated by Acexon Technologies, Singapore. The mirror has an Ag coating of 2 mm diameter at the center of a $25.2 \times 35.6(\pm 0.2)$ mm fused silica substrate of 1.1 mm thickness. The mirror had a reflection band between 400 to 900 nm, with reflectivity greater than 95 percent. The diameter of the laser beam was 1 mm, which is completely reflected by the mirror of 2 mm diameter. The microscope is equipped with an additional camera port, which is used for imaging the field of view. We have mounted a digital camera on this port. A 200 μm multi-mode, single core optical fiber with a band pass of 400 to 1000 nm was used to collect the scattered light. The length of the optical fiber could be varied between 1.5 to 5 meters. In order to optimize the collection of the scattered light into the fiber, a microscope objective was used at the camera port of the trinocular of the microscope.

For SERS measurements we have used citrate reduced Ag nanoparticles prepared by standard Lee and Meisel method [29]. The analyte of interest was mixed with the Ag nanoparticles in the ratio of 5 : 95 by volume and deposited over a glass slide before bringing the water immersion objective in contact with it for measurements. The final concentration of the analyte was 1 μM . The spectral accumulation time was typically 1 to 30 s for all the measurements.

2.3 Performance of the constructed microscope

In order to demonstrate that the micro-Raman instrument constructed by the above method can serve to detect small traces of biologically important molecules,

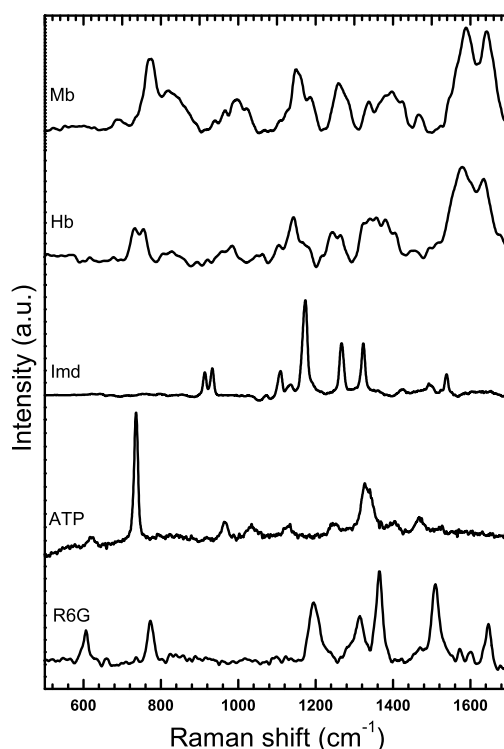


Figure 2.2: SERS spectra of Rhodamine 6G (R6G), adenosine triphosphate (ATP), imidazole (Imd), hemoglobin (Hb) and myoglobin (Mb). The concentration of all the molecules used was $1\mu\text{M}$. Laser power was around 8 mW at the sample. Typical accumulation times were 1 - 30 sec.

we have performed SERS on a variety of molecules like imidazole (a small organic molecule), rhodamine 6G (dye molecule), adenosine triphosphate and macromolecules such as haemoglobin and myoglobin at micro-molar concentrations. Figure 2.2 shows the SERS spectra of these molecules with a typical integration time of 1 to 30s. All the spectra obtained were in good agreement with previous reported results [47–51]. The typical volume of the nanoparticle - analyte system used for such detection was $30\mu\text{l}$. It was found that $7\mu\text{l}$ was the minimum volume of the composite which produced a detectable Raman spectra. Also, one could increase

the detection sensitivity by adding a small amount of NaCl solution, which acts as an aggregating agent of nanoparticles. In order to quantify the SERS enhancement, a neat solution of thiophenol was used for recording the Raman spectra, and a 1 mM solution was used for SERS measurements. Figure 2.3 shows the Raman

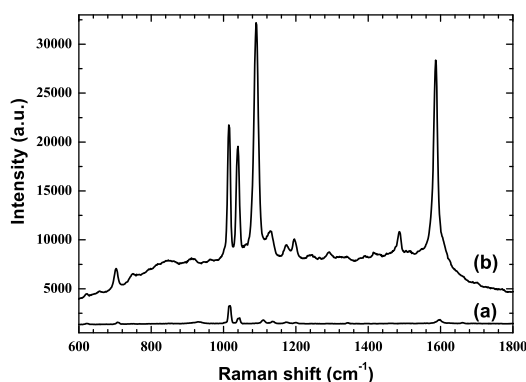


Figure 2.3: Raman (a) and SERS spectra (b) of thiophenol

and SERS spectra of thiophenol (TP). The Raman enhancement factor was calculated for the 1080 cm^{-1} band of TP using the standard method as discussed in the previous chapter, and was found to be of the order 10^6 . Other molecules, such as nucleic acid bases, different dye molecules, proteins and small molecules were detected at low concentrations using this instrument.

2.4 Role and usage of water immersion objective lens in SERS

One of the most important aspects of the Raman instrumentation for SERS studies on biomolecules is the ability to perform experiments in aqueous phase for which one uses a water-immersion objective lens. In order to obtain high spatial

resolution, high throughput, and tight focusing of the incident beam in SERS studies, it is necessary to use a high NA and a high magnification objective lens, like the 1.2 NA and $60\times$ magnification lens used in the present experiment. This has been a common approach for single-molecule SERS experiments as well as confocal Raman imaging [11]. Therefore, it is important to optimize the usage of

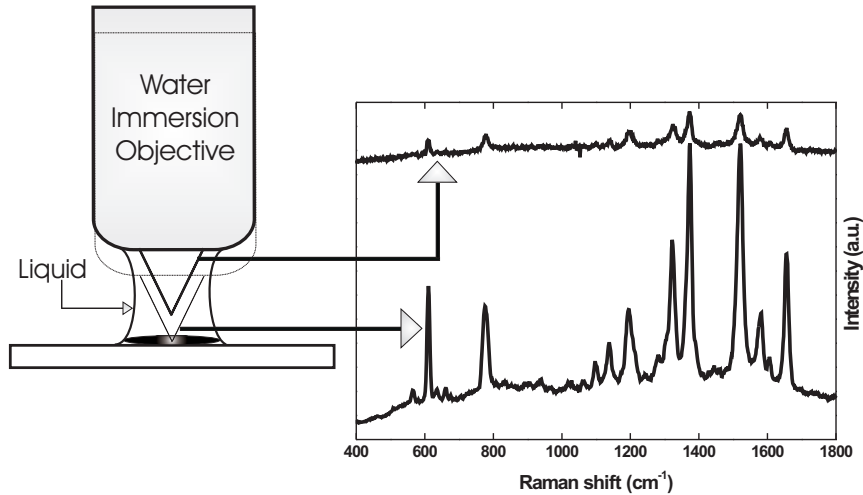


Figure 2.4: Schematic of the water-immersion objective lens focused at two different spots on the glass slide with the analyte-nanoparticle composite solution used for SERS measurements. Faint line on the figure to the left corresponds to the focus of objective lens at the liquid-glass interface. The corresponding SERS spectra of the R6Gnanoparticle composite are indicated by arrows.

these kind of lenses for SERS measurements.

Through a simple experiment, here we demonstrate the capability of water-immersion objective lens to spatially resolve two regions inside the aqueous solution along the focusing direction, which are separated by only a few micrometers. This reveals two important aspects: ability to probe a very small volume, and a limited confocal imaging ability. Figure 2.4 shows the schematic of the objective lens focusing at two different heights inside the liquid, which formed a drop over the glass slide. The SERS spectra recorded on these two spots are also shown alongside.

R6G with Ag nanoparticles was used as a test sample as it exhibits a strong SERS signal. The two spots selected were separated by about a few micrometers; one of them was on the glass-liquid interface and the other was within the liquid just above it. It was interesting to note that the intensity of the strongest mode of R6G (1373 cm^{-1}) increases by a factor of 7.5 in the case of the glass-liquid interface compared to the one within the liquid. The R6G-nanoparticle composite in the liquid is under constant Brownian motion and therefore, the Raman signal collected for a stipulated time is a resultant of a time-averaged signal of the composite residing in the probed volume of the laser beam. At the glass-liquid interface, there would be an aggregation of the R6G-nanoparticle composite due to sedimentation with time. These stationary composite particles would hence provide a large Raman signal due to increase in the Raman scattering probability. This behaviour was common to all the molecules studied using SERS, and hence could be an important tip for SERS experiments. A note about limited confocal ability is worth mentioning. The optical fibre used to collect the scattered light acts as the aperture in this case, and is responsible for the confocality of this system.

2.5 Conclusion

We have shown that a simple viewing microscope used for fluorescence imaging can be modified to perform SERS experiments whose functionality is comparable to a commercial Raman setup. The design and construction of such a setup is not only inexpensive, but also technically flexible. One can modify the design of the microscope depending upon the kind of experiment to be performed. It is also noteworthy that our design is robust which is an added advantage in labs with multiple microscope users.

All the experiments discussed in the coming chapters were performed using this instrument. Using the same setup without any modifications, we have been able to detect several biologically relevant molecules at low concentrations [27, 52–57] which reveals the significance of this instrument. By replacing the manually controlled microscope stage with a motorized one, it is also possible to convert this set-up into a Raman imaging system.

CHAPTER 3

SERS APPLICATIONS OF CORE-SHELL

NANOPARTICLES

This chapter constitutes the following publications:

1. *Hot spots in Ag core-Au shell nanoparticles potent for surface enhanced Raman scattering studies of biomolecules*

G.V. Pavan Kumar, S. Sruthi, B. Vibha, B.A.A. Reddy, T.K. Kundu and Chandrabhas Narayana

Journal of Physical Chemistry C 111, 4388-4392 (2007).

2. *Metal-coated magnetic nanoparticles for SERS applications*

G.V. Pavan Kumar, N. Rangarajan, N. Rohmon, Chandrabhas Narayana
submitted(2007).

3.1 Hot spots in Ag core - Au shell nanoparticles for SERS applications

3.1.1 Motivation

Surface-enhanced Raman scattering (SERS) has emerged as one of the most potent analytical tools to probe different aspects of biology because of its high sensitivity and molecular detection capabilities [6, 11, 12, 14–21, 25]. In SERS, the Raman signal intensity of a molecule gets enhanced by many orders of magnitude when adsorbed to metallic nanostructures exhibiting nanoscale scale roughness. The electromagnetic enhancement and the chemical enhancement are the two fundamental mechanisms for SERS. Most of the solution-phase experiments in SERS are performed using either Ag or Au nanoparticles. With Ag nanoparticles, one can obtain a very large enhancement in Raman intensities, but it is not preferred for *in vivo* studies in biological systems. In contrast, Au nanoparticles are used for *in vivo* studies of biological systems, but they provide moderate enhancement in SERS experiments. It is useful to think of a strategy to use the advantages of both Ag and Au nanoparticles to benefit the studies of biomolecules [58]. Hence, we have carried out thorough investigations on the Ag core-Au shell (core-shell) nanoparticles (NP) as a possible SERS candidate for biological systems. Another important factor in core-shell NP is the possibility of a tunable surface plasmon resonance, which makes it an ideal candidate for wavelength-dependent studies [59].

Recently, there has been a growing interest in understanding of the nature of SERS hot spots in various metallic nanostructures. The hot spots facilitate enhanced optical fields, which in turn contribute to the electromagnetic enhancement

when a molecule is in the vicinity of these spots. There have been various attempts to identify and design SERS hot spots. Some examples of these are (a) the Raman hot spots fabricated using on-wire lithography by Qin et al. [60], (b) hot spots on Ag nanowire bundles by Lee et al. [61], and (c) nanosphere arrays designed by Wang et al [62]. It is important to understand the basic methodology to produce these kinds of hot spots and tailor-make them for SERS applications. Core-shell nanoparticles could be one such candidate, where varying coverage of the shell could introduce hot spots by producing nanopinholes in the shell [58, 63, 64]. In this section, we show that with proper manipulation of the Au shell in the core-shell NP we can produce the SERS hot spots. We also show the difference in SERS properties of core-shell NP with and without the hot spots, and further demonstrate that one can use them to detect different kinds of biomolecules at nano-molar concentrations without the use of conventional Raman markers [58, 64].

3.1.2 Experimental details

Instrumentation-Transmission electron microscopy (TEM) experiments were performed using JEOL 3010 with an operating voltage of 300 keV. Field emission scanning electron microscopy (FE-SEM) was performed using Nova 600 NanoSEM (FEI, The Netherlands). The ratios of Au to Ag were determined using energy dispersive X-ray analysis (EDXA) attached to the FE-SEM. UV-vis measurements were performed using Perkin-Elmer Lambda 900 UV/vis/NIR spectrometer. SERS measurements were performed using a custom-built Raman microscope as described in Chapter 2. In the present experiment, both 632.8 nm and 532 nm wavelength laser were used as the excitation source. The laser powers at the sample were around 10 mW and the typical integration times were 10 s. All the SERS experi-

ments were performed in aqueous conditions using a water immersion objective for focusing the laser and collecting the Raman signals.

Chemicals- AgNO₃, trisodium citrate, NH₂OH.HCl, and HAuCl₄ were bought from Merck, Germany. Rhodamine 6G (R6G), hemoglobin (Hb), myoglobin (Mb), and imidazole (Imd) were bought from Sigma Aldrich, U.S.A.

Synthesis of Ag core Au shell nanoparticles - The Ag colloids were prepared by the Lee and Meisel method [29]. 250 mL of a 5.29×10^{-4} M AgNO₃ aqueous solution was brought to boiling with vigorous stirring, into which 5 mL of 1 % trisodium citrate solution was added. The mixture was boiled for 1 h. The solution was cooled to room temperature with continuous stirring. Core-shell NP was prepared by the seed growth method of Cui et al [58]. The core-shell NP with varying molar fractions of Au was prepared by the following method. A 12.5 mL Ag colloid solution was diluted with 10 mL of ultra-pure water, and x mL of 6.25×10^{-3} M NH₂OH:HCl and x mL of 4.65×10^{-4} M HAuCl₄ were added drop-wise (ca. 2 mL/min) by two separate pipets while vigorously stirring the mixture, where x is the concentration of Au desired in the final product. The stirring was continued for 45 minutes. As a starting point of core-shell nanoparticle preparation, we have used a single batch of citrate-reduced Ag nanoparticles as the seed. The concentration of nanoparticles obtained by this method was around 10^{-4} M. Throughout the synthesis, to obtain different ratios of Au to Ag, the only parameter that was varied was the concentration of HAuCl₄, which would subsequently form the Au shell on Ag core.

3.1.3 Results and Discussion

Figure 3.1a-c shows the FE-SEM images of core-shell NP with Au to Ag ratio of 0.1, 0.4, and 0.8, respectively. There is a broad distribution in particle size, which is due to the size variation in Ag seeds prepared by the Lee and Meisel method. In the case of the core-shell NP, which has Au to Ag ratio of 0.4, we observe pinholes on the surface as shown by arrows in Figure 3.1b. These nanopinholes are formed because of the incomplete filling of Au shells over Ag nanoparticles. These kinds of pinholes are usually formed in large numbers only for a particular ratio of Au to Ag (0.4, in our case), which is in agreement with the previous report by Cui et al [58]. Figure 3.1d shows the TEM image of the core-shell NP (Au to Ag ratio 0.4). The average sizes of these nanoparticles are 50 nm (for Au to Ag ratio equal to 0.4). The TEM image of Figure 3.1d shows a clear contrast between the core and the shell in the nanoparticles. The origin of the contrast in TEM image has been previously studied in detail and is due to the presence of micro-twinning of the [111] plane of the gold over silver [65]. The present method used by us for the preparation of core-shell NP leads to a relatively uniform coating of the shell over the core (see Figure 1d) for Ag to Au ratios greater than 0.4, when compared to earlier methods [63, 64]. This could have an added advantage of functionalizing the surface of the nanoparticles.

Figure 3.2 shows plasmon resonance data for the core-shell NP with varying Au concentration. We observe a shift in the plasmon absorption of the core-shell NP as a function of the Au concentration, which shifts toward the red region of the electromagnetic spectrum. The UV/vis absorption spectra have a contribution from both Ag as well as Au plasmon absorptions, and the contribution shifts from Ag to Au as Au concentration is increased. This behavior arises because of

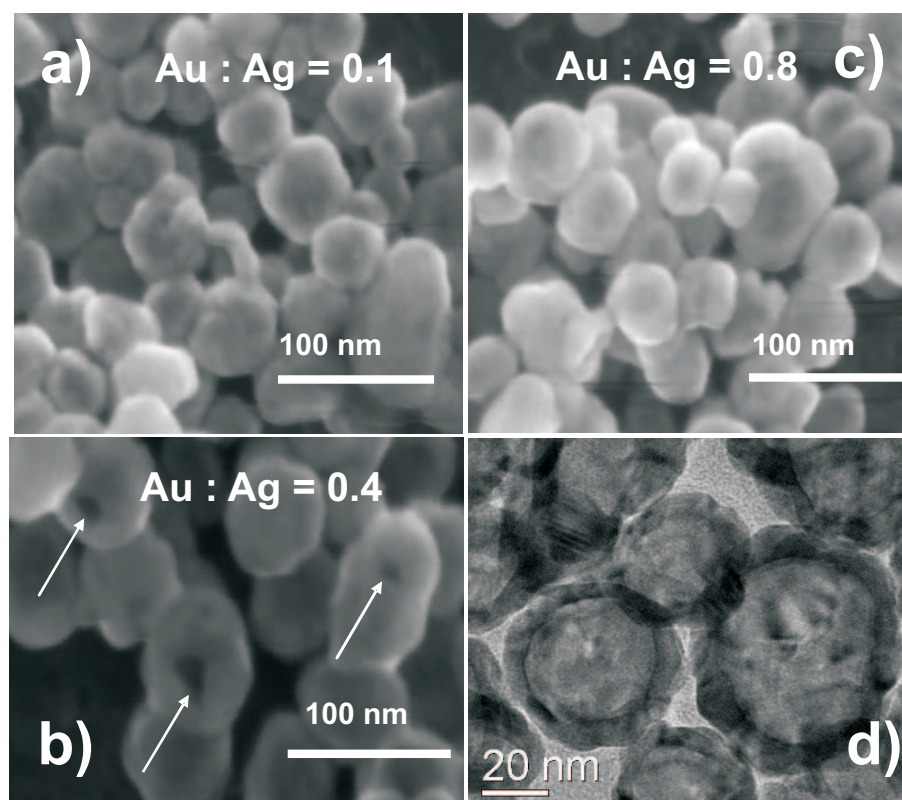


Figure 3.1: FE-SEM images of core-shell NP with Au to Ag ratio (a) 0.1, (b) 0.4 and (c) 0.8. (d) TEM image of core-shell NP shown in b)

the increase in the thickness as well as the coverage of the Au shell around Ag nanoparticles as observed previously [63–65]. It was also observed that the particle size monotonically increased with increase in Au to Ag ratio. However, in some cases, for Au to Ag ratio greater than 0.7, it was observed that the particle size decreased (see Figure 3.1c). This might be because of the direct reduction of excess HAuCl_4 by $\text{NH}_2\text{OH}\cdot\text{HCl}$ to form pure Au nanoparticles along with the core-shell NP, which is the reason for the appearance of the small nanoparticles in the 0.8 case.

We have performed SERS experiments on R6G adsorbed core-shell NP with various ratios of Au to Ag. Figure 3.3 shows a double ordinate plot. Plasmon absorption wavelengths (blue) and the intensity of 1367 cm^{-1} band of R6G (red)

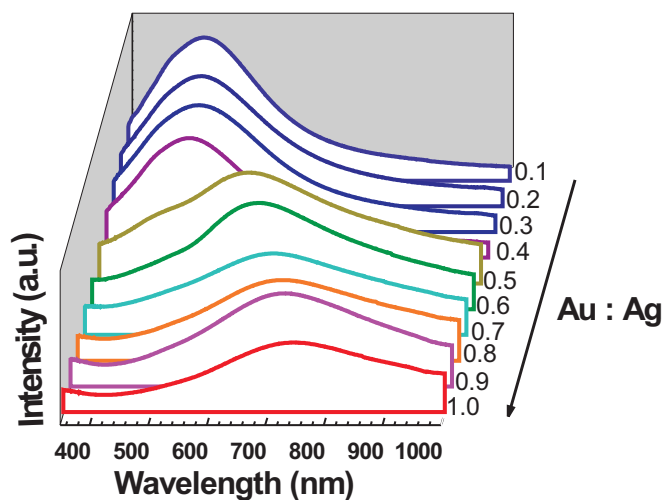


Figure 3.2: UV-VIS absorption spectra of core-shell NP as a function of Au concentration.

are plotted as a function of increasing Au concentration. We observe that there exists a maximum in SERS intensity of the R6G Raman modes for the core-shell NP having a plasmon band peaking at 494 nm and Au to Ag ratio of 0.4. For all the SERS experiments, the concentration of the nanoparticles were held constant (i.e., as synthesized without any further dilutions). We have not used any external aggregating agents like NaCl or KCl. To provide stronger evidence to show that the above-mentioned SERS experiment does not depend on the molecule under supervision or on the Raman excitation frequency used, we have performed the following experiments. At first, the dependence of Raman signal intensity for different molecules (adenine, adenosine triphosphate, thiophenol, and hemoglobin) as a function of Au to Ag ratio was measured and plotted as shown in Figure 3.4a. It can be observed that the curve shows a maximum for Au to Ag ratio equal to 0.4 for a variety of molecules. This data indicates that the enhancement observed is not specific to a particular molecule and suggests that the pinholes in nanoparticles

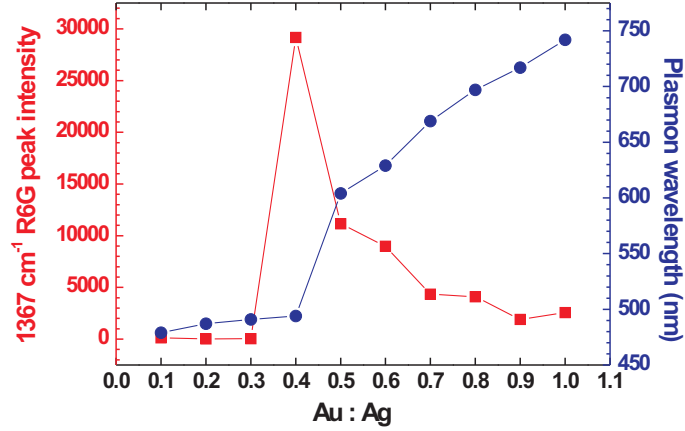


Figure 3.3: Double ordinate plot of intensity of the strongest Raman band (1367 cm^{-1}) of R6G (red) and the strongest plasmon absorption wavelength peak of (a) (blue) as a function of increasing Au concentration.

contribute to enhancement in Raman signal. Next, we performed the same experiment as mentioned above using a different excitation wavelength (532 nm). Figure 3.4b shows again a maximum for Au to Ag ratio equal to 0.4 for all the molecules. This data indicates that the enhancement observed is not wavelength specific and confirms that the contribution is mainly from the pinholes on nanoparticles. In the case of Au to Ag ratio of 0.4, we observe that almost all the nanoparticles appear with pinholes and that the Au shell coverage is nearly complete (see 3.1 1b and d).

From the above data we can infer that the pinholes are indeed acting as hot spots. The enhancement due to hot spots has been explained by Hao et al. [63], who have shown by discrete dipole approximation (DDA) calculations that there would be a remarkable enhancement in the electric field at the vicinity of hot spots. Discrete islands of Au shell on Ag core do not produce hot spots, as is the case of Au to Ag ratio below 0.4. It is known that the density of the hot spots play an important role [139]. If more than 10% of the surface area is covered with the

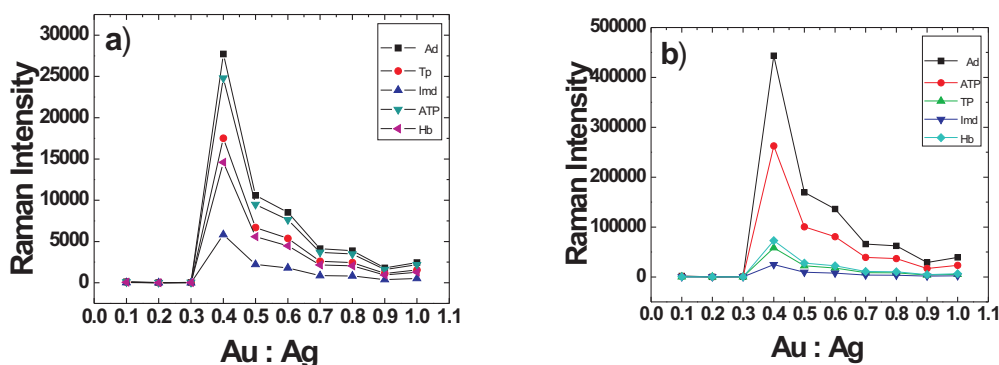


Figure 3.4: a) SERS intensity as a function of Au to Ag ratio for adenine - Ad, thiophenol - TP, imidazole Imd, adenosine triphosphate - ATP and hemoglobin - Hb. Excitation wavelength used is 633 nm and accumulation time is 30 s. b) SERS intensity as a function of Au to Ag ratio for the same molecules as mentioned above. Excitation wavelength used is 532 nm and the typical accumulation time is 10 s.

hot spots, then the contribution of hot spots to SERS measurements could exceed that of the rest of the surface [139]. In our case, the formation of the nano-pores on the surface for Au to Ag ratio of 0.4 leads to the hot spots and in turn results in enhanced Raman signal. The Raman enhancement factor for solution-phase experiments without any aggregating agent (see section 1.2.3) was found to be 10^8 to 10^9 .

Detection of Conventional Biomolecules Using Core-Shell NP with Hot

Spots: Having identified the core-shell NP with hot spots, which lead to maximum enhancement in Raman signal intensity, we have used them to perform SERS on some of the conventional biomolecules like myoglobin, hemoglobin (both are proteins), and adenosine triphosphate (ATP) along with R6G dye and imidazole, which are used extensively in biology laboratories. Figure 3.5 shows the SERS spectra of all the above-mentioned molecules, which is in good agreement with the earlier reports [47–51]. We were able to perform these experiments at 1 nM

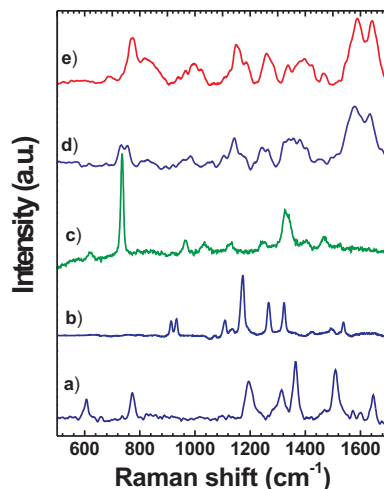


Figure 3.5: SERS spectra of a) Rhodamine 6G, b) imidazole, c) adenosine triphosphate, d) hemoglobin and e) myoglobin recorded with core-shell NP with hot spots. The concentration of the bio-molecules used for these experiments were 1 nM. Excitation wavelength of 632.81 nm and a power of 8 mW at the sample was used with a typical accumulation time of 10 s.

concentration of the biomolecules without the use of external aggregating agent like NaCl or KCl. Normally, the aggregating agents are used to further enhance the Raman signals. In the SERS experiments with biomolecules, especially with the proteins in solution phase, the electromagnetic enhancement play a major role in enhancing the Raman intensity. SERS experiments on protein are rich in the information related to the ring-structured amino acids like phenylalanine, tyrosine, tryptophan, and the polypeptide backbone chains of the protein, since they interact strongly with metallic nanoparticles. The presence of hot spots in core-shell NP would provide substantial enhancement to study the structure of the proteins in solution at low concentrations and in cases where the X-ray crystallographic data is absent.

3.1.4 Conclusion

We have shown that core-shell NPs with pinholes act as hot spots that can greatly enhance Raman intensities of molecules (biological or otherwise) adsorbed onto it. The enhancement is mainly driven by the hot spot phenomenon described by Hao et al [63]. We have compared the core-shell NP with and without hot spots to suggest the importance of the hot spots in the enhancement of Raman signal. Core-shell NP with hot spots have been successfully used to detect different kinds of conventional biomolecules at nano-molar concentrations. Core-shell NPs with hot spots have advantage over Ag nanoparticles since they are better suited for in vivo experiments. By functionalizing the Au shells, one can use them in DNA discrimination and analysis. Thus, we reveal that core-shell NP with hot spots have tremendous potential in molecular detection and sensing.

3.2 SERS applications of metal coated magnetic nanoparticles

3.2.1 Motivation

In recent years, plasmonic nanostructures exhibiting novel optical properties have derived enormous attention [66–69]. The optical properties of plasmonic nanostructures can be varied and tuned by using different metals in various geometrical configurations at the nano-scale [66]. New developments in plasmonic nanostructures have a great impact on various analytical techniques like, surface enhanced Raman scattering (SERS), tip enhanced Raman scattering [70–72], metal-enhanced fluorescence [73]; in which, metallic nano-surfaces play an important role.

Especially in SERS, the nature of the metal, surface morphology and roughness, geometrical configuration, etc., has an important consequence on electromagnetic and chemical enhancement mechanism, which are the two basic principles underlying the phenomenon [6, 21]. Two of the most extensively used metallic nanoparticles for SERS applications are prepared of silver and gold [22]. Another interesting nano-architecture is the core-shell configuration, where either a dielectric or metallic core (usually spherical) can be coated with metallic shells. There are various interesting properties of core-shell nanoparticles, which are not observed in conventional metallic nanoparticles, like tunable surface plasmon resonance [64] and formation of SERS hot spots on a single nanoparticle [56]. Another variation on the same stream of thought is the magnetic core-metallic shell nanoparticles, which exhibits both, magnetic and plasmonic properties. This configuration has opened new avenues in bio-sensing, where two different physical properties of same nanoparticles can be harnessed for detection. Previously, different synthetic routes have been devised to prepare the metal-coated magnetic nanoparticles for specific applications [74, 75]. The present study shows that the magnetic core-metallic shell nanoparticles can be used for SERS applications in aqueous solution using a simpler method. We show that both Ag coated Fe_2O_3 nanoparticles ($\text{Fe}_2\text{O}_3@Ag$) and Au coated Fe_2O_3 nanoparticles ($\text{Fe}_2\text{O}_3@Au$) can be used to perform SERS at very low concentrations of analyte. By performing SERS over a range of temperatures, we also demonstrate the robustness of these metal-coated magnetic nanoparticles. Interestingly, a coating of 15 nm thick Ag or Au on Fe_2O_3 does not alter the magnetic behaviour.

3.2.2 Preparation of metal coated magnetic nanoparticles

All the chemicals were of spectroscopy grade and were bought either from Merck, Germany or Sigma Aldrich, U.S.A. The synthesis of Fe_2O_3 nanoparticles was done following the procedures described in the earlier work [76]. In this method, 10 mL of aqueous solution containing 0.4 M Fe^{2+} , 0.8 M Fe^{3+} and 0.4 M HCl is added drop wise to a moderately heated (50°C) 100 ml of aqueous 1.5 M NaOH solution under vigorous stirring. A black precipitate of Fe_3O_4 is formed immediately. After 15 minutes of stirring, the precipitate is allowed to settle down, followed by washing with water and centrifuged at 6000 rpm. They were again washed with 0.1 M HNO_3 and centrifuged at 6000 rpm. The precipitate was then dissolved in 0.01 M HNO_3 and heated gently up to 90 to 100°C with constant stirring. During heating the black Fe_3O_4 turns to reddish brown Fe_2O_3 . After heating for 30 minutes the solution was cooled to room temperature. The precipitate was subsequently centrifuged at 6000 rpm and then washed twice with water. The final precipitate was dried under vacuum at room temperature for further treatment. Ag or Au were coated on Fe_2O_3 by employing iterative seeding growth method, with hydroxylamine hydrochloride as reducing agent. 100 mg of Fe_2O_3 was dispersed in 50 mL of aqueous solution containing 0.1 M TMAOH and 0.1 M trisodium citrate. A 200 μL of 0.1 M AgNO_3 or 0.1 M HAuCl_4 was added to the solution followed by 200 μL of 0.1 M $\text{NH}_2\text{OH}\cdot\text{HCl}$ incrementally. Each increment was separated by a 15 min interval. After 4 to 5 increments the solution turned to yellowish green for Ag and reddish brown for the Au case. The particles were washed with water, and centrifuged at 6000 rpm and finally dried under vacuum at room temperature for further characterization.

Measurements: Uv-vis absorption measurements were done by using a Perkin-Elmer Lambda 900 UV/VIS/NIR spectro-photometer. Field Emission Scanning

Electron Microscopy (FE-SEM) was done by using a Nova 600 NanoSEM (FEI, The Netherlands). The molar ratios of Fe to Ag and Au were determined by using EDAX equipped to the FE-SEM. SERS measurements were done by using a custom built Raman microscope as described before. The excitation source was 632.8 nm He-Ne laser with a laser power of 8 mW at the sample and the typical integration time was 10 s. All the SERS experiments were done using long working distance, high numerical aperture objective lens, which served the purpose of both focusing the laser and collecting the Raman signals. In temperature dependent measurements of SERS, a Linkam micro-cryostage TMS - 650 (U.K.) was used. Magnetization measurements were performed using a VSM in PPMS (Physical property measurement system) with magnetic fields upto 20 kOe at 298.15 K.

3.2.3 Sample preparation for SERS

For the solution phase experiments, a 20 μL of nanoparticle solution was mixed with 2 μL of analyte (1 μM concentration). After 5 min, 10 μL of the mixture was drop coated over a microscope slide, and SERS measurements were performed using a long working distance microscope objective lens. Nanoparticulate film was formed by room temperature drying of nanoparticles on a glass cover slip. After the solvent evaporation, 2 μL of analyte (1 μM concentration) was drop coated over the film, and SERS measurements were performed on it. The concentration of the measured Ag and Au coated Fe_2O_3 nanoparticles in solution were kept constant at 1.2 and 0.6 mM, respectively.

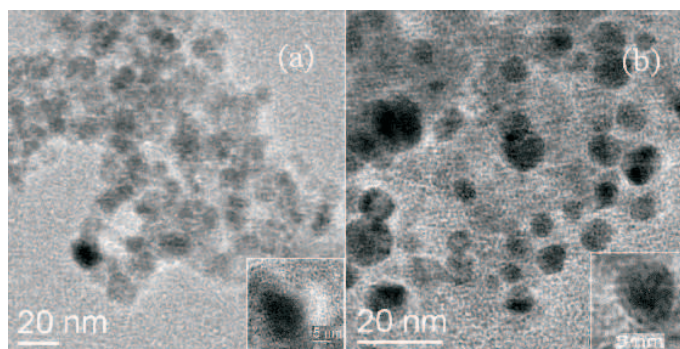


Figure 3.6: TEM images of (a) $\text{Fe}_2\text{O}_3@Ag$ and (b) $\text{Fe}_2\text{O}_3@Au$. The insets show higher magnification images of the same.

3.2.4 Results and discussion

Figure 3.6(a and b) shows the TEM images of $\text{Fe}_2\text{O}_3@Ag$ and $\text{Fe}_2\text{O}_3@Au$, respectively. The average diameter of the nanoparticles were measured to be 20 nm and 15 nm for $\text{Fe}_2\text{O}_3@Ag$ and $\text{Fe}_2\text{O}_3@Au$, respectively. It can be observed that the Ag coated nanoparticles are more aggregated and polydisperse than their Au counterpart. This is a common observation as Ag coated nanoparticles have a greater tendency to aggregate when compared to Au coated nanoparticles. Also, because of its reactivity, it is difficult to control the Ag coating over the seed nanoparticle. The elemental analysis by EDXA measurements revealed the ratios Ag:Fe and Au:Fe to be 53.5% and 23.7%, respectively.

3.2.4.1 Surface plasmon resonance of metal-coated magnetic nanoparticles

The surface plasmon resonance (SPR) absorption due to the collective oscillations of free electrons in metallic nanoparticle appear in the UV-visible region, and its position depends on the shape and size of the particles as well as on the method of preparation, stabilizing agent and solvent dielectric constant [23].

Figure 3.7a shows the UV-visible spectra of Fe_2O_3 nanoparticles, NaBH_4 reduced

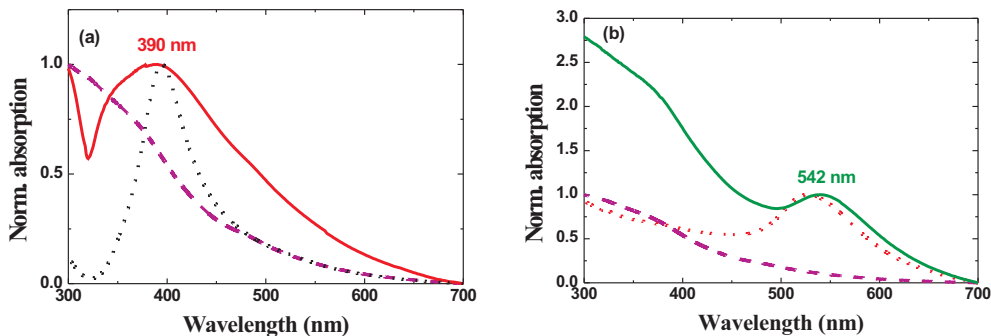


Figure 3.7: UV-vis absorption spectra of (a) $\text{Fe}_2\text{O}_3@Ag$ and (b) $\text{Fe}_2\text{O}_3@Au$. The solid curves indicate the surface plasmon resonance of metal coated magnetic nanoparticles. The dotted curves represent Ag and Au nanoparticle and dashed curves represent Fe_2O_3 nanoparticles.

Ag nanoparticles, and $\text{Fe}_2\text{O}_3@Ag$. Plasmon resonance bands were observed at 390 and 389 nm for Ag nanoparticles, and $\text{Fe}_2\text{O}_3@Ag$, respectively. A very weak band at 350 nm was also observed for the Fe_2O_3 nanoparticles, which may be due to the electronic excitation of oxygen lone pair. Figure 3.7b shows the UV-Visible spectra of Fe_2O_3 nanoparticles, citrate reduced Au nanoparticles, and $\text{Fe}_2\text{O}_3@Au$. Plasmon resonance bands were observed at 527 and 542 nm for Au nanoparticles and $\text{Fe}_2\text{O}_3@Au$, respectively. It is to be noted that both these nanoparticle show strong plasmon bands which is an importation prerequisite for the electromagnetic enhancement in SERS of molecules adsorbed to nanoparticles [6, 21].

3.2.4.2 Magnetic property of metal-coated magnetic nanoparticles

Superparamagnetic (SP) materials show paramagnetic behaviour below the Curie temperatures, and occur in materials composed of very small crystallites, 1 - 10 nm . SP behaviour is observed in single domain, uncoupled ferromagnetic

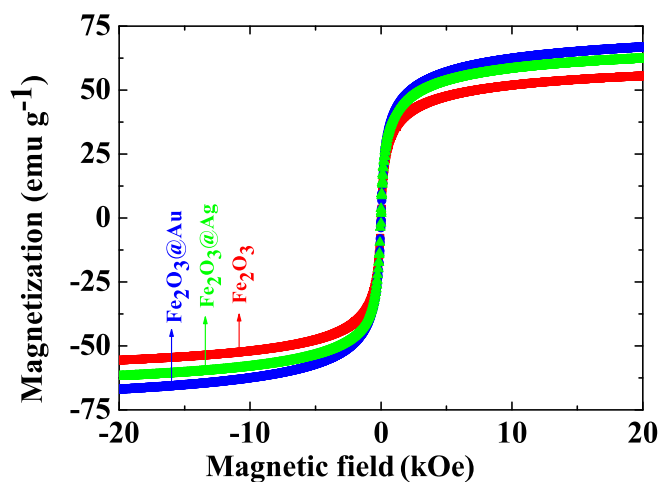


Figure 3.8: Plot of Magnetization versus applied magnetic field at 298.15 K for Fe_2O_3 , $\text{Fe}_2\text{O}_3@Ag$ and $\text{Fe}_2\text{O}_3@Au$.

particles that align their magnetic moments along the applied magnetic field direction, and switch back to a random situation once the field is removed. Generally, hysteresis would be absent in the magnetization cycle, and the resulting behaviour would be similar to paramagnetic one. The notable difference with respect to usual paramagnetism, and the consequent attribute of 'super' is due to the higher magnetization that can be achieved by aligning magnetic particles compared to individual atoms. As in the case of Fe_2O_3 , both $\text{Fe}_2\text{O}_3@Ag$ and $\text{Fe}_2\text{O}_3@Au$ are super-paramagnetic at room temperature. Figure 3.8 shows the magnetization plot for Fe_2O_3 , $\text{Fe}_2\text{O}_3@Ag$ and $\text{Fe}_2\text{O}_3@Au$ measured at 298.15 K. The figures do not reveal any detectable hysteresis at 298.15 K. It was interesting to observe that the magnetization behaviour of all the three nanoparticles under study exhibited similar saturation values when they were normalized for the values of mass. The above data suggests that the magnetic characteristic of Fe_2O_3 in the core shell remain unchanged upon coating with Ag or Au.

3.2.4.3 SERS properties of metal-coated magnetic nanoparticles

Although, metal coated magnetic NPs have been studied either with respect to their plasmonic [75] or magnetic properties [74], they have not been harnessed for SERS applications. Since Ag and Au coated magnetic nanoparticles show strong plasmon bands in the visible wavelengths, one would expect them to exhibit SERS properties like any other core-shell nanoparticles with surface plasmon resonance. Figure 3.9 a and b shows the SERS spectra of molecules (naphthalenethiol (red),

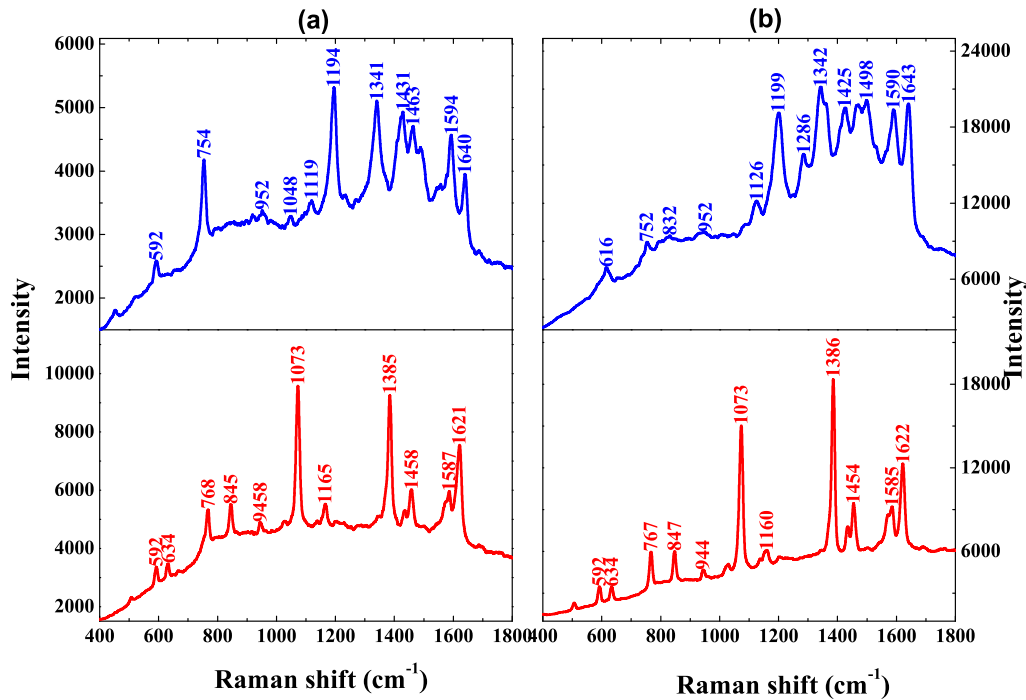


Figure 3.9: : SERS of Rhodamine B (blue) and 2-naphthalenethiol (red) on (a) $\text{Fe}_2\text{O}_3@Au$ and (b) $\text{Fe}_2\text{O}_3@Ag$ recorded at room temperature. The excitation wavelength was, 631.8 nm and the integration time was 10 s.

rhodamine B (blue)) adsorbed on $\text{Fe}_2\text{O}_3@Au$ and $\text{Fe}_2\text{O}_3@Ag$, respectively. The recorded spectra were in good agreement with the existing literature [43, 44]. It is interesting to note that unlike naphthalenethiol, the spectrum of rhodamine B has

slight difference when recorded with the two core-shell nanoparticles. There is a difference in the intensity of 754 cm^{-1} band of rhodamine B adsorbed on $\text{Fe}_2\text{O}_3@Au$ and $\text{Fe}_2\text{O}_3@Ag$ (compare the blue, upper spectra in Figure 3.9). This mode corresponds to one of the substituted ring vibrations [77]. In accordance to the surface selection rule (see section 1.2.4), the difference in band intensity implies that the rhodamine B adsorbs to Au and Ag coated Fe_2O_3 nanoparticles differently. On the other hand, naphthalenethiol adsorbs to the surface of $\text{Fe}_2\text{O}_3@Au$ and $\text{Fe}_2\text{O}_3@Ag$ with a similar geometrical configuration, and hence the spectra were found to be similar in both the cases. Also, the result in the case of rhodamine B highlights the presence of chemical enhancement, wherein the metal-molecule interactions play an important role in Raman signal enhancement. The Raman enhancement factor in solution phase calculated for NT on $\text{Fe}_2\text{O}_3@Ag$ and $\text{Fe}_2\text{O}_3@Au$ were 1.4×10^6 and 1.5×10^5 , respectively. These values are on par with the enhancement factors of conventional Ag and Au nanoparticles. Moreover, we have not used any aggregating agents like NaCl or KCl, which would further increase the enhancement factor due to the chloride ion effect [47]. Since these nanoparticles are magnetic in nature, the rate of aggregation was faster when compared to the conventional non-magnetic metallic nanoparticles used in SERS. This provides an added advantage because the magnetic attraction between the nanoparticles results in an enhanced localization of surface plasmons, which makes the usage of aggregating agents redundant.

3.2.4.4 Temperature dependent SERS using $\text{Fe}_2\text{O}_3@Ag$

Along with pressure, temperature is one of the most important thermodynamic parameter to test the robustness of materials. Raman scattering has been a well-established tool to study temperature and pressure dependant phenomenon

[2, 5]. Of late, due to advancement in optical and cryogenic instrumentation, temperature dependant SERS has evolved as a new technique to test fundamental aspects [78] and applications [27] of nanoparticular films. In order to test the robustness of metal-coated magnetic nanoparticular film, we have performed temperature dependent SERS on $\text{Fe}_2\text{O}_3\text{@Ag}$ drop coated over a microscope cover slip. Figure 3.10 shows the SERS of NT adsorbed to $\text{Fe}_2\text{O}_3\text{@Ag}$ between the tempera-

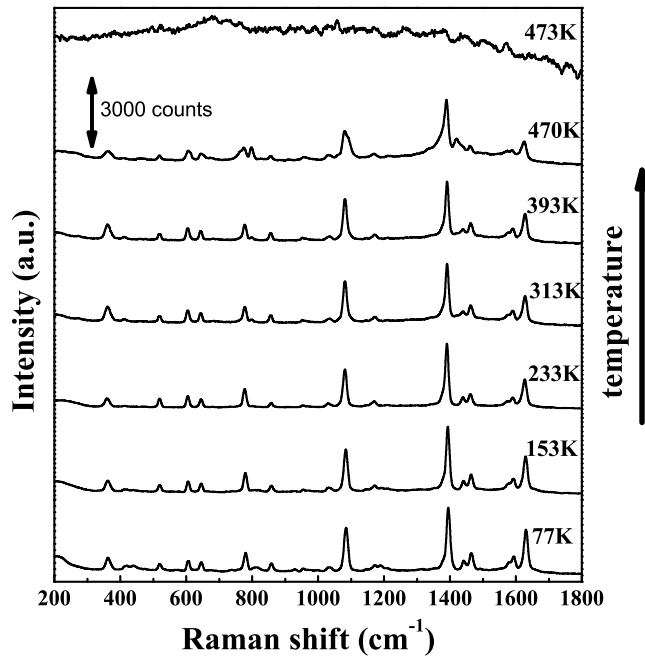


Figure 3.10: Temperature dependence of SERS of 2-naphthalenethiol on $\text{Fe}_2\text{O}_3\text{@Ag}$ in the range of 77 K to 473 K. The spectrum was vertically stacked for clarity.

tures 77 to 473 K. We observed the SERS spectra to be consistently same over a wide range of temperature, which confirms the robustness of $\text{Fe}_2\text{O}_3\text{@Ag}$. It was interestingly to note that the SERS intensity of NT at 473 K drastically changed due to the thermal desorption of NT [79], which was in agreement with the fact that the adsorption of analyte molecules on colloidal particles as one of the prerequisites for

obtaining considerable enhancement in the Raman scattering signal. This shows the sensitivity of the technique to detect the change in adsorption properties of molecules, and proves the efficiency of the metal-coated magnetic nanoparticular film as a SERS substrate.

3.2.5 Conclusion

Ag and Au coated magnetic nanoparticles were synthesized for SERS applications. These magnetic nanoparticles have been used for SERS detection of molecules, and have found to be on par with the conventional Ag and Au nanoparticles. Apart from exhibiting excellent surface plasmon resonance, these nanoparticles are super-paramagnetic at room temperature, which opens new avenues for detection methodologies. Since these nanoparticles can be dispersed in aqueous solution, they are ideal for biological application without any further modification. One could further functionalize these metal coated magnetic nanoparticles with specific proteins that can be covalently linked to Raman markers. This composite can be further introduced into a living cell, and tracked by both SERS and magnetic field.

3.3 Gold-coated Fe₂O₃ nanoparticular films

3.3.1 Motivation

The physical control, assembly and maneuverability of sub-micron matter have various applications in different aspects of science and technology [80]. Nanoparticles are one such paradigm of sub-micron matter with a variety of interesting

physical properties. The size and shape of nanoparticles can be harnessed to fabricate materials for various applications. The surface enhanced Raman scattering (SERS) and magnetism [81, 82] are two of the many attributes of nanoparticles which have been extensively studied in recent years. Of late, there is a surge of interest in hybrid nanoparticles with a rich blend of the above mentioned properties [74, 75]. One such prototype is the gold-coated Fe_2O_3 nanoparticle ($\text{Fe}_2\text{O}_3@\text{Au}$), which is a hybrid material with both, plasmonic and magnetic property. These kinds of nanoparticles have opened new avenues in molecular detection, where two independent properties of a single nanoparticle can be harnessed to improve sensitivity and fidelity of the detection scheme, and thus have gained importance [81, 82]. In recent years, electric and magnetic fields have been extensively used to assemble and manipulate various kinds of nanomaterials. In this section, we show the formation of magnetic field-assisted gold-coated Fe_2O_3 nanoparticular films which are both magnetic and plasmonic in nature. These films exhibit complementary properties with respect to magnetism and SERS, which can be further utilized as special substrates for specific applications. Also, by performing simple experiments with a bar magnet, we show the ability to magnetically control the aggregates of metal-coated magnetic nanoparticles.

3.3.2 Experimental details

$\text{Fe}_2\text{O}_3@\text{Au}$ was prepared as described in previous section. This synthesis method is advantageous because it does not use surfactant as capping agent for the nanoparticles, and are water dispersive. They are ideally suited for SERS applications as the molecules of interest could be adsorbed on to the surface which is weakly capped by citrate molecules. After the synthesis, a 20 μL drop of $\text{Fe}_2\text{O}_3@\text{Au}$

was deposited on a glass coverslip and placed underneath a 10× objective lens of the custom built Raman microscope. A 0.5 T bar magnet was laterally placed with respect to the coverslip to induce the magnetic field on Fe₂O₃@Au.

3.3.3 Results and Discussion

3.3.3.1 Formation of Fe₂O₃@Au thin film in the presence of magnetic field

Here we discuss the formation of a thin film of Fe₂O₃@Au on a glass cover slip in presence of an applied magnetic field. A 20 μL drop of Fe₂O₃@Au was placed on a cleaned glass cover slip, which was about 2 cm away from a 0.5 T bar magnet. The solution was left undisturbed for 2 hours. Upon evaporation of the solvent a film of Fe₂O₃@Au was formed. Figure 3.11a shows optical image of the film formed,

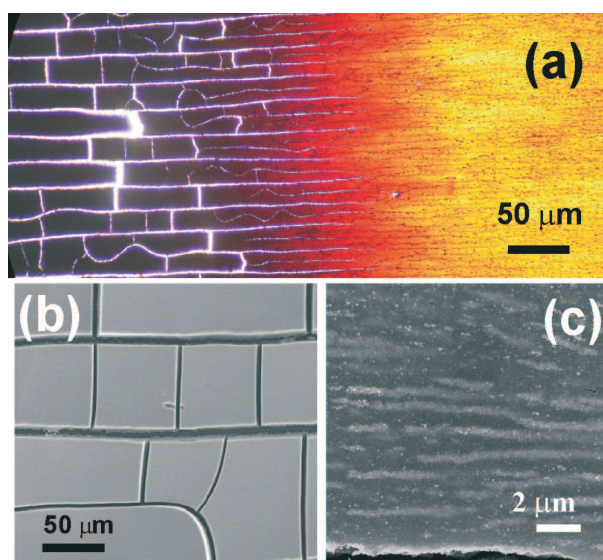


Figure 3.11: Magnetic field assembled Fe₂O₃@Au films. (a) Optical image captured in transmission mode; (b) FE-SEM image of the cracked film; and (c) FE-SEM image of aligned nanoparticles.

illuminated with white light from the bottom. It is evident from the image that the

film had two distinct regions: an opaque region with smooth surface with cracks in between, and a translucent, aligned nanoparticle region. These regions were continuous along the plane of the cover slip with distinct color contrast. The interface region between these regions had a color gradient, which varied from dark brown, to red, and finally merged into the yellow background. We observed same kind of assembly of $\text{Fe}_2\text{O}_3@Au$ on a silicon surface, which was imaged using a FESEM as shown in Figure 3.11(b and c). The cracked region (see Fig 3.11a) resembled cracks formed on dry soil [83], and comprised of smooth, distinct, rectangular and square shaped islands, whose boundaries were well defined. The main reason behind the crack formation would be due to the drying-mediated aggregation of nanoparticles [84] in the presence of a magnetic field, where heterogeneous limits of solvent evaporation dynamics and domain instabilities [85] play a major role. Figure 3.11(c) shows an FESEM image of the filmstrip formed ~ 10 cm away from the magnet. Long strips of $\text{Fe}_2\text{O}_3@Au$ were observed, whose length varied from 100 nm to $10\mu\text{m}$. A high resolution FESEM image revealed that these strips were aligned aggregates of nanoparticles, with a rough surface morphology at the nano-scale. These kinds of strip formation in the presence of magnetic field have been reported earlier for various magnetic nanomaterials [81, 86]. It is to be noted that in the absence of a magnetic field, when a $\text{Fe}_2\text{O}_3@Au$ drop was evaporated neither the formation a cracked film nor of strips were observed.

3.3.3.2 Magnetic and SERS property of $\text{Fe}_2\text{O}_3@Au$ thin films

In order to examine the magnetic behavior of the two regions of the film, magnetization measurement was performed using a Physical Property Measurement System (PPMS). Figure 3.12(a) shows the magnetization curve recorded for a cracked film, and a film containing the aligned strips of nanoparticles. The two

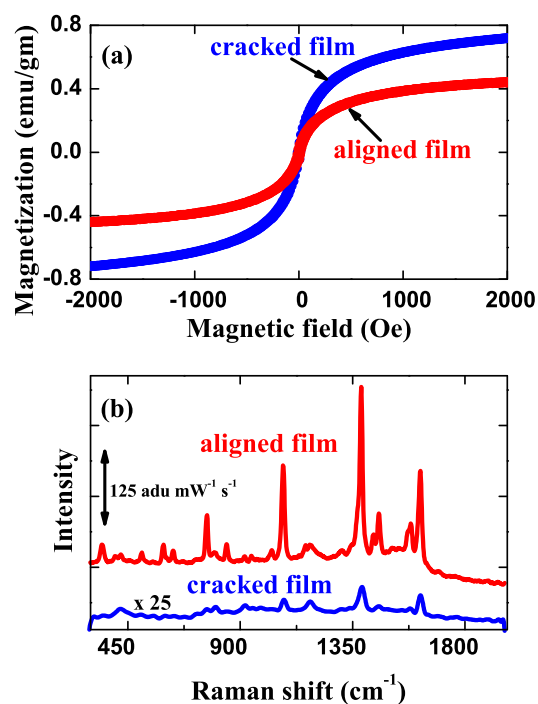


Figure 3.12: (a) Magnetization plots of the cracked Fe₂O₃@Au film and aligned Fe₂O₃@Au film; (b) SERS spectra of naphthalenethiol adsorbed to cracked Fe₂O₃@Au film and aligned Fe₂O₃@Au film, Laser excitation- 632.81 nm; signal accumulation time = 2 s.

regions of the continuous film were separated from each other and measurements were performed individually. Although both these regions of nanoparticles exhibited super-paramagnetic behavior, the normalized magnetic saturation value of the cracked film was higher than the film with aligned magnetic nanoparticles. This is because the cracked film is a compacted structure formed due to the field-induced aggregation of nanoparticles, and hence the magnetic coupling would be stronger. On the other hand, in the strips of nanoparticles, the magnetic coupling is weaker for a given area than the cracked film, which results in a lower saturation of magnetization. Having observed a difference in the roughness of the two regions of a Fe₂O₃@Au film, we tested them for their SERS behavior. An ethanolic solution

of naphthalenethiol ($2\mu\text{L}$ in volume; $1\mu\text{M}$ concentration) was drop-coated over the film. SERS measurements were performed after solvent evaporation. A 632.8 nm laser was used as Raman excitation source. The signal accumulation time was for 2 seconds. Figure 3.12(b) shows the SERS spectra of naphthalenethiol adsorbed on the cracked film, and on the strips of nanoparticles. We observed a large Raman signal enhancement ability of the nanoparticle strips when compared to the cracked film. The difference in the enhancement factors(see Chapter 1) for the 1360 cm^{-1} band of NT adsorbed to the two regions was found to be of the order of 10^4 . This large difference in SERS behaviour is due to the difference in the surface roughness of the two regions of the film upon aggregation. Since the morphology of cracked film was observed to be smooth, one would expect the localized surface plasmon to be absent. In the case of the rough strips of nanoparticles, there would be localized surface plasmons [23] due to the formation of the 'SERS hot spots', which further facilitate huge electrical fields that couple to the polarizability of the molecule. This leads to an enhanced Raman signal. Also, one would expect the plasmonic properties of the two regions in the film to be different from each other, which would account for the difference in the enhancement factor.

3.3.3.3 Magnetic field assisted alignment and rotation of $\text{Fe}_2\text{O}_3\text{@Au}$ aggregates in solution

Manipulating motion of nanoparticle aggregates is of significance in various applications of nano and biotechnology, especially in micro and nano-fluidics. Here, we discuss some simple experiments performed to control the motion of $\text{Fe}_2\text{O}_3\text{@Au}$ aggregates in solution. The basic methods discussed here are pilot-experiments which can be further extrapolated to more complicated configurations in micro and nano-fluidic environments.

Towards one end of the deposited solution of nanoparticle, a bar magnet of the strength 0.5 T was placed at a distance of 1 cm and locked into position. Care was taken to avoid any contact between the magnet and the deposited solution. Upon placing the magnet, the nanoparticles moved towards the magnet and microscopically visible aggregates ($30\mu\text{m}$ wide) were formed at the edge of the drop. The rate of aggregation and the width of the aggregate depend on the strength of the magnetic field. Figure 3.13 (a, b and c) shows the aligned aggregates for three

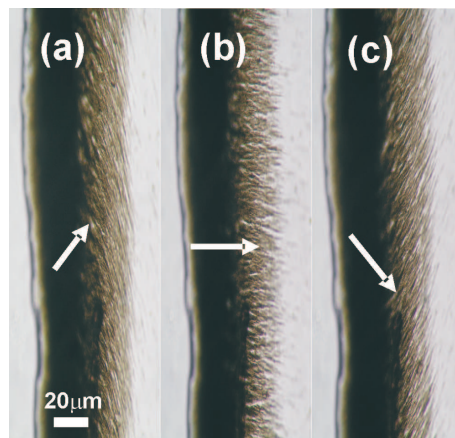


Figure 3.13: Magnetic field induced alignment of $\text{Fe}_2\text{O}_3@Au$ aggregates along three different angles (a) 45 degree, (b) 0 degree and (c) -45 degree. The white arrows indicate the direction of the magnetic field.

different directions: 45, 0 and -45 degrees of magnetic field, respectively. The white arrows in Figure 3.13 represent the direction of the applied magnetic field. As seen from the Figure 3.13, there is a gradation in the aggregation, which starts with a thick aggregate at the edge of the drop and ends with fibrils into the solution. These fibrils are elongated clusters of nanoparticles. The direction of the fibrils show that aggregate tends to align along the magnetic flux lines. One can flip the direction of aligned aggregate by changing the direction of the magnetic field, and the response of the aggregates was instantaneous. The compacted fibrils, which are isolated in the solution, tend to exhibit Brownian motion in the absence of the

field. Upon application of external magnetic field they tend to move towards the aggregate closest to them.

To understand this alignment behavior, we can consider the whole aggregate to be consisting of numerous clusters of magnetic nanoparticles. The self-assembly happens at both the ensemble level (the whole aggregate) and at the individual particle level. At the ensemble level, the magnetization vector of each cluster in the aggregate couples to an effective field, H_{eff} , which is superposition of two components. The first one would be the dominant, applied magnetic field, and the other would be the weak, local field created by the cluster of neighboring nanoparticles. If the elongated cluster in the aggregate can be approximated to an ellipsoidal particle that has a shape induced uniaxial anisotropy, with the easy axis along its length, then the magnetostatic energy E of the cluster is given by [86]

$$E = \frac{1}{2}M^2VN_L + \frac{1}{2}M^2V(N_S - N_L)\sin^2\theta - H_{eff}MV\cos\phi \quad (3.1)$$

where V is the volume of the aggregate, M is the magnitude of the magnetization vector, N_L and N_S are demagnetization factors along long and short axes, respectively, θ is the angle between the long axes and magnetization vector, and ϕ is the angle between the effective field and long axis. The magnetostatic energy would be minimal when the last term in equation 3.1 has the greatest value. This can be achieved when the direction of the effective field and the long axis are in the same direction, that is, when $\phi = 0$. This explains the tendency of the aggregate to align along the field direction.

Having aligned the $\text{Fe}_2\text{O}_3@Au$, we ventured into the possibility of isolating and rotating a micro-cluster of $\text{Fe}_2\text{O}_3@Au$. Rigorous movement of the magnet in the vicinity of an earlier formed aggregate achieved the isolation. Having achieved

it, we slowly rotated the laterally placed magnet with a uniform angular velocity of 0.25 rotations per second. In response to this motion, the isolated clusters in the solution produced a similar rotation. Figure 3.14 shows snapshots of the motion

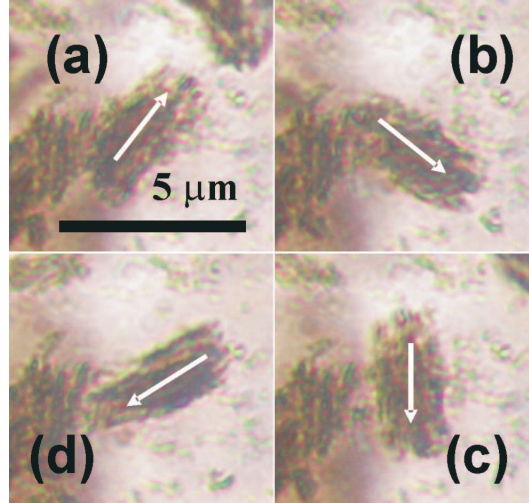


Figure 3.14: Snapshots of a single isolated cluster of Fe₂O₃@Au aggregate rotated by a magnetic field, at different time intervals equal to (a) 0 s, (b) 1 s, (c) 3 s, and (d) 4 s. The rotational frequency of the magnet was 0.25 rotations per second. The white arrow is shown as guide to the eye to follow the rotation.

of the cluster taken at an interval of 1 sec per frame. The white arrow indicates the polarity of the cluster. We could vary the angular velocity of the magnet to change the rotational velocity of the cluster. The physics behind the rotation [87] can be qualitatively explained as follows. The aggregate with a magnetic moment M , placed in a magnetic field H , experiences a torque proportional to $M \times H$. In a varying field, the clusters would experience a force F , which is proportional to the field gradient. This force will try to restore the magnetic moment of the aggregate along the direction of the magnetic field, by inducing a torque, which leads to the rotation. This torque on the nanoparticle aggregate is directly proportional to the rotational speed of the applied magnetic field. It is to be noted here that the magnet was laterally placed along the plane of the liquid (not vertically above the

liquid) and rotated in the same plane, which was advantageous in imaging.

3.3.4 Conclusion

By forming a two-phase film of $\text{Fe}_2\text{O}_3@\text{Au}$, we have shown that the hybrid nature of the zero dimensional nanoparticles can be extrapolated to one dimensional nanoparticle strip, and two-dimensional cracked surfaces. To further harness these films for hybrid plasmonic circuits, they can be studied in light of their surface plasmon resonance properties. We have shown that $\text{Fe}_2\text{O}_3@\text{Au}$, a hybrid plasmonic-magnetic nanomaterial, can be magnetically manipulated with a high degree of control. Since $\text{Fe}_2\text{O}_3@\text{Au}$ contains gold on its surface, their chemistry can be utilized to link different molecules for specific applications. By formation of magnetic field grids, one can self-assemble and pattern these core-shell magnetic particles to harness the SERS properties in microscopic scales.

CHAPTER 4

RAMAN AND SURFACE ENHANCED RAMAN SPECTROSCOPIC STUDIES OF ACTIVATOR MOLECULES OF HISTONE ACETYLTRANSFERASE P300

This chapter constitutes the following publication:

1. *Raman and SERS studies of small molecule activators of histone acetyl transferase p300*

G.V. Pavan Kumar, K. Mantelingu, P.J.Mohan, K. Balasubramanyam,
T.K. Kundu, C. Narayana
submitted(2007).

4.1 Motivation

In the present work, we use Raman and SERS studies to characterize N-(4-chloro-3-trifluoromethyl-phenyl)-2-ethoxy-benzamide(CTB) and N-(4-chloro-3-trifluoro-methyl-phenyl)-2-ethoxy-6 pentadecyl-benzamide(CTPB), which are synthesized from salicylic acid and anacardic acid [54, 88]. Figure 4.1 shows the structure

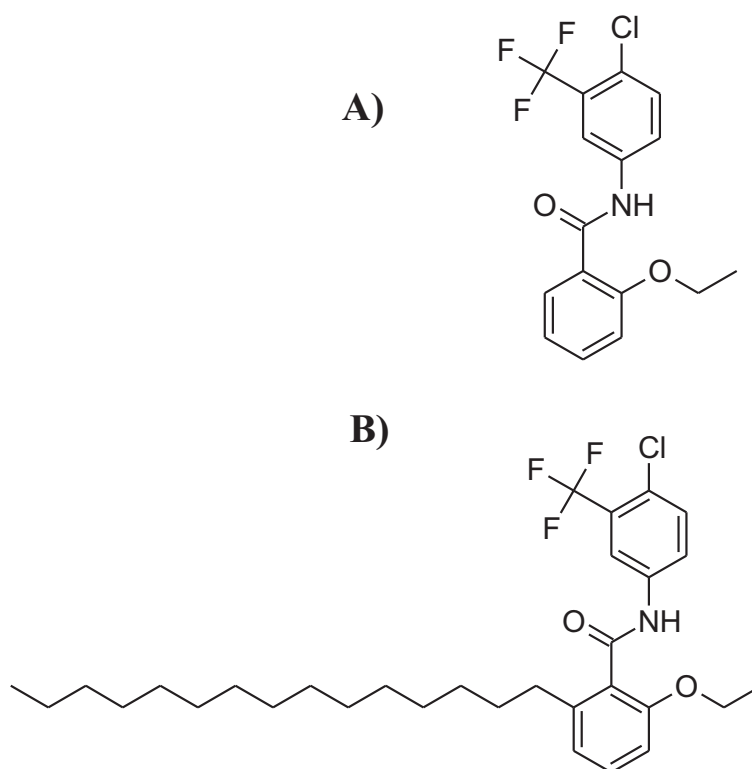


Figure 4.1: Schematic representation of the molecular structure of (A) CTB and (B) CTPB.

of CTB and CTPB. These molecules were synthesized by Kundu and coworkers [54, 88] to specifically activate histone acetyltransferase (HAT) activity of p300. To date, these are the only known small molecule activators of any HAT. It has to be noted that p300 is probably the most widely studied HATs. It has been implicated in a number of diverse biological functions such as, proliferation, cell cycle regulation, apoptosis, differentiation and DNA damage response [89, 90]. It is a

potent transcriptional coactivator and possesses intrinsic HAT activity. Along with this, several important cellular functions including DNA repair, cell cycle, differentiation and establishment of retroviral pathogenesis are regulated by p300 mediated protein (both histone and non-histone) acetylation. Due to its involvement in these important cellular events, dysfunction of p300 may be the underlying causes of several diseases including a few types of cancers, cardiac hypertrophy, asthma, and diabetes [89, 90]. Therefore, the small molecule activators of p300 like CTB and CTPB are therapeutically important lead molecules. Their structural characterization using vibrational spectroscopic technique like Raman scattering would be of great importance.

Since CTB and CTPB are molecules that interact with enzymes, it is important to compare their structure in free and adsorbed state. This motivated us to perform Raman spectroscopy and SERS on CTB and CTPB.

4.2 Experimental details

A detailed procedure of the synthesis of CTB and CTPB can be found elsewhere [54, 88]. Ag nanoparticles were prepared by the standard Lee and Meisel method [29]. The average size of the nanoparticle was measured to be 45 nm. It had a plasmon band centered at 425 nm. Custom built Raman microscope was used for all the measurements, whose details can be found in Chapter 2. All the spectra reported here were recorded using frequency doubled Nd-YAG 532 nm laser. The power at the sample was measured to be 15 mW. The typical signal accumulation times for Raman and SERS measurements were 120s and 30s, respectively. A 100× objective lens with a numerical aperture of 0.95 was used in the 180 degree scattering geometry. Powdered samples of CTB and CTPB were used for Raman

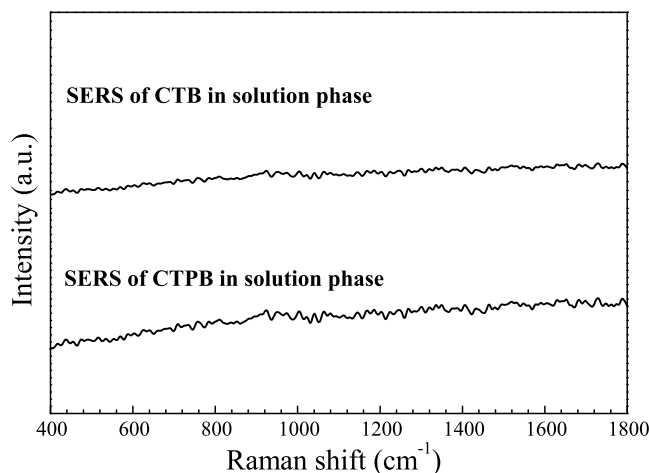


Figure 4.2: SERS spectra of CTB and CTPB in solution phase. The spectrum were devoid of molecular signatures.

measurements. It is to be noted that both these molecules are water insoluble and hence recording the solution-phase SERS spectra with Ag sols was not possible as shown in Figure 4.2. This is a common problem while performing SERS experiments on water insoluble molecules [91, 92]. To overcome this disadvantage, we have recorded the SERS spectra of these molecule adsorbed to concentrated Ag nanoparticles in dry phase. For this, we centrifuged 100 mL of Ag colloids at 10,000 rpm for 4 minutes. The clear supernatant was discarded and the thick blackish gray coloured concentrated nanoparticles were transferred to a separate container. 2 μ L of concentrated Ag nanoparticles was deposited on a clean glass slide and left for drying at room temperature. 1 μ L of 6 μ M solution of molecule (CTB or CTPB) in methanol was drop coated over the deposited nanoparticle surface. As soon as the solvent evaporated, SERS measurements were performed.

Raman spectra calculation details

All the calculations reported herein were performed with Gaussian 03 suite of pro-

grams [93]. Ground state structures are obtained by carrying out a full geometry optimizations with 6-31G (d) (for CTB) and hf/6-31G(d) (for CTPB) basis set using hybrid Becke's 3 Parameter exchange functional and Lee, Yang and Parr correlation functional for non-local corrections and VWN functional III for local corrections (B3LYP). We have calculated Raman spectra at the same level of theory.

4.3 Results and Discussion

CTB and CTPB are two molecules with structural similarities (see Figure 4.1) except for the presence of an additional pentadecyl chain in CTPB. Therefore, the vibrational properties of these molecules are expected to be similar in nature. Both these molecules are insoluble in water and hence, performing SERS in solution phase using Ag hydrosol was not possible by standard methods. In order to overcome this, we have used centrifuged colloids to perform SERS, as explained in the experimental section. Following are the detailed Raman and SERS spectral analysis of these molecules.

4.3.1 Raman and SERS spectra of CTB

The theoretically calculated Raman spectrum and the experimentally observed Raman and SERS spectra of CTB are shown in Figure 4.3 (a-c). The modes of vibrations are assigned in Wilson's notation as shown in Table 4.1. Since the spectrum in Figure 4.3a was calculated in gas phase and spectrum in Figure 4.3b was recorded on the powdered sample, we have not multiplied the calculated spectra with scaling factors to avoid any discrepancies. This leads to a blue shift in calculated spectra when compared to the experimental counterpart. However,

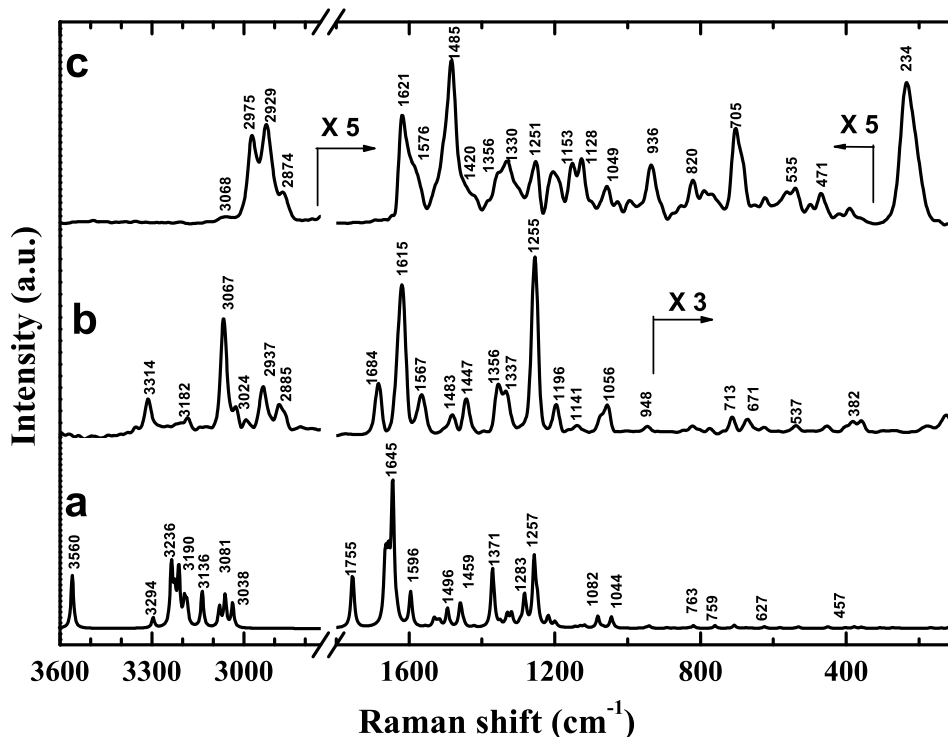


Figure 4.3: (a) Calculated Raman spectrum; experimental (b) Raman and (c) SERS spectra of CTB. Experimental conditions: excitation wavelength 532 nm; accumulation time- 60 s for Raman spectra and 30s for SERS.

we observe a one to one correspondence in the modes of vibrations between experimentally observed and theoretically calculated spectra. Some of the important Raman and SERS modes of vibrations are discussed below.

4.3.1.1 Vibrations of N-H group

We observe the N-H stretching frequency at 3314 cm^{-1} in Raman spectra of CTB (Figure 4.3b). This is a characteristic vibration commonly associated with secondary amide groups [94]. The intensity of this band is weak and broadened

<i>Calc.Raman</i>	<i>Expt.Raman</i>	<i>SERS</i>	<i>Assignment</i>
3560	3314m	-	$\nu(\text{N-H})$
3236	3067s	3068w	$\nu(\text{C-H})\text{ring}$
3190	3024w	2975s	$\nu_{as}(\text{CH}_2)$
3081	2937m	2929s	$\nu_s(\text{CH}_3)$
3038	2885w	2874w	$\nu_s(\text{CH}_2)$
1755	1684m	-	amide I
1645	1615s	1621s	$\nu_{8a}(\text{C=C})\text{ring}$
1596	1567m	1567m	$\nu_{8b}(\text{C=C})\text{ring}$
1496	1483w	1485vs	$\nu_{19a}(\text{C=C})\text{ring}$
1459	1447m	1420m	$\nu_{19b}(\text{C=C})\text{ring}$
1371	1356m	1356m	$\omega(\text{CH}_2)$
1283	1255s	1251m	$\beta(\text{N-H})$
1257	1196w	1153m	$\nu_{as}(\text{CF}_3)$
1170	1141w	1128m	$\nu_s(\text{CF}_3)$
1082	1056m	1049w	$\rho(\text{CH}_3\text{C})$
1044	948w	936m	$\beta(\text{CH}_3)$
763	713w	705s	$\nu(\text{C-Cl})$
627	535w	537w	$\gamma(\text{C=O})$
-	-	234vs	$\nu(\text{Ag-N})$

Table 4.1: Raman shift (cm^{-1}) and assignment of major vibrational modes of CTB

due to the hydrogen bonding in crystalline phase. The SERS spectrum of CTB (Figure 4.3c) does not exhibit the N-H stretch because, the hydrogen is deprotonated and Ag-N bond is formed in the presence of Ag surface. In such a case, one expects the Ag-N vibration to evolve in the SERS spectrum. We observe a very strong band at 234 cm^{-1} in SERS spectra associated with Ag-N stretching. This clearly indicates the bond formation between the Ag and N. This is a characteristic feature of SERS spectra when Ag interacts with molecules containing nitrogen groups [95–97]. This also suggests that there is a short range enhancement component in the SERS spectra, wherein the metal-molecule composite lead to Ag-N bond formation, thereby enhancing the Raman spectra of adsorbed molecule [7]. Apart from this, we observed a strong N-H bending vibration at 1255 cm^{-1} in the Raman spectra of CTB, which is weak in SERS. This supports the above argument.

4.3.1.2 Vibrations of methyl, methylene and C-H group

In the Raman spectra of CTB (see Fig.4.3b), we observed three important stretching vibrations at the high frequency region (2800-3200 cm^{-1}) associated with methyl and methylene group. The 2929 cm^{-1} Raman bands is associated with symmetric stretching of CH_3 group. The weak bands at 3024 cm^{-1} and 2885 cm^{-1} are assigned to antisymmetric and symmetric stretch of CH_2 group respectively. The 3067 cm^{-1} mode is associated with ring C-H stretching vibration.

In SERS spectra of CTB (see Fig.4.3c), the intensity of the ring C-H group reduces drastically. Whereas, we observe an enhancement in symmetric stretch of CH_3 and antisymmetric CH_2 vibration. As per the surface selection rules of SERS [6, 98, 99], this could mean that the enhanced modes have vibrations perpendicular to the Ag surface.

We did not observe any significant differences in Raman and SERS modes of the other vibrations like CH_2 wagging (1356 cm^{-1}), C- CH_3 rocking (1056 cm^{-1}) and CH_3 bending (948 cm^{-1}).

4.3.1.3 Vibrations of benzene ring C=C group

CTB has two substituted benzene rings (see Figure 4.1a). In Raman spectra of CTB, we observe four non-degenerate ring modes at 1615 cm^{-1} , 1567 cm^{-1} , 1483 cm^{-1} and 1447 cm^{-1} . These bands are associated with ν_{8a} , ν_{8b} , ν_{19a} and ν_{19b} of C=C ring stretching modes, respectively. It was interesting to observe that, all of the above mentioned ring vibrations were enhanced in the SERS spectra of CTB, of which, ν_{19a} mode (1483 cm^{-1}) was enhanced to the maximum extent. It is well known in SERS literature that the molecules containing substituted benzene rings interact strongly with metallic surfaces, giving rise to enhanced Raman signatures

[94–97]. Our data is in agreement with this observation.

4.3.1.4 Amide I vibration

Amide I vibrations mainly correspond to C=O stretching with a small contribution from N-H bending. The amide I vibrations was found to be at 1684 cm^{-1} in Raman spectra of CTB. It has been previously observed in secondary amides that the amide I modes are around 1660 to 1685 cm^{-1} , which is in agreement with the molecular structure and Raman spectra of CTB. In SERS spectra of CTB, this mode is very weak, which could imply that either the C=O stretching vibration is aligned parallel to the Ag surface or the deprotonation due to Ag-N bond formation effects this mode [98, 99].

4.3.1.5 Vibrations of carbon-halogen bonds

We observe three weak Raman bands at 1196 cm^{-1} , 1141 cm^{-1} and 713 cm^{-1} , which are assigned to asymmetric and symmetric stretching of CF_3 , and C-Cl stretching, respectively. The asymmetric stretching mode of CF_3 is doubly degenerate; hence, a single mode was observed. All these modes of vibrations are enhanced and slightly red shifted in SERS spectra of CTB. This observed enhancement implies that the above mentioned carbon-halogen moieties may be in close proximity to metallic surface where the electromagnetic enhancement is prevalent. The red shift in these modes could be due to electrostatic interaction of electronegative groups with the Ag^+ ions on the nanoparticle surface.

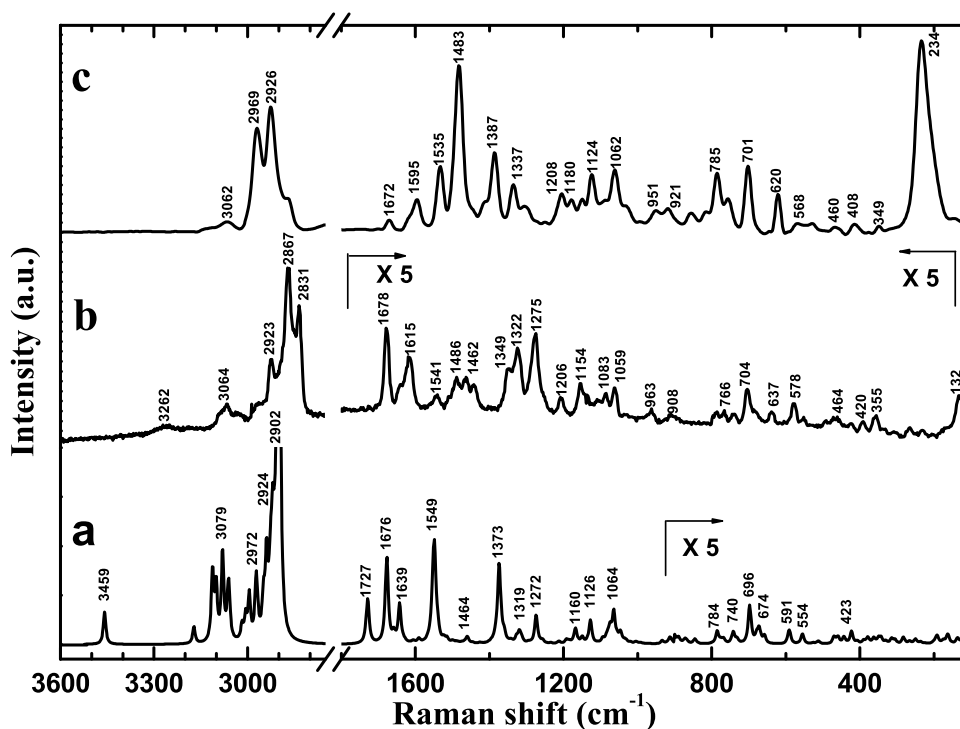


Figure 4.4: (a) Calculated Raman spectrum; experimental (b) Raman and (c) SERS spectra of CTPB. Experimental conditions: excitation wavelength - 532 nm; accumulation time 60 s for Raman spectra and 30s for SERS.

4.3.2 Raman and SERS spectra of CTPB

Figures 4.4 (a, b and c) show the theoretically calculated Raman spectrum, experimentally observed Raman and SERS spectra of CTPB, respectively. Due to the large size of the molecule and computing limitations, we were not able to calculate the theoretical spectra of CTPB using 6-31G-basis set. However, we have attempted to calculate the Raman spectra of CTPB using a different basis, which was feasible within our limitations. Even then, we observe a good correspondence between the calculated and experimental spectrum of CTPB. Since the molecular

structure of CTB and CTPB were similar, except for the presence of an alkyl chain in CTPB (see Figure 4.1), we observe similarities in Raman spectra of CTB and CTPB. This further helped us to assign the Raman and SERS vibrational modes of CTPB, as shown in the Table 4.2. It is evident that most of the vibrations are

Table 4.2: Raman shift (cm^{-1}) and assignment of major vibrational modes of CTPB

Calc.Raman	Expt.Raman	SERS	Assignment
3459	3262w	-	$\nu(\text{N-H})$
3079	3064w	3062w	$\nu(\text{C-H})$ ring
2924	2923m	2926s	$\nu_{as}(\text{CH}_2)$
2902	2867vs	2874w	$\nu_s(\text{CH}_3)$
-	2831s	-	$\nu_s(\text{CH}_2)$
1727	1678s	1672w	amide I
1636	1615s	1595m	$\nu_{8a}(\text{C=C})$ ring
1549	1541w	1535s	$\nu_{8b}(\text{C=C})$ ring
-	1486m	1483vs	$\nu_{19a}(\text{C=C})$ ring
1464	1462m	1387s	$\nu_{19b}(\text{C=C})$ ring
1373	1349m	1337m	$\omega(\text{CH}_2)$
1272	1275s	1208w	$\beta(\text{N-H})$
1160	1154m	1124m	$\nu_{as}(\text{CF}_3)$
1126	1101w	1095w	$\nu_s(\text{CF}_3)$
1064	1083w	1062m	$\rho(\text{CH}_3\text{C})$
-	963w	951w	$\beta(\text{CH}_3)$
784	704m	701s	$\nu(\text{C-Cl})$
674	637w	620m	alkyl chain
591	578m	568w	$\gamma(\text{C=O})$
-	355w	350w	alkyl chain
-	-	234vs	$\nu(\text{Ag-N})$
-	132m	-	alkyl chain

in common with CTB. The presence of an extra alkyl chain in CTPB results in few additional bands in the Raman spectra of CTPB. We observed that the high frequency modes, especially the Raman stretching modes pertaining to methyl and methylene groups to be more intense in comparison to CTB (compare 2800-3200 cm^{-1} region of Figure 4.3b and Figure 4.4b). As in the case of CTB, the 234 cm^{-1}

band was the strongest mode in SERS spectra of CTPB. This again confirms the de-protonation of hydrogen attached to the nitrogen, leading to the formation of Ag-N bond. We also observe that the ring modes of CTPB to be enhanced as in the case of CTB. One of the main differences in the SERS spectra of CTPB when compared to CTB was the presence of amide band at 1672 cm^{-1} , which was very weak in SERS spectra of CTB (compare Figure 4.3c with Figure 4.4c). This observation indicates a subtle difference in the adsorption geometry of CTB and CTPB. Apart from this, we observe small differences in the intensity of ν_{8a} and ν_{8b} SERS modes of the two molecules, which confirms that the adsorption of CTPB on Ag surface is different from that observed in CTB. These differences in adsorption of CTPB to Ag surface may arise due to the steric hindrance offered by the alkyl chain, which constraints the molecule to interact with a specific orientation on the metal surface.

4.4 Conclusion

We have performed Raman and surface enhanced Raman spectroscopy on CTB and CTPB, the two specific activator molecules of the HAT activity of the p300, for the first time. A complete Raman and SERS band assignments have been performed for both the molecules. The Raman mode assignments of both the molecules have been confirmed by performing density functional theory calculations. Although both, CTB and CTPB have structural similarities, we have been able to distinguish them using Raman and SERS spectroscopy. By performing SERS, we have been able to specifically reveal the adsorption sites of the molecules on Ag surface. A very intense 234 cm^{-1} band observed in SERS spectra of both CTB and CTPB indicate the Ag-N bond formed between the molecule and the

metal. Since these molecules are potential anti-neoplastic drugs, our experiments would help in tracking them in-vivo environment.

CHAPTER 5

SERS STUDIES OF HUMAN

TRANSCRIPTIONAL CO-ACTIVATOR P300

AND ITS ACTIVE DOMAIN

This chapter constitutes the following publications:

1. *Surface Enhanced Raman Scattering Studies of Human Transcriptional Coactivator p300* **G.V. Pavan Kumar**, B.A. Ashok Reddy, Md. Arif, T.K. Kundu and Chandrabhas Narayana *Journal of Physical Chemistry B* 110, 16787-16792 (2006).
2. *Activation of p300 histone acetyltransferase by small molecules altering enzyme structure: Probed by Surface enhanced Raman spectroscopy* K. Mantelingu, A. H. Kishore, K. Balasubramanyam, **G.V. Pavan Kumar**, M. Altaf, S. Najundaswamy, R. Selvi, C. Das, Chandrabhas Narayana, K.S. Rangappa and T.K. Kundu *Journal of Physical Chemistry B* 111, 4427-4535 (2007).
3. *Specific inhibition of p300-HAT Alters Global Gene Expression and Repress HIV replication* K. Mantelingu, B.A.A. Reddy, V. Swaminathan, A.H. Kishore, N. B. Siddappa, **G.V. Pavan Kumar**, G. Nagashankar, N. Natesh, S. Roy, P.P. Sadhale, U. Ranga, Chandrabhas Narayana and T. K. Kundu *Chemistry & Biology* 14, 645-657 (2007).

-
4. *Autoacetylation induced specific structural changes in histone acetyltransferase domain of p300: Probed by Surface enhanced Raman spectroscopy*
M.Arif, **G.V. Pavan Kumar**, C. Narayana and T.K. Kundu *Journal of Physical Chemistry B* lett. 111, 11877-11879 (2007).

5.1 Motivation

p300 is a 300 kDa protein present inside the human cell [100, 101]. It belongs to a protein family that participate in many physiological processing like differentiation and apoptosis [90, 100, 102, 103]. They function as transcriptional co-activators and are involved in multiple, signal dependent transcriptional events. p300 is also bestowed with histone acetyltransferase (HAT) activity [104, 105], which transfers an acetyl group to the ϵ -amino group of a lysine residue in the histone (a protein wound to DNA in the nucleus of a cell). p300 is a protein with 2414 amino acids and has several important functional domains present in them as shown in the Figure 5.1. They are: (1) the bromodomain, which is frequently

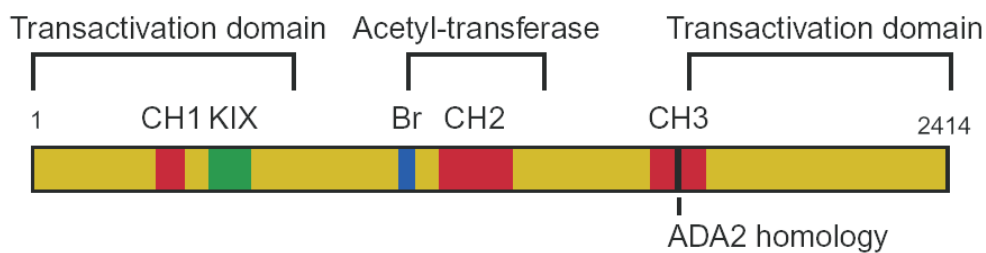


Figure 5.1: p300 domain structure

found in mammalian HATs; (2) three cysteine-histidine (CH)-rich domains (CH1, CH2 and CH3); (3) a KIX domain; and (4) an ADA2-homology domain. The CH1, CH3 and the KIX domains are likely to be important in mediating protein-protein interactions, and a number of cellular and viral proteins bind to these regions. The bromodomain recognizes acetylated residues. Given that an increasing number of cellular factors have been found to be acetylated by p300, bromodomains could function in recognizing different acetylated motifs. Both the N- and the C-terminal regions of p300 can activate transcription, and the HAT domain resides in the central region of the protein. This modular organization may allow p300

to provide a scaffold for assembly of multi-component transcription co-activator complexes. p300 was originally identified using protein-interaction assays with the adenoviral E1A oncoprotein [101]. It has been implicated in a number of diverse biological functions including proliferation, cell cycle regulation, apoptosis, differentiation, and DNA damage response [90, 100, 102, 103]. Primarily p300 functions as transcriptional coactivator for a number of nuclear proteins. These include known oncoproteins (e.g., myb, jun, fos), transforming viral proteins (e.g., E1A, E6, and large T antigen), and tumor suppressor proteins (e.g., p53, E2F, Rb, and BRCA1) [106]. Apart from the histones, p300 also acetylates several nonhistone proteins with functional consequences [107]. Recently, it has been shown that the non-histone substrate of p300 also includes histone chaperone NPM 1, which activates the chromatin mediated transcription in an acetylation-dependent manner [108]. Due to its diverse functional importance any alteration of the function of p300 leads to several diseases, which include cancer, diabetes, Rubinstein-Taybi syndrome, etc [106, 107, 109]. Therefore, p300 is a novel target for therapeutics. Although extensive work has been done to understand the functional mechanisms of such an important transcriptional coactivator, the exact structure-function relations of p300 are yet to be established. Raman spectroscopy has been used in the past to get important structural information from various biological systems, like proteins, nucleotides, peptides, etc. Large concentrations of these biological systems are a must to perform routine Raman experiments. In the case of proteins, polypeptides, and nucleotides which are available in low concentrations, it is commonly observed that routine Raman spectroscopy is difficult to perform due to intense fluorescence and small Raman cross sections. In the case of p300, as discussed later, it is nearly impossible to get any normal Raman spectra due to its scarcity. But, upon addition of some silver nanoparticles to the aqueous solution

of the p300, a large enhancement in Raman intensities has been observed, which is due to the SERS phenomenon.

In this chapter, we discuss the SERS experiments carried out on p300 and present the complete vibration spectral analysis, which shed light into the full length 300 kDa protein structure. In the SERS spectra, it was possible to identify modes related to various functional groups of the protein, which would provide a key to understand protein-drug interactions. In addition to this, we have also studied the effect of chloride ion on the SERS of p300 protein. Chloride ion aggregate silver nanoparticles around the molecule, resulting in large enhancement in Raman signals. To make a comparative study of the effect of silver nanoparticles on aqueous and dry samples of p300, we have performed SERS on p300 dried on a glass substrate in the presence of silver nanoparticles. After this, we describe a new method devised by us which harnesses SERS technique to probe protein-molecule interaction. In particular, we describe the SERS method to probe the p300 interactions with its activator and inhibitor molecules. The final part of this chapter would constitute the SERS studies on p300 HAT domain, which is the isolated, functional part of the p300. We show that SERS can also be used to probe specific structural changes in protein upon modifications like autoacetylation.

5.2 SERS of p300

5.2.1 Experimental details

5.2.1.1 Processing of p300 for SERS studies

The details of the expression and purification of full-length recombinant human p300 and purification of Human (HeLa) Core Histones can be found else-

where [108]. The protein was dialyzed against BC100 (20 mM Tris-HCl (pH 7.9), 10% glycerol, 0.2 mM EDTA (pH 8.0), 100 mM NaCl, 0.5 mM PMSF, 0.01 M 2-mercaptoethanol, and 0.1% NP40) to remove the imidazole for performing the SERS experiments. To deuterate the protein, p300 was incubated in D₂O before performing the SERS experiments. The nanoparticles in D₂O solution were used for the deuterated protein experiments. In order to check the activity of the protein, HAT assay was performed. The indicated amounts of highly purified human core histones were incubated in HAT assay buffer containing 50 mM Tris-HCl, pH 8.0, 10% (v/v) glycerol, 1 mM dithiothreitol, 1 mM phenyl methyl sulfonyl fluoride, 0.1 mM EDTA, pH 8.0, 10 mM sodium butyrate, and 1 L of 3.3 Ci/mmol [3H]acetyl coenzyme A (acetyl-CoA) (Perkin-Elmer-NEN) at 30⁰C for 30 min. The final reaction volume was 30 μ L. The reaction was stopped by incubating the mixture on ice for 10 min before blotting onto P-81 (Whatman) filter papers. The radioactive counts were recorded on a Wallac 1409 liquid scintillation counter. To visualize the radiolabeled acetylated histones, the reaction mixtures were resolved on 15% SDS-polyacrylamide gel and processed for fluorography as described in ref [88].

5.2.1.2 Sample preparation for SERS measurements

SERS of the Aqueous Sample- p300 solution (protein concentration approximately 40 ng/ μ L) was mixed with Ag colloidal solution (prepared by Lee and Meisel method [29]) in the ratio of 1:4 on a glass slide with a cavity in it. After allowing the mixture to settle for 5 min, SERS measurements were performed using the water immersion objective lens of the Raman microscope as described in Chapter 2. To find out the effect of chloride ion in the SERS experiments, NaCl solution was mixed with the above suspension in the ratio of 1:10 (NaCl/suspension). The

final concentration of NaCl was found to be 0.3 mM in the solution mixture.

SERS of p300 on a Glass Substrate- Two methods were used to perform SERS on p300 deposited over the glass substrate. Figure 5.2 shows the schematic

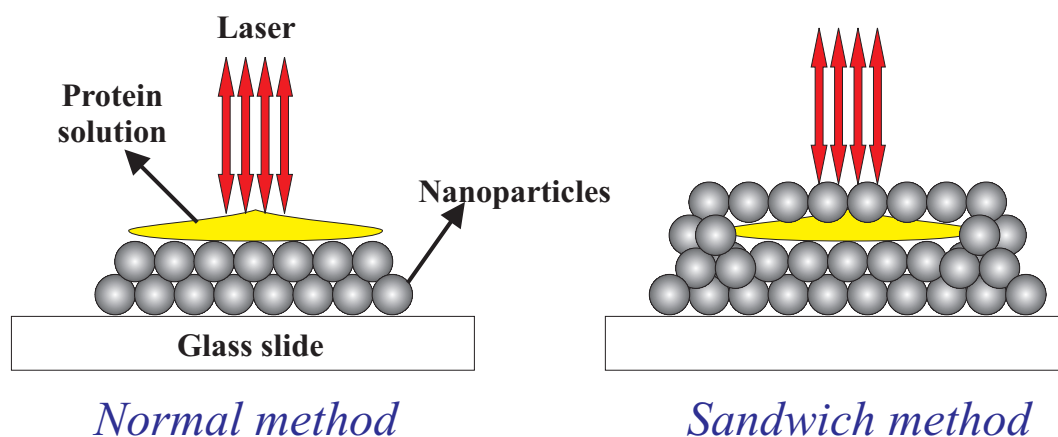


Figure 5.2: Schematic depicting the two configurations of SERS measurements.

of both the methods.

Normal Method: A 100 μL solution of Ag colloid was deposited on a flat glass slide and dried overnight at room temperature. A brown-colored ring was observed over which 20 μL of p300 solution (40 ng/ μL protein in BC100 buffer) was dropped, and the sample was dried at room temperature for 5 h. SERS measurements were performed by focusing the objective onto the uppermost layers of the deposited mixture as shown in the schematic diagram in Figure 5.2. Proper care was taken to avoid any contact with the objective while focusing the laser.

Sandwich Method: A 50 μL solution of Ag colloid was deposited on a flat glass slide and dried overnight at room temperature. On the ring formed by the colloidal solution, 20 μL of p300 solution of the same concentration as mentioned above was deposited followed by 50 μL of Ag colloidal solution as shown in Figure 5.2. The sample was left to dry at room temperature for 5 h. The SERS measurements were performed as discussed in the normal method.

5.2.2 Results and Discussion

Although p300 is one of the most important multifunctional proteins in humans, very little is known about the structural dynamics of it. However, the structural and functional domain organization of p300 (Figure 5.1) indicates that the protein presumably undergoes vibrational reorganization at the amino acid level to achieve diverse functional ability. The functional domains of p300 include nuclear hormone receptor (Nr) cysteine/histidine-rich zinc finger domains CH1 (347-413), CH2 (1195-1451), and CH3 (1669-1807), the KIX domain, the bromo domain (Br), the histone acetyltransferase (HAT) domain, and the minimal HAT domain (1284-1669). The N and C-terminal domains can act as transactivation domains. For the present study, the protein was dialyzed against BC100 buffer to remove imidazole. The HAT activity of p300 was assayed by filter binding of radiolabeled acetylated histones (Figure 5.3). SERS of p300 was carried out with the protein adsorbed on silver nanoparticles. Therefore, it was essential to find out the effect of the silver surface on the functional activity of p300. The HAT activity of p300 incubated with silver nanoparticles was assayed by filter binding. As depicted in Figure 5.3, the HAT activity of p300 adsorbed on the silver nanoparticle surface remained almost the same as compared to that of the mock incubated enzyme (lane 2 vs 3). These data suggest that the SERS of p300 shown in this report represent the structural dynamics of the functional enzyme.

5.2.2.1 SERS Spectra of p300 in the solution phase

The components of a solution phase SERS experiments on proteins generally contain a buffer solution(BC100,in present case) and nanoparticles along with the protein. Therefore, it is important to confirm that there are no interfering Raman

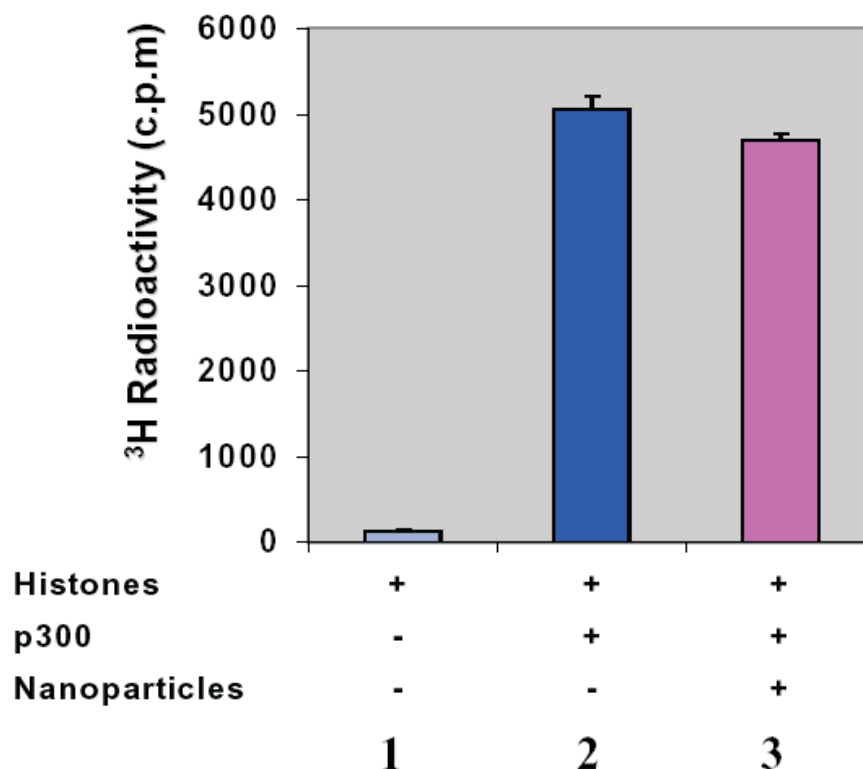


Figure 5.3: Filter binding assay: HAT assay was performed by using highly purified HeLa core histones (800 ng) in the absence (lane 1) and presence (lane 2) of enzyme p300 (5 ng) and the enzyme (p300) incubated with Ag nanoparticles (lane 3). The results represent the average values with error bars from three independent experiments.

bands of the buffer and nanoparticles, which essentially act as noise in the spectra of the protein. In order to confirm the authenticity of SERS spectra of p300 in such a situation, we performed a series of control experiments whose results are displayed in Figure 5.4. In order to reassert the peaks of p300, the SERS spectra of the buffer, Raman spectra of neat protein and nanoparticles were recorded. It is evident from the Figure 5.4 that the SERS spectra of p300 differs from the other spectra displayed. One of the main motivation behind using SERS to detect this protein is that Raman spectra of p300 is extremely weak, as shown in Figure 5.4. This is not only because of the feeble concentration of the protein, but also due to

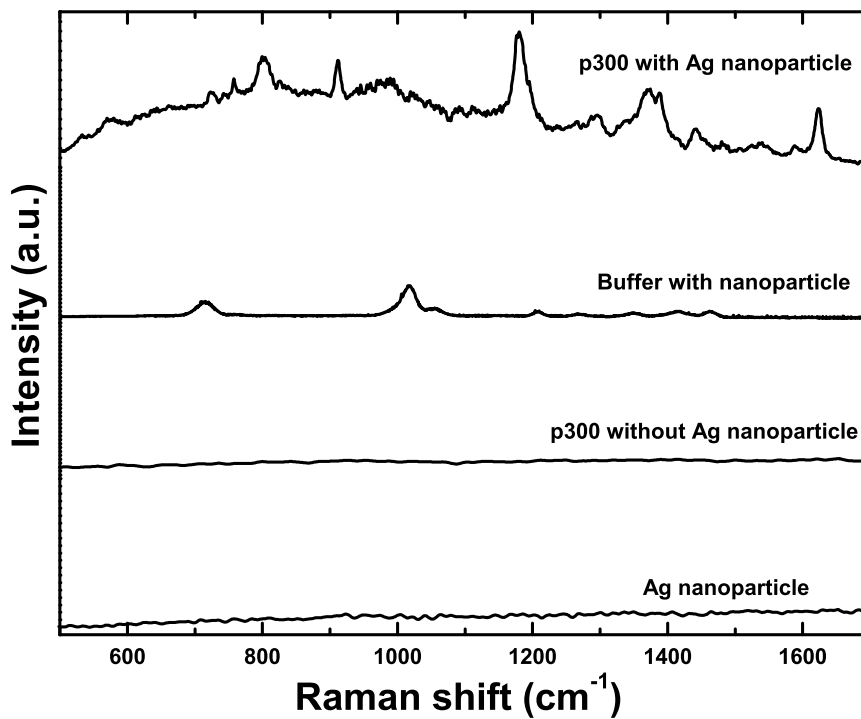


Figure 5.4: Control experiments: Raman spectra of nanoparticles and p300, and SERS spectra of buffer compared with SERS spectra of p300. The experimental conditions were same for all measurements.

the low Raman cross section exhibited by the macromolecule.

Next, the SERS spectra of p300 is discussed. As described earlier, p300 is a 300 kDa protein with 2414 amino acids. Therefore, the vibrational modes arising due to this protein would be a superposed contribution from various amino acids, which complicates the analysis. However, in special cases like SERS, where a macromolecules like p300 interact specifically with metallic nanoparticle, one should expect only particular modes of vibrations to arise. Figure 5.5 shows the SERS spectra of p300 protein recorded in H₂O and D₂O. The concentration of p300 was around 40 ng per μL . At such a concentration, it is nearly impossible

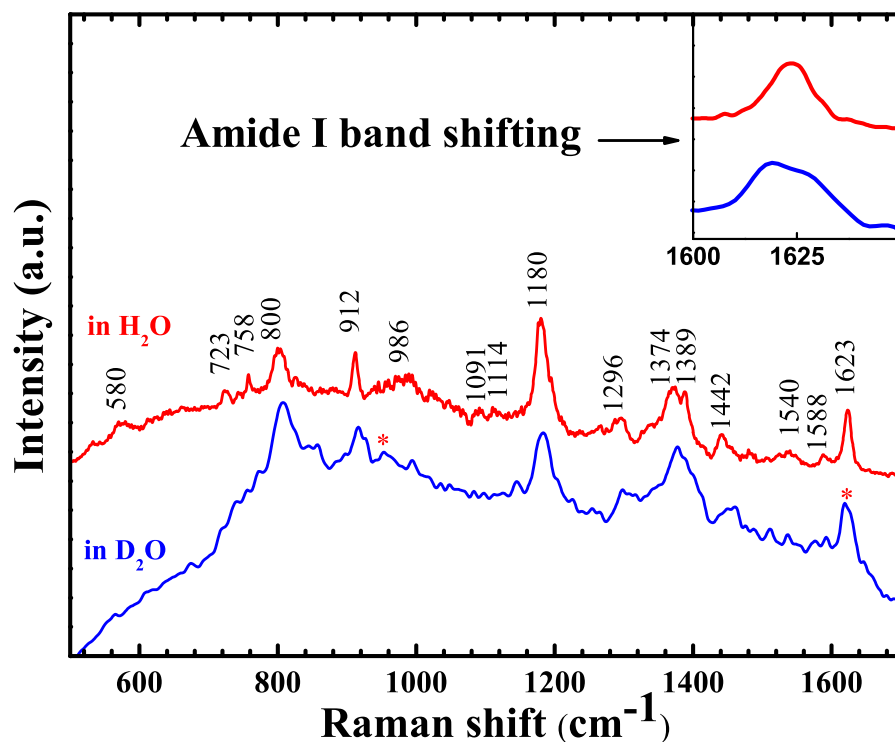


Figure 5.5: SERS spectra of p300 in H_2O and D_2O at 40 ng per μL concentration. The * mark in the lower spectrum indicates shifted amide modes. The inset explicitly shows the shifting of amide I band upon deuteration.

to obtain normal Raman spectra, whereas, the SERS spectra is evidently strong with high signal to noise ratio. Table 5.1 shows the observed frequencies of the most important SERS bands and their proposed band assignments for the SERS spectrum of p300 recorded in H_2O . The band assignments have been carried out in accordance with the existing literature pertaining to SERS spectra of amino acids and proteins [15–17]. As expected, aromatic rings, amides, and carboxylic group vibrations dominate the SERS spectrum of p300. We describe some of the characteristic SERS vibrations observed in the spectrum.

Table 5.1: Assignment of Raman bands in the SERS spectra of p300

Raman shift(cm^{-1})	Band assignment
1623	amide I
1588	$\nu_{as}(\text{COO}^-)$, His, Trp, and/or Phe(ν_{8a})
1540	Trp and/or amide-II
1442	His and/or Trp
1389	$\nu_s(\text{COO}^-)$
1374	$\beta(\text{CH})$
1296	amide-III (α helix) and/or $\delta(\text{CC}_\alpha\text{H})$
1180	Tyr and/or Phe(ν_{9a})
1114	$\nu_{as}(\text{C}_\alpha\text{CN})$
1091	$\nu(\text{C}_\alpha\text{N})$
912	$\nu(\text{C-COO}^-)$
800	Tyr and/or $\nu_{as}(\text{C-S-C})$
758	Trp or His
723	$\delta(\text{COO}^-)$
580	Trp

Polypeptide Backbone Vibrations- The SERS spectra of p300 in H_2O shows three Raman bands associated with the polypeptide backbone at around 1623, 1540, and 1296 cm^{-1} . The 1623 cm^{-1} is associated with vibrations of the amide I band. This band generally appear in the protein spectra when the α helix of the protein is in close vicinity of the silver surface. It has been seen that most of the common proteins adsorb to the silver surface through the α helix [16, 17]. The next band, viz., 1540 cm^{-1} , is due to the amide II vibration. In normal Raman spectra these modes of vibrations have low relative intensity. In the SERS experiments there is a modification in the selection rules giving rise to this band [98, 99]. This is due to the changes in the bond angles, which induce changes in the polarizability of the vibrations in the presence of the nanoparticles. It is to be noted that there are 12 tryptophan (Trp) residues in p300, which exhibits a SERS band in this region. Therefore, the possibility of this mode overlapping with Trp cannot be ruled out. The amide III vibration was observed at 1296 cm^{-1} . The

amide III band often overlaps with the $\delta(\text{CC}_\alpha\text{H})$ vibrations, and hence the Raman band at 1296 cm^{-1} could have contributions from both of these vibrations.

To confirm all the observed amide vibrations, we have performed SERS on deuterated p300. In the deuterated p300, the hydrogens in the amide are replaced by heavy deuteriums. Hence, the vibrational frequencies of the amide bands should decrease in deuterated p300. The blue curve of Figure 5.5 shows the SERS spectra of deuterated p300. Significantly, both curves of Figure 5.5 closely resemble each other. Since the deuteration happens mainly at the amide group, this observation is on the expected lines. Upon deuteration, we observe a decrease in the amide I band frequency by 7 cm^{-1} which is explicitly shown in the inset of Figure 5.5. There is a clear shift from 1623 to 1616 cm^{-1} . In blue curve of Figure 5.5, we do observe distinct changes in the amide II and amide III regions around 1540 and 1296 cm^{-1} , respectively. This supports our earlier statement that these peaks are a superposition of the Raman bands of the amide groups and that of other functional groups in the same region. We also observe a new mode around 950 cm^{-1} in the deuterated p300 spectra (marked * in Fig 5.5). It is known that upon deuteration the amide III band shifts from 1296 to 950 cm^{-1} (340 cm^{-1}) [110]. These observations confirm the amide band assignments.

It is interesting to note that we do not observe any amide bands pertaining to β sheet or random coil of p300 protein. The crystal structures of p300 and CBP (functional twin partner of p300) are not known. The solution structure of the active domains of p300 and CBP reveal that indeed in these domains there is no β sheet or random coil. However, on the basis of the primary structure, it could be predicted that p300 may contain very short stretches of β as well as random coils. Since none of the structural information available so far is from the full-length protein, our spectral analysis may reflect more realistic structural information about

p300. However the complete structure-function correlation can only be achieved by the high resolution full-length crystallographic study of p300.

Vibrations Associated with the Aromatic Side Chain- The SERS spectrum of p300 is dominated by aromatic side chain vibration of tyrosine (Tyr), tryptophan (Trp), and phenylalanine (Phe). Table 5.1 gives the detailed assignments of these modes. It is necessary to point out here that p300 is quite rich in these aromatic amino acids. There are 12 Trp, 46 Tyr, and 44 Phe present in the primary structure of p300. We do not observe the phenyl ring-breathing mode of Phe as well as the indole ring mode of Trp. This could be due to the fact that these groups may not be in close proximity to the silver surface. This kind of behavior has been observed previously in the SERS spectra of lysozymes adsorbed to silver, where the short-range component of SERS was predominant [111]. It could also be due to the orientation of the molecules with respect to the silver surface.

Aliphatic Side Chain Vibrations The carboxylate group of the aspartic acid (Asp), glutamine (Glu), and/or the C terminus group in protein interacts with the silver surface to give strong enhancements of these Raman bands [112]. The bands at 1588 and 1389 cm^{-1} are assigned to the asymmetric and symmetric stretching modes of the C-O-O group, respectively. In the SERS spectra a strong Raman feature at 912 cm^{-1} is seen, which is due to the C-COO stretching. One also observes the Raman band at 723 cm^{-1} due to $\delta(\text{COO}^-)$ vibrations. There are two weak bands around 1091 and 1114 cm^{-1} , which are due to the stretching of C_αN and the asymmetric stretching of CC_αN groups, respectively. This observation suggests that the p300 adsorbs to the silver nanoparticles through the nitrogen groups. This could also be one of the reasons for the presence of strong amide bands in the SERS of p300.

5.2.2.2 Chloride ion effect on SERS Spectra of p300

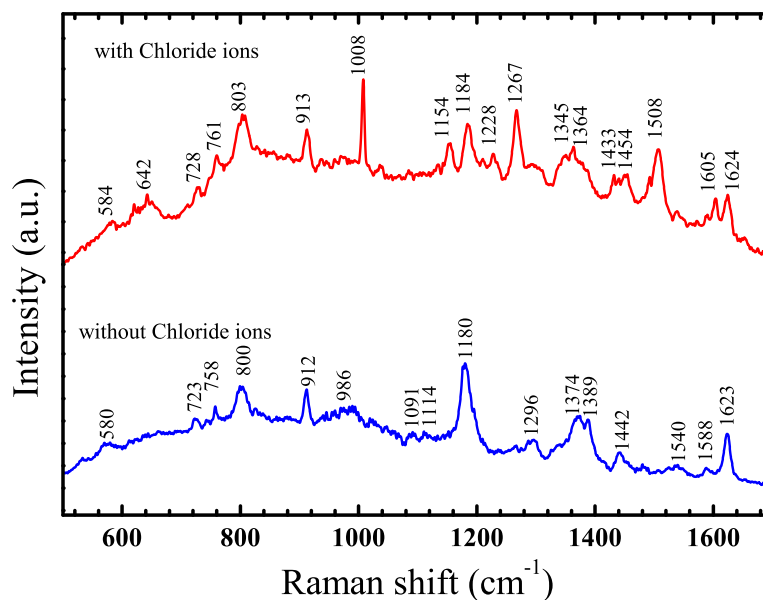


Figure 5.6: SERS spectra of p300 in the absence and presence of 0.3 mM NaCl. The concentration of the p300 was same for both the cases.

Although the role of aggregating agents in SERS has been studied earlier with respect to small molecules [113], proteins are yet to be investigated in this regard. Upon addition of a small quantity of NaCl or KCl to the solution containing the analyte and nanoparticles, one observes a large enhancement in the SERS signal. As it is known, the enhancement of Raman bands in SERS is governed by both electromagnetic enhancement and the chemical enhancement [6, 21]. Upon addition of small concentrations of chloride ions to the protein-nanoparticle composite, there is a nanoparticle aggregate formed around the proteins. This will cause a further enhancement in the above-mentioned mechanisms due to

- an enhanced plasmon coupling as a result of the aggregation of the nanopar-

Table 5.2: Assignment of Raman Bands in the SERS Spectra of p300 + 0.3 mM NaCl

Raman shift	Band assignment
1624	amide I
1605	Trp, Tyr, and/or Phe(ν_{8a})
1508	His
1454	$\delta(\text{CH}_2)$
1433	His and/or Trp
1364	Trp
1345	$\delta(\text{CH})$ and/or Trp
1267	amide III
1184	Tyr and Phe
1153	$\nu(\text{CN})$
1008	Phe
913	$\nu(\text{C-COO}^-)$
803	Tyr
761	Trp or His
728	$\delta(\text{COO}^-)$
642	Tyr
584	Trp

ticles,

- an increased charge-transfer pathway between the metal-protein system, and
- the anion-induced reorientation of adsorbed protein [113].

These reasons will account not only for the enhanced Raman signal intensity, but also for the appearance of new vibrational modes upon addition of chloride ions in the solution.

Figure 5.6 shows the SERS spectrum of p300 in the presence of 0.3 mM NaCl. Table 5.2 shows the frequencies of the most important SERS bands of p300 and their proposed band assignments for the chloride ion case. We observe new modes of vibrations arising upon the addition of chloride ions (see Figure 5.6). We can clearly see new Raman bands around 1008, 1267, 1508 and 1605 cm^{-1} , which have been assigned to the groups Phe, C=O stretching of the α helix, histidine (His)/Trp,

and Tyr and/or Phe, respectively. Note that p300 contains 68 His residues along with several Trp, Tyr and Phe as mentioned earlier. Therefore, we expect these aromatic amino acids to interact strongly with Ag nanoparticles.

5.2.2.3 SERS Spectra of p300 adsorbed to silver nanoparticles dried over a glass substrate

The SERS spectra of p300 obtained by normal method (see Experimental section) is shown as blue coloured spectra in Figure 5.7. Enhanced Raman signals for the bands around 634, 721, 1013, and 1268 cm^{-1} are observed. These bands pertain to stretching vibrations of Phe and C=O and are absent in SERS spectra of p300 recorded in the aqueous solution (compare with Figure 5.5). It is important to note the absence of the amide vibration in Figure 5.7. The absence of amide bands could be due to the fact that these groups are not in the close proximity to silver surface, since the silver colloids are immobilized on the glass slides a priori. This also could be due to screening of the amide groups by the aromatic groups on the protein surface [110]. In the absence of a short-range component of the SERS mechanism, the amide bands can disappear in the SERS spectra. SERS spectra were also obtained by preparing the sample using another method which we call the *sandwich method* (see the Experimental section). The red curve in Figure 5.7 shows the SERS spectra of p300 obtained by this method. Here, we observe a weak amide I band around 1672 cm^{-1} along with many other modes, which were absent in the SERS spectra obtained by normal method. It is interesting to observe that the Raman spectrum of p300 prepared by the sandwich technique (red plot in Figure 5.7) resembles the Raman spectrum of the p300 in aqueous solution in the presence of chloride ion (red plot in Figure 5.6). In the sandwich method, we add the nanoparticles along with the protein on top of a dried silver nanoparticle layer,

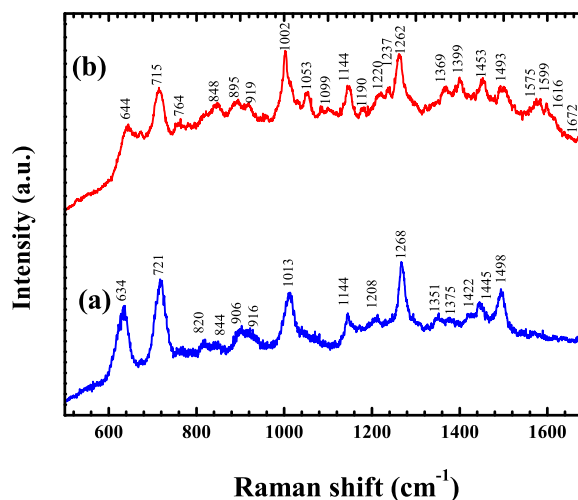


Figure 5.7: SERS spectra of p300 in the nonaqueous form on substrates prepared by (a) method I and (b) method II (the Experimental Details gives the details of the substrate preparation). The concentration of the p300 was again $40 \text{ ng}/\mu\text{L}$.

which allows a better adsorption of the protein to the silver surface, and hence facilitate an environment to retain minute amounts of water between the silver nanoparticles. Although the enhancement of the Raman signal obtained by this method is less when compared to that of the spectra obtained in aqueous form, this technique may still provide a unique technique to perform temperature dependent SERS studies.

5.2.3 Conclusions

For the first time, SERS was performed on p300 in aqueous and dry forms. The SERS spectra suggest the presence of α helix, aromatic ring structures like Phe, Tyr, Trp, His, and aliphatic structures such as Asp, Glu, and C-terminus groups in p300. The presence of these Raman bands in the SERS of the protein provides an important tool for studying drug-protein interactions. In the absence of full-length

crystallographic data of proteins, SERS can act as a very useful technique to obtain structural information. The presence of small concentrations of NaCl leads to aggregation of nanoparticles leading to a better adsorption of silver nanoparticles to the proteins. The chloride ion could increase the sensitivity of SERS experiments due to larger enhancement in Raman signals more or less retaining the Raman spectra of the proteins. A new method called the *sandwich technique*, which could provide an alternate method for recording SERS spectra of proteins without the aqueous medium was discussed. Using this method, we were able to record the Raman spectra of p300, which resembled its spectra in aqueous medium. This method could pave the way to perform SERS experiments in ultrahigh vacuum conditions. Furthermore, SERS analysis can be used to study protein-ligand interactions, like p300-HAT modulator interaction, which is the theme of the next section.

5.3 Interaction of p300 with small molecules: Probed by SERS

Proteins are important macromolecules which exhibit highly specific structure-function correlation. As described earlier, p300 is one such macromolecule present in human cells, which act as Histone acetyltransferase(HAT) enzymes. It has important implications in functioning of cells, and acts as transcriptional coactivator. Mutation in the HAT active site of p300 abolishes transactivation capability of p300. Dysfunction of p300 is often associated with manifestation of several diseases including cancer, cardiac hypertrophy, asthma, and diabetes. It is important with respect to therapeutics that HAT activation and inhibition of p300 is not only well understood, but also controlled at will. This has motivated biochemists to design

molecules which specifically activate or inhibit the functioning of HAT. However, very few small molecule modulators of histone acetyltransferases are known so far. Availability of recombinant HATs has made it possible to synthesize and isolate HAT inhibitors, of late. These include the p300 specific synthetic and natural inhibitor Lysyl CoA [114] and Curcumin [115], respectively. Recently, Kundu and coworkers isolated the first naturally occurring HAT inhibitor anacardic acid from cashew nut shell-liquid and garcinol from *garcinia indica*, which are nonspecific inhibitors of p300, CBP, and PCAF (p300/CBP associated factor) [88, 116]. By using anacardic acid as syntony, they have synthesized amide derivative (N-(4-chloro-3-trifluoromethyl-phenyl)-2-ethoxy-6-pentadecyl-benzamide) (CTPB) and N-(4-chloro-3-trifluoromethyl-phenyl)-2-ethoxy-benzamide (CTB), which are the only known small molecule activator of any histone acetyltransferase, in this case, p300. Significantly, CTB and CTPB are specific to p300 HAT activity, and hence important for therapeutics. In this section we show that SERS can be harnessed to track the specific interaction between a protein (p300) and an activator or inhibitor molecule. The activator molecules used in this study are CTPB and their derivatives, and inhibitor molecules used are garcinol and their derivatives. Figure 5.8 shows the schematic of the SERS method used to probe the protein-molecule interaction. The strategy was to obtain the SERS spectra of the protein adsorbed to nanoparticles in the absence of any small molecules. Later, the protein was allowed to interact with the small molecules in the absence of any nanoparticle. After sufficient duration, the complex of protein-molecule was adsorbed to nanoparticles in solution phase, and SERS spectrum was recorded. By comparing the SERS spectra of p300 in molecule-free state and in molecule-bound state, insights can be obtained to understand the protein-molecule interactions. In the present case, both activating and inhibiting molecules were water insoluble, and hence did not exhibit

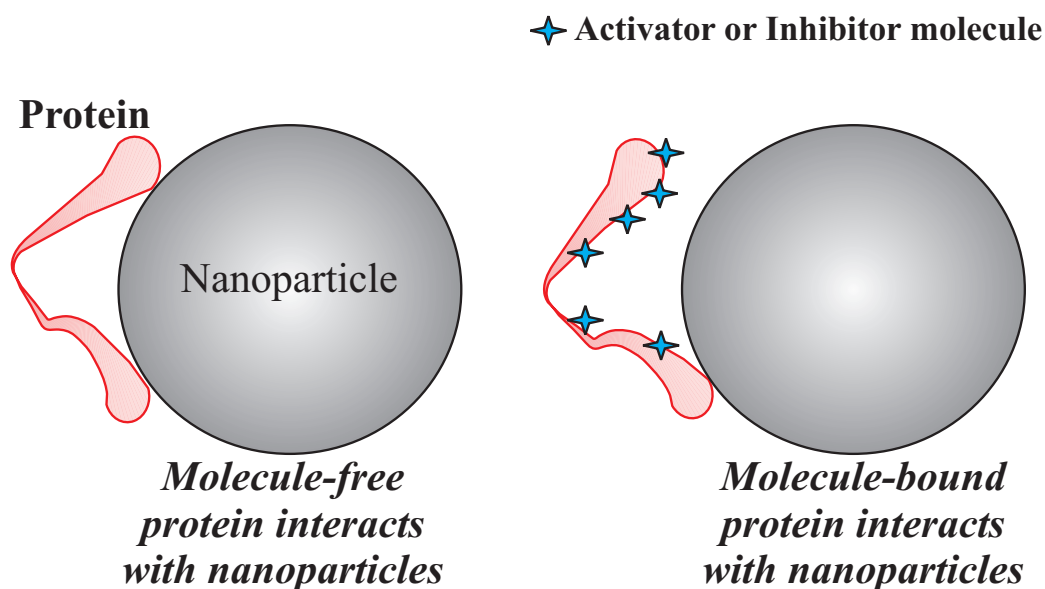


Figure 5.8: Schematic of protein-molecule interaction probed by SERS

any SERS spectra of their own in solution phase, which would have interfered as noise in SERS spectra of p300. This was an important advantage, and specific to cases where small molecules do not interact with nanoparticles in solution phase.

5.3.1 Experimental Details

The Raman experiments were carried out using the 632.8 nm laser source using the experimental setup described in Chapter 2. The laser power used at the sample was 6 mW. To perform SERS, we have prepared the citrate-reduced silver colloidal solution following the standard method of Lee and Meisel [29]. We dissolved 50 μL silver colloid to 20 μL of p300 solution or a mixture of 2 μL of activator or inhibitor molecule and 20 μL of p300 solution on a cavity slide under the microscope. The typical accumulation times were 3-5 min. The preincubation time for p300 and compound to interact was same as used in biochemical experiments [53, 54].

5.3.2 Results and Discussion

5.3.2.1 Interaction of p300 with activator molecules

Interactions between p300 and derivatives of CTB

Figure 5.9 shows the three derivatives of CTB and their respective HAT activity on p300. Note that control and DMSO (solvent) activities are also displayed. It is important to note that these three molecules are similar to each other in structure, except for the positions of a Cl atom, and a CF₃ group. Interestingly, it can

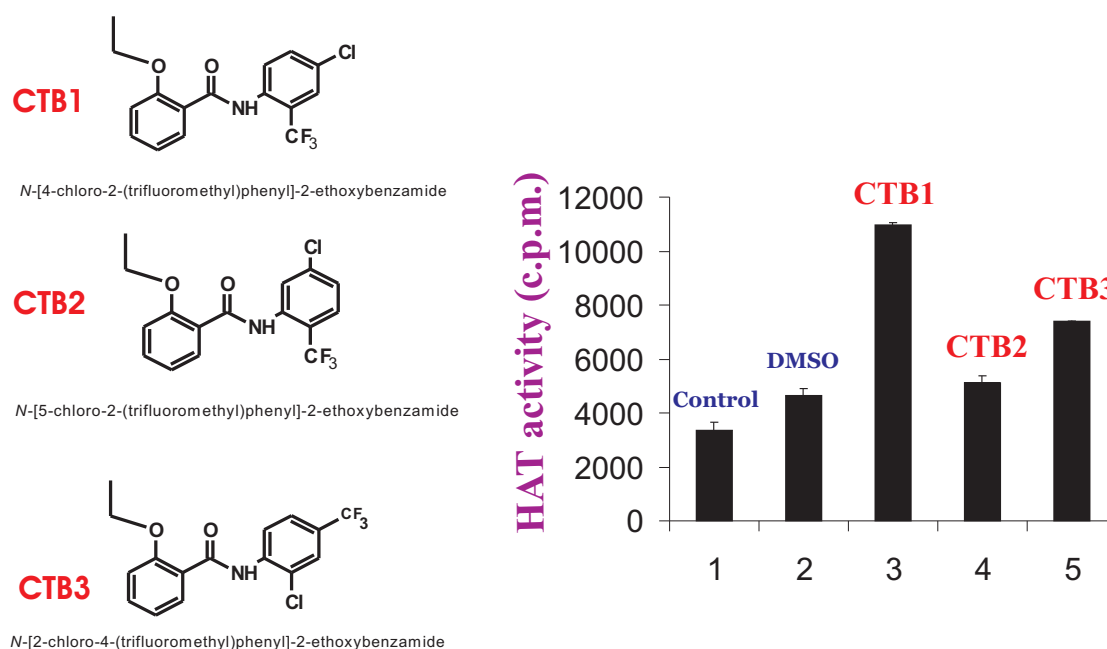


Figure 5.9: Molecular formulae of CTB derivatives and their respective HAT activity on p300.

be observed that the influence of these molecules on the HAT activity of p300 differs significantly from each other despite their structure being similar [54]. CTB1 activates p300 to maximum extent followed by CTB3. Whereas, the activation of CTB2 was observed to be minimal. In order to reveal the interaction of these derivatives with p300, and hence correlate them to small structural changes in

p300, we have used a unique approach to monitor the structural change of the enzyme upon binding of the compounds by using SERS. Whenever a molecule binds to the protein, the binding sites are distanced from the noble metal surface and would affect the Raman modes such that there is a reduction in intensity or disappearance. The change in orientation of these groups in the protein with respect to the nanoparticle surface could also lead to the disappearance of the Raman mode. SERS is sensitive not only to the distance between the molecule and metal surface, but also to the orientation of the molecule with respect to the metal surface, as discussed in Chapter 1. Therefore, upon binding of a molecule to the surface of the protein, we expect the SERS of the protein to change. Figure 5.10 shows the

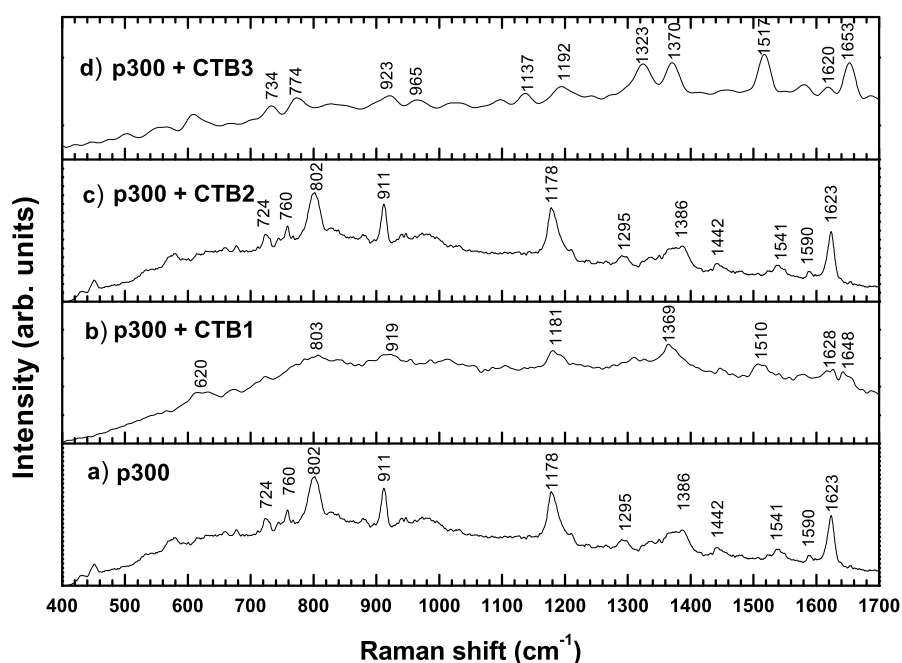


Figure 5.10: SERS spectrum of molecule-free p300 compared with SERS spectrum of p300+CTB1, p300+CTB2 and p300+CTB3

SERS spectra of molecule-free p300 compared with molecule-bound p300. All the Raman modes of vibrations discussed in this section refers to the band assignment shown in Tabel 5.1. We observe that the SERS spectra of p300 bound to CTB1 shows a significant change in the intensity and band position when compared to SERS spectra of molecule-free p300. Whereas, SERS spectra of p300 interacting with CTB3(which shows the least HAT activation) is very similar to SERS spectrum of molecule-free p300. Both CTB1 and CTB2 have electronegative groups, namely, Cl and CF₃ groups at the para position of the phenyl group of the CTB. The SERS spectra indeed show an increase in the random coils at the expense of α helix (compare intensities of 1623, 1295, and 1654 cm⁻¹) as well as large changes to ring-structured amino acids like Trp, Tyr, His, and Phe in the structure of the p300 upon addition of these compounds(compare Figure 5.10 a, b, and d). The HAT activity induced by CTB3 is relatively low as compared to CTB1 but is much larger than CTB2. Therefore, we infer that the presence of the CF₃ group at the meta position also plays an important role in the activation. It also implies that substitution at the meta and para positions in the phenyl group of CTB with strong electronegative group, such as F, may lead to stronger activation of p300 HAT activity. So, in general, the activators of p300 mainly induce changes to the α helix and the ring-structured amino acids of the active domain of the protein.

p300 interaction with CTB and CTPB: a comparison

The kinetic analysis of the activation of p300 activity by CTPB and CTB suggests that in the presence of compounds, activation barrier is reduced thereby enhancing the enzyme activity [54] (CTB and CTPB are the same molecules which were discussed in chapter 4, for their structure, please see Figure 4.1). Presumably, binding of the compounds to the enzyme leads to causal change in the enzyme structure to enhance the acetylation activity. Figure 5.11 shows the SERS spectra

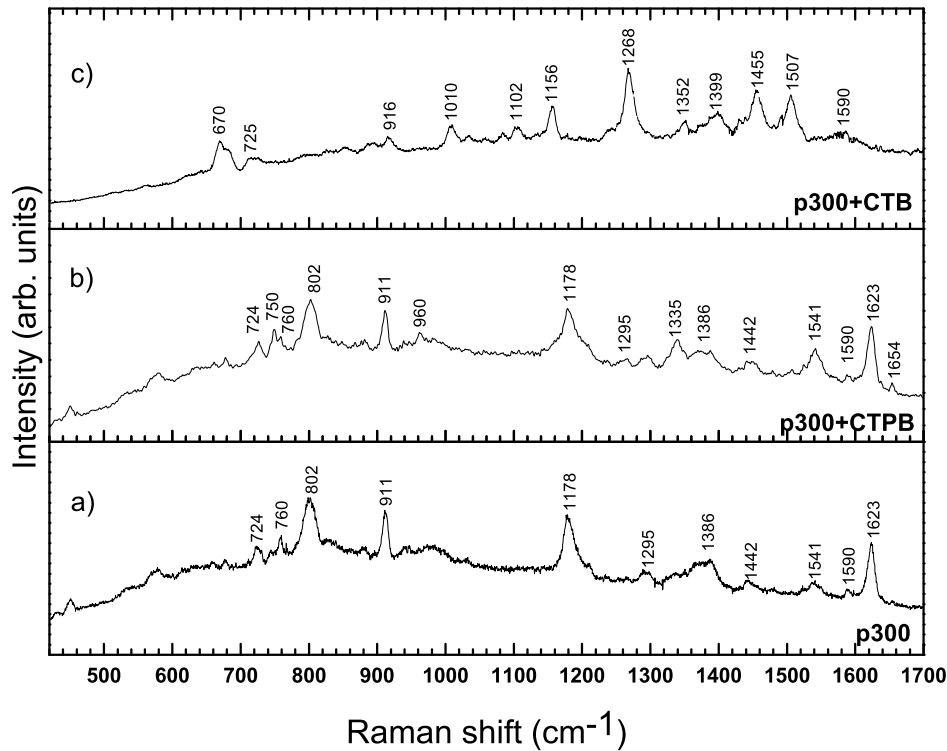


Figure 5.11: SERS spectra of a)p300; b)p300 bound to CTPB; c)p300 bound to CTB. Note that CTB induces greater change to SERS spectra of p300 than CTPB.

of (a) p300, (b) p300 with CTPB, and (c) p300 with CTB. We observe spectral changes in SERS of p300 in the presence of CTPB and CTB (Figure 5.11, compare a vs b and c). In the case of CTPB (Figure 5.11b), the SERS spectrum of p300 does not show large-scale changes. The appearance or increase in intensity of the Raman modes 1654, 1335, and 960 cm^{-1} suggests that the binding of CTPB is predominant to the amide groups of the α helix and β sheets. In the case of CTB (Figure 5.11c), we observe a comparatively larger change in the SERS spectra of p300. CTB also binds to the amide groups of the α helix and β sheets like CTPB, but the binding sight might be different compared to CTPB as we observe disappearance of both 1623 cm^{-1} and 1654 cm^{-1} Raman modes. Along with this, the

CTB has a strong effect on the binding sites as shown by the large shifts in the peaks in the region $1150\text{-}1550\text{ cm}^{-1}$, which are related to the amide II and aromatic amino acids (tryptophans (Trp), tyrosines (Tyr), phenylalanines (Phe), and histidines (His)). The shifts in the Raman peaks are between 10 to 35 cm^{-1} . This is a substantial effect and can be caused either by a strong hydrogen bonding of the molecule to the protein or a hydrophobic interaction between the molecule and the nanoparticle. The strong interaction of CTB with amide group is also reflected in the appearance of a new mode around 1010 cm^{-1} and 1102 cm^{-1} (symmetric and asymmetric vibrations of C-C-N) and disappearance of the 802 cm^{-1} mode (Tyr). The appearance of a mode near 670 cm^{-1} signifies the interaction of CTB to the carboxyl groups of aliphatic amino acids. All these observations suggest that although both CTPB and CTB bind to p300, affecting the structure of the enzyme, CTB has a greater effect on localized structural alteration.

5.3.2.2 Interaction of p300 with inhibitor molecules

As described before, because of its involvement in many important cellular events, dysfunction of p300 may be the underlying causes of several diseases, including a few types of cancers, cardiac hypertrophy, asthma, and diabetes. HAT activity of p300 therefore is being considered as a target for the new generation therapeutics. Unlike histone deacetylase inhibitors, the number of HAT modulators (activator and inhibitors) discovered so far is scanty. Recently, isothiazolones-based modulators have been designed that inhibits both p300 and PCAF [117]. The search for specific natural small-molecule modulators of HATs succeeded when anacardic acid from cashew nut-shell liquid was found as a potent inhibitor of p300 and PCAF. Unfortunately, these compounds were found to have poor cellmembrane- permeability potential [88]. The lead development in the field was initiated when another

natural small-molecule inhibitor of HATs, garcinol, a polyisoprenylated benzophenone derivative from *Garcinia indica* fruit rind was discovered [116]. Garcinol was

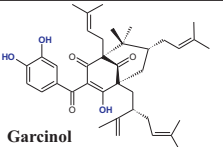
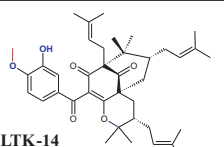
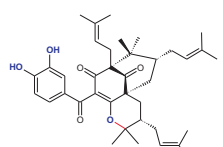
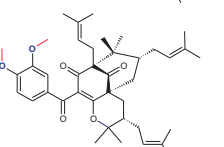
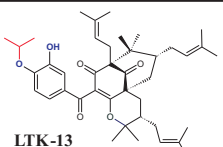
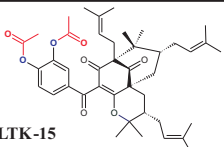
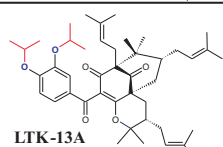
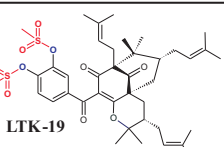
Compound	Specificity	IC50	Cell Toxicity	Compound	Specificity	IC50	Cell Toxicity
 Garcinol	Non specific	p300-7 μM PCAF-5 μM	Highly toxic	 LTK-14	Specific to p300	5-7 μM	Non toxic
 Isogarcinol	Non specific	p300-7 μM PCAF-5 μM	Highly toxic	 LTK-14A	Inactive	-	Not tested
 LTK-13	Specific to p300	5-7 μM	Non toxic	 LTK-15	Inactive	-	Not tested
 LTK-13A	Inactive	-	Not tested	 LTK-19	specific to p300	5-7 μM	Non toxic

Figure 5.12: Structure and specificity of inhibition of garcinol, isogarcinol and their derivatives

found to be a nonspecific HAT inhibitor (HATi) but highly permeable to cultured cells and a potent inhibitor of histone acetylation in vivo. The nonspecific nature of garcinol made it highly cytotoxic. Therefore, the potential use of garcinol to target p300 for understanding the physiological role of HATs or to develop a therapeutic molecule is less likely. These limitations of garcinol inspired biochemists to synthesize several derivatives of this potent inhibitor to find out specific and less toxic HAT inhibitors. Among nearly 50 derivatives synthesized from garcinol, three were found to be highly specific for HAT activity of p300, the details of which are shown in Figure 5.12. LTK-13, 14 and 19 were found to be specific

inhibitor of p300. In order to elucidate these specific interactions between p300 and their various inhibitors, we have used SERS. Figure 5.13 shows the SERS spectra of p300 in comparison with inhibitor-bound p300. The SERS spectra of p300 in the presence of dimethyl sulfoxide (DMSO)-which is the solvent for inhibitors- was also recorded as a control. The p300 spectrum, as discussed earlier, is dominated

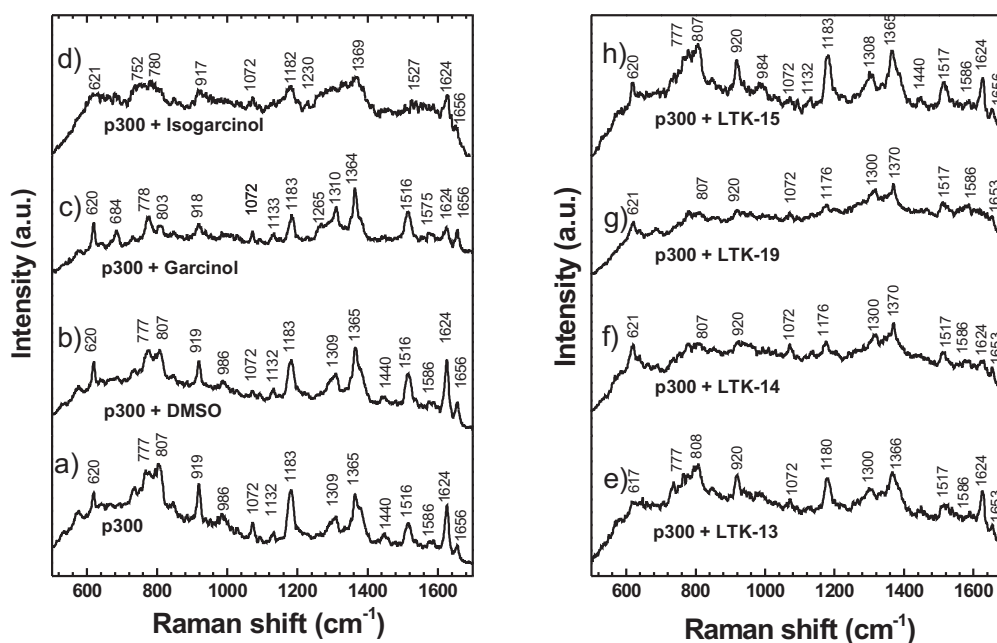


Figure 5.13: SERS spectra of a) p300; b) p300 + DMSO; c) p300 + Garcinol; d) p300 + Isogarcinol; e) p300 + LTK-13; f) p300 + LTK-14; g) p300 + LTK-19; h) p300 + LTK-15. Laser excitation - 632.81 nm; laser power at the sample - 8 mW; accumulation time - 180 sec.

with the Raman features associated with ring-structured amino acids tryptophan (Trp), tyrosine (Tyr), phenylalanine (Phe), and histidine (His). p300 is known to contain several units of Trp, Tyr, Phe, and His in it. The spectrum of p300 also exhibits prominent amide I band around 1624 cm^{-1} and 1656 cm^{-1} associated with the α helix and β sheet structure, respectively. The spectrum of p300 with and without DMSO were found to be quite similar (Figures 5.13a and b), suggesting that there is no contribution from the DMSO to the SERS spectrum of

p300. The aromatic ligands, such as garcinol and IG, would form hydrogen bonds and/or have hydrophobic interactions with the protein resulting in the change of the structure of the protein. Since Raman spectrum has a correspondence to the secondary structure of protein, we expect the changes in Raman modes due to the interaction between the inhibitor and the protein. It is interesting to note that there is a small difference in the chemical structures of garcinol and IG molecules, namely, the presence of a hydroxyl group in the garcinol instead of the oxygen bridging in IG as shown in Figure 5.12. SERS spectra of p300 in the presence of these molecules are shown in Figures 5.13 c and d. The SERS spectrum of p300 bound with garcinol shows changes mostly to the amide bands of the α helix, like 1624 cm^{-1} and 1296 cm^{-1} , carboxylic group vibrations of the aliphatic amino acids (985 cm^{-1} and 684 cm^{-1}), and certain Tyr modes, like 803 cm^{-1} . On the other hand, IG causes a large-scale change to the p300 spectra. Along with the modes affected in the case of garcinol, the binding of IG also affects all the modes related to Tyr, Trp, Phe, and His. Next, we looked at the derivatives of IG, namely LTK-13, -14, -15, and -19. The Figure 5.13 shows the SERS spectra of p300 complexes with LTK-13 (Figure 5.13e), LTK-14 (Figure 5.13f), LTK-19(Figure 5.13g), and LTK-15(Figure 5.13h). It is important to note that upon addition of LTK-15, the inactive IG derivative, there is no change to the SERS spectra of p300 (Figure 2h). In the case of LTK-13, the change in the p300 spectra is limited to the amide bands of the α helix (1656 cm^{-1} and 1517 cm^{-1}) and certain carboxylic groups of the aliphatic amino acids (737 cm^{-1} and 617 cm^{-1}). On the other hand, both LTK-14 and LTK-19 causes large-scale changes in the p300 spectra. Like in the case of IG, binding of both LTK-14 and -19 (specific inhibitors) affects not only the amide modes but also all the modes related to Trp, Tyr, Phe, and His. However, unlike in the case of IG, LTK-14 and -19 binds to p300, the carboxylic side group

of the aliphatic amino acid represented by 621 cm^{-1} is unaffected (compare Figure 5.13d with 5.13f and 5.13g). Taken together, these data suggest that the specific and nonspecific inhibitors of p300 bind to the amide groups of α helix, and thereby differentially alter the enzyme structure. This mechanism can be further used as a qualitative tool to probe protein-inhibitor interaction.

5.3.3 Conclusion

The interaction of p300 with its activators and inhibitors were probed using SERS technique. This method offers a unique way to probe protein-molecule interactions in special cases where the amount of protein is scarce. The role of distance-dependent electromagnetic enhancement plays an important role in this method. By comparing the SERS spectral changes in molecule-free p300 and molecule-bound p300, we could elucidate small yet subtle changes in the secondary structure in the protein. These structural changes corroborate the biochemical assays which reveal activity modulation of the protein when bound to the molecules. In the light of therapeutics, one could further harness this method to find specific structural changes and reorientation of protein in the presence of an external activator or inhibitor.

5.4 Structural changes in p300 HAT domain: probed by SERS

The acetylation and deacetylation of histone and non-histone proteins play a key role in the regulation of gene expression, cell growth, and differentiation and in maintaining cellular homeostasis in the eukaryotic cells [103, 118]. A balance between acetylation and deacetylation of the proteins are brought about by two important classes of histone modifying enzymes, histone acetyltransferases (HATs) and histone deacetylases (HDACs) [118]. Among the HAT family, the p300/CBP group of HATs are most widely studied and have been identified as major enzymes that acetylate protein with a range of biological functions. The intrinsic histone acetyltransferase (HAT) activity of p300 plays important roles in the transcriptional coactivation of p53, p73, steroid hormone response [103, 119]. The HAT activity of p300 is regulated by several mechanisms, which include methylation and autoacetylation [120, 121]. p300 HAT domain (p300HD) gets extensively autoacetylated, which is a highly cooperative process and is intermolecular in nature. The autoacetylation of p300 dramatically enhances its activity and thereby increases the HAT activity dependent signal via the acetylation of histone and non-histone proteins. During autoacetylation mechanism, there is a conformational change induced in the secondary structure of p300 HAT domain. Although autoacetylation mediated structural alteration of p300 has been realized as one of the key mechanisms of action, the direct evidence for the conformational changes was yet to be demonstrated. We have utilized SERS as an effective probe to determine the subtle structural change in p300 HAT domain. The strategy was to perform SERS on p300 HAT domain before and after the autoacetylation, and analyze the SERS modes of them. Any differences in the vibrational modes of the protein can

reveal insights into the secondary structural changes induced by autoacetylation.

5.4.1 Experimental details

To perform SERS of p300HD, it was adsorbed on the silver nanoparticles prepared by Lee and Meisel method [29]. As in the case of p300, it has been reported that the adsorption of silver nanoparticles does not alter the function of p300 HAT domain [122]. All the measurements were performed using the water immersion objective of custom built Raman microscope whose details can be found in Chapter 2. For the present study, 532 nm frequency doubled Nd-YAG laser was used. The accumulation time was 30 seconds. For the SERS measurements, p300 HAT domain solution (or its autoacetylated counterpart) was mixed with silver nanoparticles in the ratio 1 : 4, and deposited on a glass slide with single cavity. The deuterated SERS spectrum was obtained by the same method as explained for p300 in the section 5.2.1.1, without any modifications.

5.4.2 Results and Discussion

SERS can be utilized as an effective probe to detect and characterize biomolecules available at low concentrations as revealed in previous section. The p300 HAT domain (p300HD) also belongs to the category of biomolecules which are available at scarce quantity. Figure 5.14 shows the SERS spectra of p300 HAT domain. In order to confirm the amide vibrations, the SERS spectra of p300HD was recorded in D₂O. Figure 5.15 compares the SERS spectrum of p300HD in H₂O and D₂O. The BC100 buffer used for these experiments were same as that used for p300 studies, and control spectrum of the buffer is shown in Figure 5.15. Upon deuteration of proteins, most of the hydrogen in the amide groups will be replaced by the heavier

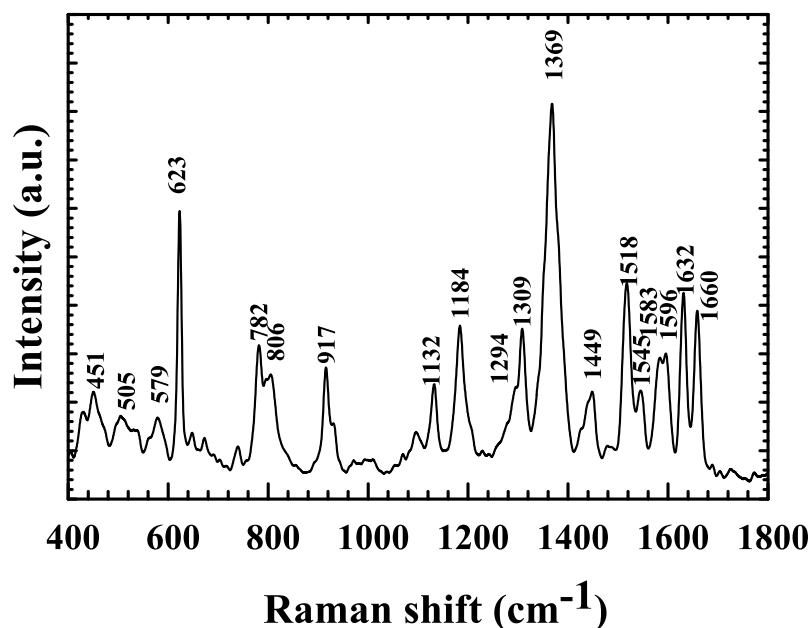


Figure 5.14: SERS spectra of p300 HAT domain

deuterium. This will increase the reduced mass of the vibrating unit (oscillator), which is inversely proportional to the vibrational frequency. Therefore, one should expect a decrease (red-shift) in the amide vibrations. As expected, we observed a red-shift in amide bands. The shifts in the frequency for the amide I and II bands of p300HD were found to be 7 and 5 cm⁻¹, respectively.

Table 5.3 shows the SERS band assignments of the HAT domain. Modes have been assigned in comparison to the SERS spectra of the parent protein p300 and using the standard amino acids and proteins band assignments. It is evident that the spectrum is dominated by SERS modes of ring-structure amino acids: tryptophan (Trp), tyrosine (Tyr), and phenylalanine (Phe), which are characteristic of SERS of any protein. The report on experiments using mass spectrometry has revealed that the active sites of p300HD being modified due to autoacetyla-

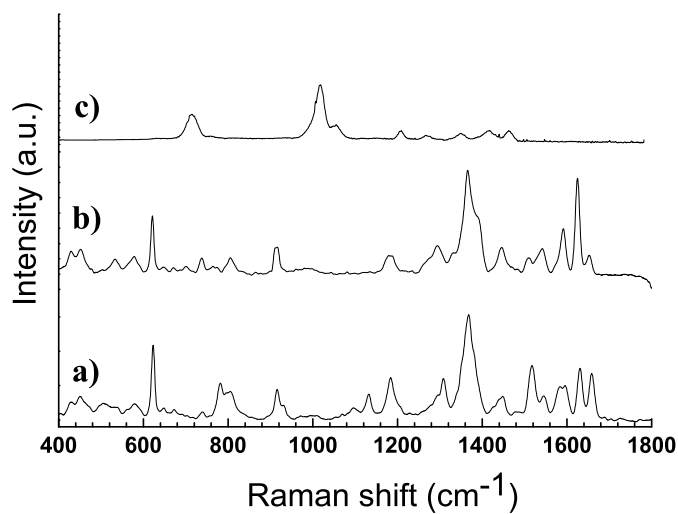


Figure 5.15: SERS of a) p300 HAT domain; b) deuterated p300 HAT domain; c) buffer

Table 5.3: SERS band assignments of p300 HAT domain

Raman shift	Band assignment
1660	amide I (α helix)
1632	amide I (random coil)
1596	Trp, Tyr, and/or Phe
1583	$\nu_{as}(\text{COO}^-)$, His, Trp
1545	Trp, Tyr, and/or Phe
1518	amide II and/or Trp
1449	$\delta(\text{CH}_2)$
1369	$\nu_{as}(\text{COO}^-)$
1303	$\omega(\text{CH}_2)$
1294	amide III (α helix)
1184	Phe
1132	$\nu_{as}(\text{C}_\alpha\text{CN})$
917	$\nu(\text{C-COO}^-)$
806	Tyr and/or $\nu_{as}(\text{C-S-C})$
782	$\delta(\text{COO}^-)$
623	Trp
579	Phe
505	$\nu(\text{S-S})$

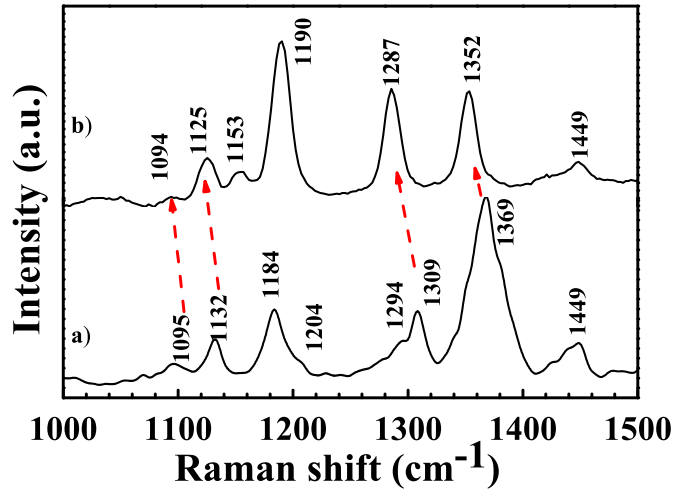


Figure 5.16: SERS of (I) HAT domain compared with (II) autoacetylated HAT domain. The red arrows indicate the softening of some modes. The spectrum has been vertically shifted for clarity.

tion [57]. In order to corroborate these observations, we have performed SERS of fully autoacetylated p300HD and compared it with normal, partially acetylated HAT domain as shown in Figure 5.16. There is a marked change in the modes pertaining to symmetric stretching of COO^- (1369 cm^{-1}), amide III (1294 cm^{-1}), Phe (1184 cm^{-1}), and asymmetric stretching of C_αCN (1132 cm^{-1}). We observe not only a change in intensity of these modes but also softening of some modes (Figure 5.16b). Softening of the modes implies decrease in the Raman shift. This observed softening of modes (10 cm^{-1}), in fact, signifies bond weakening due to the interaction between various groups upon autoacetylation. Also, it was interesting to observe that some of the modes like 1449 and 1094 cm^{-1} that pertain to $\delta(\text{CH}_2)$ and proline (Pro) do not show any significant shifts after the autoacetylation. The possible reason for such an observation is that upon autoacetylation, there could be structural changes at specific sites of p300HD, which leads to subtle changes in

SERS spectrum. Hence, these spectral changes indicate structural reorganization of the HAT domain after the complete autoacetylation.

It is to be noted that, unlike conventional Raman spectroscopy, SERS probes vibrational modes of groups that are in close proximity to the metal surface. This would be reflected as intensity changes due to the distance dependent electromagnetic enhancement and the surface selection rules, where the orientation of the molecule on the metal surface determines the enhancement of the vibrational modes. Therefore, all these conditions suffice to make SERS sensitive to probe the structural modifications of macromolecules near the surface of nanoparticles, as in the present case. Furthermore, these data also suggest that SERS could be used to monitor the structural changes in the other self-modifying proteins like kinases, methyltransferases.

5.4.3 Conclusion

Autoacetylation induced specific structural changes in p300 HAT domain was probed through SERS. This technique may be further evolved to study site specific structural changes in protein, especially at the surface. It is important to note that all the above mentioned experiments were performed in solution phase at low concentrations of protein. This provides a significant advantage to study subtle secondary structural changes of protein under physiological conditions, which is not viable to probes like x-ray crystallography. Although the in vitro studies like these show promising results, the final aim should be to perform experiments in vivo. Many research laboratories around the world are aiming to achieve the same.

CHAPTER 6

DIAGNOSTIC APPLICATION OF SERRS: DETECTION AND DISCRIMINATION OF HIV-1 SUBTYPES

This chapter constitutes the following patent:

1. *A high sensitivity assay for molecular typing of biological samples using Surface enhanced Raman scattering*
Indian Patent applied (2007).

6.1 Motivation

Acquired Immune Deficiency Syndrome (AIDS) has been one of the deadliest diseases in the history of mankind, whose complete cure is yet to be achieved. The virus which causes this disease is called as Human Immuno-deficiency Virus(HIV), whose detection and characterization is of paramount interest to present day AIDS pathologist and scientists. The classification of HIV is as shown in Figure 6.1. HIV-1 and HIV-2 are the two strain prevalent, of which there are various

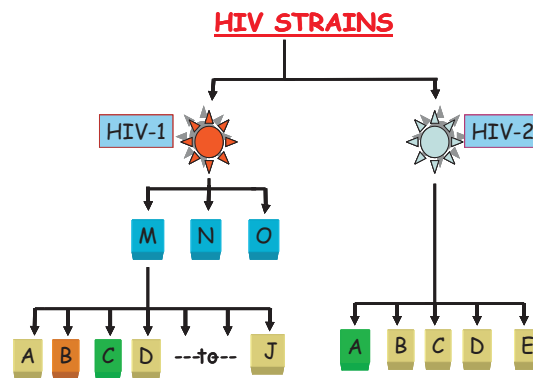


Figure 6.1: Classification of HIV

subtypes. Based on the genetic homology, HIV-1 is classified into 9 distinct and primary genetic subtypes designated A through J [123]. Distribution of the viral subtypes across the globe is non-uniform as shown in Figure 6.2. Additionally, epidemic outbreaks due to recombinant forms of the viruses are also becoming a serious problem in several geographical regions [124]. Depending on the epidemiologic incidence, recombinant viruses are of two types. First, circulating recombinant forms (CRF) are strains that have established successful infection in a geographical region or population and been characterized at the molecular level. Second, the unique recombinant forms (URF), viruses that have been isolated from limited number of subjects and not adequately characterized at the molecular level. The total numbers of molecularly characterized CRFs has increased to 34 presently

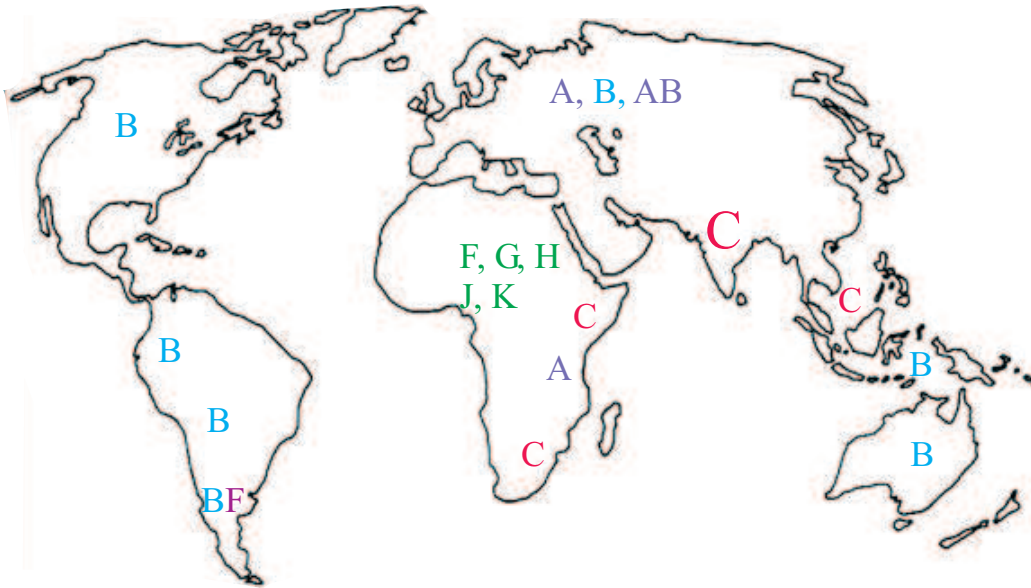


Figure 6.2: Non uniform global distribution of HIV subtypes.

from 8 during the past 2-3 years. On the other hand, a large number of URFs are being identified on a regular basis.

Generation and expansion of the recombinant viruses may throw serious challenges at disease intervention strategies like vaccine development and drug therapy [125, 126]. It is therefore important to develop simple and inexpensive diagnostic strategies to detect recombinant viruses on a priority basis. A wide range of techniques presently used for the subtype determination of the viral strains and recombinant viruses have limited application in molecular typing of the viral strains as they are too cumbersome, fail to target diverse viral subtypes, lead to contamination problem and/or expensive. The novel detection strategies must be technically simpler and inexpensive without sacrificing sensitivity and specificity. Especially for resource-limited countries like India, it is highly critical to develop molecular detection strategies that do not require template amplification strategy. Template amplification by Polymerase Chain Reaction (PCR) requires sophisticated diagnostic laboratories especially given the enormous potential for

contamination. PCR-dependent amplification is also expensive especially when TaqMan probe-based detection strategy is used. Keeping these practical limitations in view, we developed a novel strategy for the molecular characterization of HIV-1 subtypes and recombinant strains using Surface Enhanced Resonant Raman Scattering (SERRS) approach. The approach blends standard molecular biological techniques with the most powerful SERS detection strategy. Intact viral RNA molecules from biological samples are directly captured with oligonucleotides that are viral subtype- and window-specific and are covalently cross linked to chemically activated glass surface in a geographically addressable manner (in a microarray fashion). The captured viral RNA molecules are then detected with a different but single oligonucleotide probe that targets a sequence within the RNA that is highly conserved among diverse viral subtypes. The detector probe chemically conjugated to a Raman reporter and in conjunction with gold or silver nanoparticles permits high level molecular detection of the captured viral RNA molecule. Proof-of-the-concept experiments confirmed the practical viability of the novel strategy to detect viral RNA molecules in the absence of the template amplification. Our group is presently in the process of optimizing the novel detection strategy for efficient and simple molecular characterization of HIV-1 subtype and recombinants. Once optimized, the new SERS detection strategy can have wide application in the molecular detection of several pathogenic organisms and human physiological disorders.

6.2 Experimental details

We identified a novel and innovative strategy that can satisfy the above requirements and molecularly characterize a viral subtype, whose schematic is shown

in Figure 6.3. Our strategy is based on capturing the viral RNA using a capture

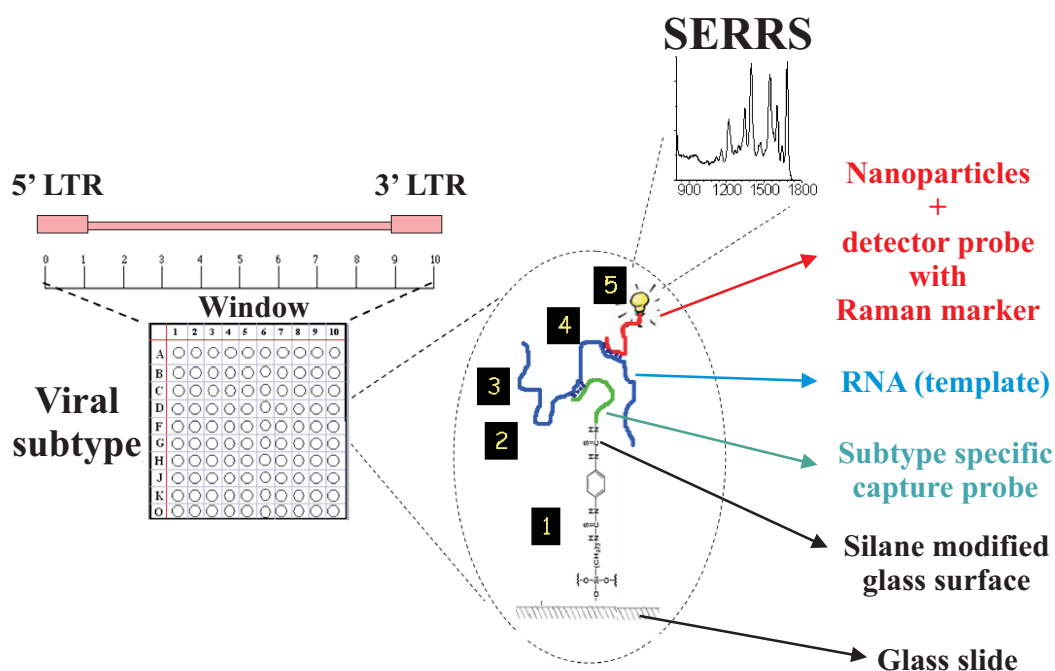


Figure 6.3: Schematic representation of genetic characterization of HIV-1 subtypes using SERRS. (1) Glass slide is silanized; (2) Subtype specific capture probe is attached ; (3) Specific RNA template from the sample adjoins the capture probe; (4) A Raman marker-tagged detector probe which is specific to subtype is captured by the template RNA and the rest is washed off by gentle flow of buffer solution. (5) Ag nanoparticles are introduced to bind the Raman marker and the SERRS spectra is recorded thereafter.

probe and detecting the latter with a reporter probe. An array of oligo-nucleotides that are subtype- and window-specific are amino-modified at the 5' end and are spotted in an array fashion on the surface of a silane-modified glass slide [127, 128]. The capture probes are designed to target 5-10 individual windows spanning the entire length of the virus each window consisting of 1000 base pairs. The viral RNA extracted from a biological sample is directly captured in a series of the windows of the microarray depending on the molecular nature of the viral subtype. The captured viral RNA is detected using one or a pool of two or three detector

probes that are tagged with a reporter molecule, a radio-isotope, fluorescent dye or a Raman marker(RM). The detector probes are highly conserved and detect all the diverse viral subtypes regardless of the subtype identity. The assay is characterized by moderate sensitivity when isotope- or fluorophore-labeled detector probe is used. However, the assay can attain high sensitivity when the detector probes are tagged to a Raman marker(rhodamine 6G in this case) as the latter can exploit the phenomenon of surface-enhanced resonance Raman scattering (SERRS). The high sensitivity of RM-tagged reporter probe can functionally compensate for the lack of template amplification in our strategy.

Amino-silane modification: A standard procedure was followed in this case [128]. Glass slides are cleaned for 30 min in a solution consisting of one-third hydrogen peroxide (30%) and two-thirds sulfuric acid (18 M), rinsed in distilled water, left for 10 min in boiling distilled water. Pre-cleaned microscope slides are immersed in 1% 3-aminopropyltrimethoxysilane solution in 95% acetone/water for 2min. The slides are washed ten times with acetone, 5 min per wash, dried for 45 min at 110⁰C, treated for 2 h with a solution of 0.2% 1,4 phenylene diisothiocyanate (PDC) solution in 10% pyridine/dimethyl formamide and washed with methanol and acetone. The activated glass may be stored indefinitely at 4⁰C in vacuum desiccators.

Fixation of aminated DNA to modified glass: Required quantity of amino modified capture probe is dissolved in solution of 1M NaCl and 10 mM sodium phosphate buffer and 2 μ L of this solution is placed on the glass slide as modified above followed by incubation at 37⁰C for 2 h [129]. The slide is washed with water twice for 2 min, blocked with 1% Bovine serum albumin with a gentle shaking at 45⁰C for 30 min and rinsed with distilled water twice for 2 min each time. The slide is ready for template capture.

Capture of the template nucleic acid: Desired quantity of the template nucleic acid (RNA or single-strand DNA) is dissolved in 5x SSPE and dispensed over the array. A glass cover-slip is over laid on the glass slide carefully. The slide assembly is incubated for 3 h at 60 C, followed by 0.3M PBS wash for two times. This is followed by incubation with the detector probe. Detector probe (R6G) in 5x SSPE is added to the slide followed by the overlay of the cover slip and the assembly is incubated at 65 C for 6 h. The array is washed with the following buffers in that order. One wash with each buffer: 2x SSC and 0.1 SDS at 65⁰C for 5 min, 0.2x SSC and 0.05x SSC at room temperature. The slide is spun to remove excess fluids, allowed to air dry and stored in dark until SERRS experiments were performed.

All the SERRS measurements were performed using costum built Raman microscope whose details can be found in Chapter 2. The absorption wavelength of R6G is around 520 nm, therefore we have employed 532 nm laser for SERRS measurements. The silver nanoparticles were prepared by the standard Lee and Meisel method [29].

6.3 Results and Discussion

The results of the two proof-of-concept experiments on detection and discrimination of subtype of HIV-1 will discussed in this section. First, we tested the capabilities of the concept by experimenting on single-stranded DNA of the viruses (not the real viral RNA). HIV-1 subtype-C capture probe N 730c and three different viruses (A, B and C) were used in the experiment. Figure 6.4 shows the multi-grooved glass slides with different loading of single stranded DNA used for the experiment. The SERRS results accompany the photograph in Figure 6.4. A 10-fold dilution series of each of the viruses was captured on the arrays and interro-

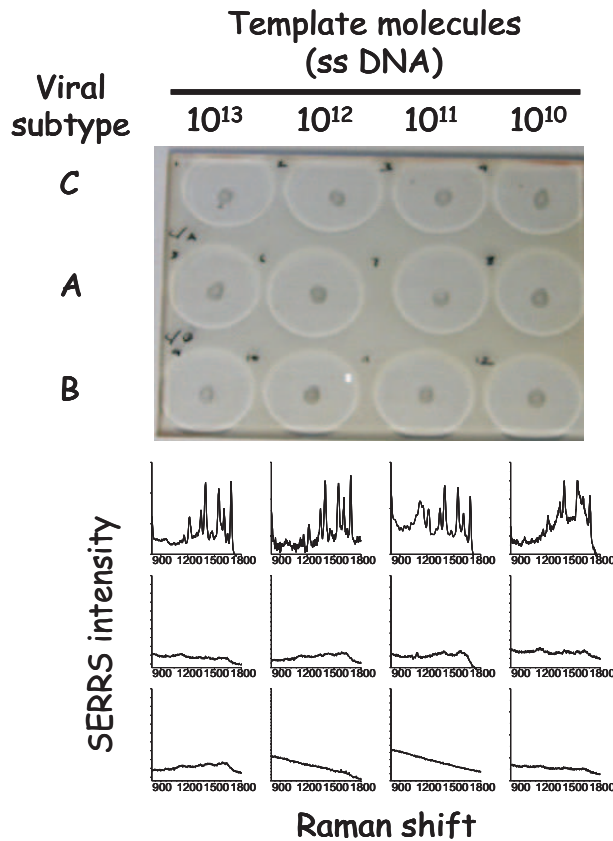


Figure 6.4: Photograph of multi-grooved glass slide used for SERRS assay to determine and distinguish HIV-1 subtypes A, B and C. The respective SERRS graphs are shown in the bottom half. SERRS signals are observed only for the first row (subtype C) highlighting the specificity of the assay.

gated using a single detector probe. Subtype-specific SERRS signals were detected only when the probe and subtype matched (top row) but not with subtypes A and B thus proving specificity of the assay. Sensitivity of the assay was approximately 10^3 molecules with a 1 second acquisition time.

Next, we performed the experiment to test the sensitivity on real HIV B type virus. For this Subtype-B and -C viruses were pelleted from 500 μ l of culture supernatant of HEL293 cells transiently transfected with the molecular clones. Viral pellet was dissolved in appropriate buffer with detergents to release the viral RNA and directly used in the experiment. Subtype-B capture probe (N729B) was cova-

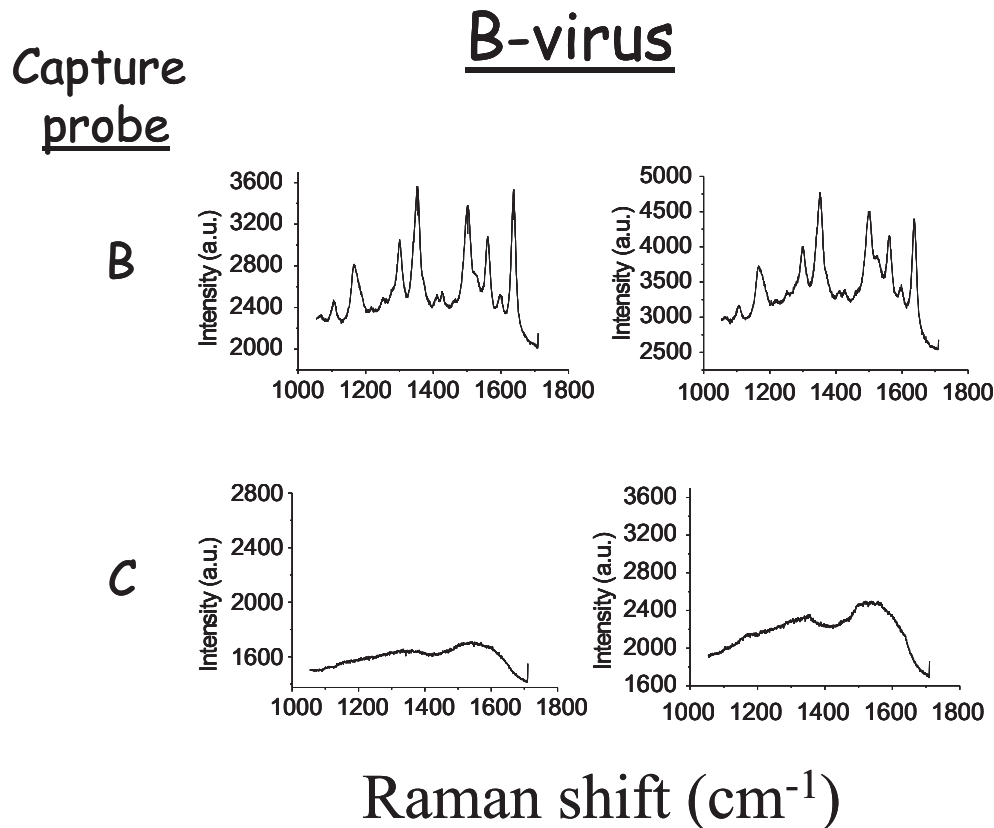


Figure 6.5: SERRS spectrum reveals that the B capture probe detects subtype B viral RNA, but not subtype C viral RNA from culture supernatant.

lently linked on the slides. The resulting SERRS spectrum obtained from specific B capture-probe assay is shown in Figure 6.5. To test the reproducibility, we have performed the experiments on two copies of the same sample, whose data are represented by the two columns in Figure 6.5. It is clearly evident that the SERRS signal arises only when the capture probe and the subtypes are precisely matched (virus B in the present case). We obtain a flat, noisy signal for the case of virus C, which highlights the specificity of the assay.

The data from figures 6.4 and 6.5 collectively provide proof that our novel strategy can detect the viral RNA without amplification. This is probably the first attempt to develop a viral diagnostic technique that employs molecular diagnostics

coupled to SERRS.

When compared to conventional molecular biology techniques, our SERRS method has the following advantages:

- Does not require template amplification. False positive results are avoided. Economically inexpensive.
- Broader range. A large number of capture probes can target several windows within the virus and essentially every viral subtype can be included in the detection strategy.
- Highly sensitive detection. The reporter probe is conjugated to a Raman reporter hence exploiting the phenomenon of SERS or SERRS there by a single molecule detection should be possible theoretically. Also, the problem of photo-bleaching has least interference in SERRS measurements.

Application of Raman reporters also offer the advantage of employing low output gas lasers and/or diode lasers that are less expensive as opposed to more expensive high quality lasers employed in the fluorescent technology. Technically, a less complicated and less expensive equipment could be designed.

6.4 Conclusions

We have developed a new strategy for HIV-1 subtype detection by harnessing the SERRS phenomena. Our strategy of microarray capture of the nucleic acid template blended with SERRS-mediated detection can have wider global application where HIV-1 infections are common. The diverse viral subtypes of HIV-1, presently known recombinant viruses and recombinant strains that may arise in future can be efficiently detected by this method. Determination of the HIV-1

molecular nature will be important in the following areas and can have significant impact on treatment decisions, and intervention strategies.

- Basic research where determination of the subtype and/or recombinant nature of viruses is required.
- Drug therapy, where drug resistant mutants should be quickly identified.
- Vaccine studies, where a knowledge of the viral strains in a given population or geographical region is essential.

Importantly, the strategy we have developed can have a universal application where genetic diversity is a serious problem with other infectious organisms including HIV-2, Influenza, Polio, HBV, HCV, Dengue, Tuberculosis, malaria and others. Our strategy is technically less complicated, and can find broader application in resource poor conditions.

CHAPTER 7

OUTLOOK

The emerging field of optical spectroscopy has redefined the benchmark for molecular detection capabilities. Techniques like SERS, Fluorescence Resonance Energy Transfer (FRET) and Surface Plasmon Resonance (SPR) have emerged as effective probes of single molecules in confined volumes. New limits of resolution have been set and renewed due to the advances in microscopy. Methodologies like coupling the scanning probe microscopy or atomic force microscopy with optical schemes have resulted in techniques like Tip enhanced Raman Scattering, Scanning near-field Fluorescence microscopy and many more. All these advancements have resulted in better understanding of nanosystems, both biological and otherwise. The avenues for using modern optical techniques are plenty. Due to the sub-wavelength imaging capabilities, open problems like understanding the dynamics of macromolecules at cellular level, optical properties of nanosystems etc., can be addressed with greater accuracy. Especially in techniques like SERS, which have a unique blend of single molecule sensitivity with chemical imaging capabilities can be harnessed to address interesting problems which are not viable to other techniques.

7.1 Fundamental issues

Although SERS and SERRS have been effectively employed in various analytical applications, the fundamental physics of SERS as an optical process is yet to be understood completely. An active debate on this phenomenon was topic of a recent *Faraday Discussion* [130, 131]. Various groups around the world are trying build effective microscopic models to understand the electromagnetic and chemical enhancement mechanisms. The mechanism of vibrational pumping is one such attempt which has effectively explained some peculiar observations in SERS. Attempts have been made to precisely define the Raman cross section of molecules exhibiting SERS. This is important because the insight into the process of SERS lies in the enhanced interaction between molecule and metal, and one way to understand this is to precisely define the cross section of the scattering molecule. Another important issue in SERS is the calculation of absolute enhancement factors. Etchegoin and coworkers have performed an in-depth study of SERS enhancement factors (EFs) and cross-sections [132], including several issues often overlooked. Accurate experimental determination of single molecule enhancement factors using bi-analyte SERS and temperature dependent SERS vibrational pumping have been performed by them, which is a significant advancement in the field. It has been demonstrated that EFs as low as 10^7 , as opposed to the figure of 10^{14} often claimed in the literature, are sufficient for the observation of single molecule SERS signals, with maximum single molecule EFs typically of the order 10^{10} [132]. At the same time, Ozaki and coworkers have experimentally shown [133] second enhancement in surface-enhanced resonance Raman scattering by an analysis of anti-Stokes and Stokes Raman spectra. They show evidences of *twofold* electromagnetic (EM) enhancement in SERRS that exhibits an enhancement factor of up to 10^{14} which

has been analyzed by comparing SERRS spectra and plasmon resonance Rayleigh scattering spectra. They identify that SERRS spectral variations are induced by selective enhancement of SERRS bands whose maxima are close to plasmon resonance maxima. The correlation between the selective enhancement of SERRS and the plasmon energy demonstrated that the variations in SERRS spectra are induced by second EM enhancement in SERRS as a result of coupling between scattering photons and plasmons [133]. All these explanation has added a new dimension to the understanding of SERS phenomenon at the fundamental level, but by no means a comprehensive one [134–139]. Further research on these lines find great importance in understanding the physics behind SERS.

With an application point of view, there are various issues in SERS which have to be addressed in future. The rational design and fabrication of SERS hot-spot, effective coupling of magnetic properties of nanoparticle to their surface plasmon resonances, micro-fluidic instrumentation for SERS applications, Raman imaging of sub-cellular components are few of the examples which have direct or indirect implications in various analytical applications. Fabricating SERS substrates by both top-down and bottom-up approaches are needed to be addressed with greater concern. With the help of developing technology and better understanding of physical and chemical processes at nanoscale, all the above mentioned ideas can be conceived and materialized in future.

Thus, I conclude this thesis on an optimistic note that SERS has enormous potential to probe various aspects of materials and molecules alike, and I hope that new scientific avenues will be ventured in the coming future using effective optical probes like SERS.

References

- [1] C. V. Raman and K. S. Krishnan, *A new type of secondary radiation*, Nature **121**, 501 (1928).
- [2] D. A. Long, *Raman Spectroscopy* (McGraw-Hill, London, 1977).
- [3] J. R. Lakowicz, *Principles of Fluorescence Spectroscopy* (Kluwer, Norwell, 1999).
- [4] W. Demtroeder, in *Laser Spectroscopy*, 3rd ed. (Springer, Germany, 2003), pp. 524–525.
- [5] M. Manfait and I. Nabiev, *Raman Microscopy* (Academic Press, St. Louis, 1996).
- [6] M. Moskovits, *Surface-enhanced spectroscopy*, Rev. Mod. Phys. **57**, 783 (1985).
- [7] A. Campion and P. Kambhampati, *Surface-enhanced Raman scattering*, Chem. Soc. Rev. **27**, 241 (1998).
- [8] M. Fleischmann, P. J. Hendra, and A. J. McQuillan, *Raman spectra of pyridine adsorbed at a silver electrode*, Chem. Phys. Lett. **26**, 163 (1974).

- [9] M. G. Albrecht and J. A. Creighton, *Anomalously intense Raman spectra of pyridine at a silver electrode*, J. Am. Chem. Soc. **99**, 5215 (1977).
- [10] D. L. Jeanmaire and R. P. VanDuyne, *Surface Raman Spectroelectrochemistry. Part I. Heterocyclic, Aromatic, and Aliphatic Amines Adsorbed on the Anodized Silver Electrode*, J. Electroanal. Chem. **84**, 1 (1977).
- [11] K. Kneipp *et al.*, *Single molecule detection using surface-enhanced Raman scattering (SERS)*, Phy. Rev. Lett. **78**, 1667 (1997).
- [12] S. Nie and S. R. Emory, *Probing single molecules and single nanoparticles by surface-enhanced Raman scattering*, Science **275**, 1102 (1997).
- [13] D. Graham, B. J. Mallinder, and W. E. Smith, *Surface-enhanced resonance Raman scattering as a novel method of DNA discrimination*, Angew. Chem. Int. Ed. **39**, 1061 (2000).
- [14] B. D. Moore *et al.*, *Rapid and ultra-sensitive determination of enzyme activities using surface-enhanced resonance Raman scattering*, Nature Biotech. **22**, 1133 (2004).
- [15] E. Podstawka, Y. Ozaki, and L. M. Proniewicz, *Part I: Surface-enhanced Raman spectroscopy investigation of amino acids and their homodipeptides adsorbed on colloidal silver*, Appl. Spectrosc. **58**, 570 (2004).
- [16] S. Stewart and P. M. Fredericks, *Surface-enhanced Raman spectroscopy of peptides and proteins adsorbed on an electrochemically prepared silver surface*, Spectrochim. Acta - Part A **55**, 1615 (1999).

- [17] E. Podstawka, Y. Ozaki, and L. M. Proniewicz, *Adsorption of S-S containing proteins on a colloidal silver surface studied by surface-enhanced Raman spectroscopy*, *Appl. Spectrosc.* **58**, 1147 (2004).
- [18] G. Fabriciova, S. Sanchez-Cortes, J. V. Garcia-Ramos, and P. Miskovsky, *Surface-Enhanced Raman Spectroscopy Study of the Interaction of the Antitumoral Drug Emodin with Human Serum Albumin*, *Biopolymers* **74**, 125 (2004).
- [19] M. Ermishov *et al.*, *Raman and surface-enhanced Raman scattering spectroscopy of bis-netropsins and their DNA complexes*, *Biopolymers* **57**, 272 (2000).
- [20] S. Streltsov *et al.*, *Interaction of Clinically Important Human DNA Topoisomerase I Poison, Topotecan, with Double-Stranded DNA*, *Biopolymers* **72**, 442 (2003).
- [21] A. Otto, I. Mrozek, H. Grabhorn, and W. Akemann, *Surface-enhanced Raman scattering*, *J. Phys.: Condens. Matter* **4**, 1143 (1992).
- [22] R. F. Aroca *et al.*, *Surface-enhanced Raman scattering on colloidal nanostructures*, *Adv. Colloid Interface Sci.* **116**, 45 (2005).
- [23] R. Aroca, *Surface Enhanced Vibrational Spectroscopy* (Wiley, West Sussex, 2006).
- [24] G. A. Baker and D. S. Moore, *Progress in plasmonic engineering of surface-enhanced Raman-scattering substrates toward ultra-trace analysis*, *Anal. Bioanal. Chem.* **382**, 1751 (2005).

- [25] T. R. Jensen, M. D. Malinsky, C. L. Haynes, and R. P. VanDuyne, *Nanosphere lithography: Tunable localized surface plasmon resonance spectra of silver nanoparticles*, J. Phys. Chem. B **104**, 10549 (2000).
- [26] T. R. Jensen *et al.*, *Nanosphere lithography: Effect of the external dielectric medium on the surface plasmon resonance spectrum of a periodic array of silver nanoparticles*, J. Phys. Chem. B **103**, 9846 (1999).
- [27] T. Bhuvana, G. V. P. Kumar, G. U. Kulkarni, and C. Narayana, *Carbon assisted electroless gold for surface enhanced raman scattering studies*, J. Phy. Chem. C **111**, 6700 (2007).
- [28] Z. Zhu, T. Zhu, and Z. Liu, *Raman scattering enhancement contributed from individual gold nanoparticles and interparticle coupling*, Nanotechnology **15**, 357 (2004).
- [29] P. C. Lee and D. Meisel, *Adsorption and surface-enhanced Raman of dyes on silver and gold sols*, J. Phys. Chem. **86**, 3391 (1982).
- [30] J. A. Creighton, C. G. Blatchford, and M. G. Albrecht, *Plasma resonance enhancement of Raman scattering by pyridine adsorbed on silver or gold sol particles of size comparable to the excitation wavelength*, J. Chem. Soc., Faraday Trans. II **75**, 790 (1979).
- [31] T. M. Cotton, S. G. Schultz, and R. P. Van Duyne, *Surface-enhanced resonance Raman scattering from cytochrome c and myoglobin adsorbed on a silver electrode*, J. Am. Chem. Soc. **102**, 7960 (1980).
- [32] X. Dou *et al.*, *Enzyme Immunoassay Utilizing Surface-Enhanced Raman Scattering of the Enzyme Reaction Product*, Anal. Chem. **69**, 1492 (1997).

- [33] X. Huang, I. H. El-Sayed, W. Qian, and M. A. El-Sayed, *Cancer cells assemble and align gold nanorods conjugated to antibodies to produce highly enhanced, sharp, and polarized surface Raman spectra: A potential cancer diagnostic marker*, *Nano Lett.* **7**, 1591 (2007).
- [34] S. Lee *et al.*, *Biological imaging of HEK293 cells expressing PLC β 1 using surface-enhanced raman microscopy*, *Anal. Chem.* **79**, 916 (2007).
- [35] K. Kneipp, H. Kneipp, and J. Kneipp, *Surface-enhanced raman scattering in local optical fields of silver and gold nanoaggregates - From single-molecule raman spectroscopy to ultrasensitive probing in live cells*, *Acc. Chem. Res.* **39**, 443 (2006).
- [36] K. Kneipp *et al.*, *Surface-enhanced raman spectroscopy in single living cells using gold nanoparticles*, *Appl. Spectrosc.* **56**, 150 (2002).
- [37] D. A. Stuart *et al.*, *In vivo glucose measurement by surface-enhanced Raman spectroscopy*, *Anal. Chem.* **78**, 7211 (2006).
- [38] K. E. Shafer-Peltier, C. L. Haynes, M. R. Glucksberg, and R. P. VanDuyne, *Toward a glucose biosensor based on surface-enhanced Raman scattering*, *J. Am. Chem. Soc.* **125**, 588 (2003).
- [39] M. Kahraman *et al.*, *Reproducible surface-enhanced Raman scattering spectra of bacteria on aggregated silver nanoparticles*, *Appl. Spectrosc.* **61**, 479 (2007).
- [40] R. M. Jarvis, A. Brooker, and R. Goodacre, *Surface-enhanced Raman scattering for the rapid discrimination of bacteria*, *Faraday Discussions* **132**, 281 (2006).

- [41] W. R. Premasiri *et al.*, *Characterization of the Surface Enhanced Raman Scattering (SERS) of bacteria*, J. Phys. Chem. B **109**, 312 (2005).
- [42] K. Kneipp *et al.*, *Surface-enhanced Raman scattering and biophysics*, J. Phys.: Condens. Matter **14**, (2002).
- [43] J. A. Dieringer *et al.*, *Surface enhanced Raman spectroscopy: New materials, concepts, characterization tools, and applications*, Faraday Discussions **132**, 9 (2006).
- [44] C. M. Stellman, K. S. Booksh, J. E. Reddic, and M. L. Myrick, *Description and performance of a highly versatile, low-cost fiber-optic confocal Raman microscope*, Rev. Sci. Instrum. **67**, 79 (1996).
- [45] K. E. Shafer-Peltier *et al.*, *Raman microspectroscopic model of human breast tissue: Implications for breast cancer diagnosis in vivo*, J. Raman Spectrosc. **33**, 552 (2002).
- [46] F. LaPlant and D. Ben-Amotz, *Design and construction of a microscope-based Raman system*, Rev. Sci. Instrum. **66**, 3537 (1995).
- [47] M. Muniz-Miranda and G. Neto, N.and Sbrana, *Surface Enhanced Raman Scattering of Imidazole adsorbed onto Silver Colloidal Particles*, J. Mol. Struct. **267**, 281 (1992).
- [48] P. Hildebrandt and M. Stockhurger, *Surface-Enhanced Resonance Raman Spectroscopy of Rhodamine 6G adsorbed on colloidal silver*, J. Phys. Chem. **88**, 5935 (1984).
- [49] P. Etchegoin *et al.*, *Observation of dynamic oxygen release in hemoglobin using surface enhanced Raman scattering*, Chem. Phys. Lett. **367**, 223 (2003).

- [50] T. T. Chen, C. S. Kuo, Y. C. Chou, and N. T. Liang, *Surface-enhanced Raman scattering of adenosine triphosphate molecules*, *Langmuir* **5**, 887 (1989).
- [51] A. R. Bizzarri and S. Cannistraro, *Surface-enhanced resonance Raman spectroscopy signals from single myoglobin molecules*, *Appl. Spectrosc.* **56**, 1531 (2002).
- [52] H. B. Ghodke *et al.*, *The I-tetraplex building block: Rational design and controlled fabrication of robust 1D DNA scaffolds through non-Watson-Crick interactions*, *Angew. Chem. Int. Ed.* **46**, 2645 (2007).
- [53] K. Mantelingu *et al.*, *Specific Inhibition of p300-HAT Alters Global Gene Expression and Represses HIV Replication*, *Chem. Bio.* **14**, 645 (2007).
- [54] K. Mantelingu *et al.*, *Activation of p300 histone acetyltransferase by small molecules altering enzyme structure: Probed by surface-enhanced raman spectroscopy*, *J. Phy. Chem. B* **111**, 4527 (2007).
- [55] T. Bhuvana, G. V. P. Kumar, C. Narayana, and G. U. Kulkarni, *Nanogranular Au films deposited on carbon covered Si substrates for enhanced optical reflectivity and Raman scattering*, *Nanotechnology* **18**, 145702 (2007).
- [56] G. V. P. Kumar *et al.*, *Hot spots in Ag core-Au shell nanoparticles potent for surface-enhanced Raman scattering studies of biomolecules*, *J. Phy. Chem. C* **111**, 4388 (2007).
- [57] G. V. P. Kumar *et al.*, *Surface-enhanced raman scattering studies of human transcriptional coactivator p300*, *J. Phy. Chem. C* **110**, 16787 (2007).

- [58] Y. Cui *et al.*, *Synthesis of AgcoreAushell bimetallic nanoparticles for immunoassay based on surface-enhanced Raman spectroscopy*, J. Phys. Chem. B **110**, 4002 (2006).
- [59] E. Prodan and P. Nordlander, *Structural tunability of the plasmon resonances in metallic nanoshells*, Nano Lett. **3**, 543 (2003).
- [60] L. Qin *et al.*, *Designing, fabricating, and imaging Raman hot spots*, Proc. Natl. Acad. Sci. U.S.A. **103**, 13300 (2006).
- [61] S. J. Lee, A. R. Morrill, and M. Moskovits, *Hot spots in silver nanowire bundles for surface-enhanced Raman spectroscopy*, J. Am. Chem. Soc. **128**, 2200 (2006).
- [62] H. Wang, C. S. Levin, and N. J. Halas, *Nanosphere arrays with controlled sub-10-nm gaps as surface-enhanced Raman spectroscopy substrates*, J. Am. Chem. Soc. **127**, 14992 (2005).
- [63] E. Hao *et al.*, *Optical properties of metal nanoshells*, J. Phys. Chem. B **108**, 1224 (2004).
- [64] R. A. Alvarez-Puebla, D. J. Ross, G. Nazri, and R. F. Aroca, *Surface-enhanced Raman scattering on nanoshells with tunable surface plasmon resonance*, Langmuir **21**, 10504 (2005).
- [65] I. Srnova-S, loufova, F. Lednický, A. Gemperle, and J. Gemperlova, *Core-shell (Ag)Au bimetallic nanoparticles: analysis of transmission electron microscopy images*, Langmuir **16**, 9928 (2000).
- [66] C. Genet and T. W. Ebbesen, *Light in tiny holes*, Nature **445**, 39 (2007).

- [67] J. Wenger *et al.*, *Raman scattering and fluorescence emission in a single nanoaperture: Optimizing the local intensity enhancement*, Opt. Comm. **267**, 224 (2006).
- [68] E. Popov *et al.*, *Field enhancement in single subwavelength apertures*, J. Opt. Soc. Am. A **23**, 2342 (2006).
- [69] J. Dintinger, S. Klein, and T. W. Ebbesen, *Molecule-surface plasmon interactions in hole arrays: Enhanced absorption, refractive index changes, and all-optical switching*, Adv. Mater. **18**, 1267 (2006).
- [70] R. M. Stockle, Y. D. Suh, V. Deckert, and R. Zenobi, *Nanoscale chemical analysis by tip-enhanced Raman spectroscopy*, Chem. Phys. Lett. **318**, 131 (2000).
- [71] N. Hayazawa, Y. Inouye, Z. Sekkat, and S. Kawata, *Near-field Raman scattering enhanced by a metallized tip*, Chem. Phys. Lett. **335**, 369 (2001).
- [72] B. Pettinger *et al.*, *Nanoscale probing of adsorbed species by tip-enhanced Raman spectroscopy*, Phys. Rev. Lett. **92**, 096101 (2004).
- [73] J. R. Lakowicz, *Radiative decay engineering 5: Metal-enhanced fluorescence and plasmon emission*, Anal. Biochem. **337**, 171 (2005).
- [74] G. K. Kouassi and J. Irudayaraj, *Magnetic and gold-coated magnetic nanoparticles as a DNA sensor*, Anal. Chem. **78**, 3234 (2006).
- [75] M. Mandal *et al.*, *Magnetite nanoparticles with tunable gold or silver shell*, J. Colloid Interface Sc. **286**, 187 (2005).
- [76] J. L. Lyon *et al.*, *Synthesis of Fe oxide Core/Au shell nanoparticles by iterative hydroxylamine seeding*, Nano Lett. **4**, 719 (2004).

- [77] D. W. Mayo, F. A. Miller, and R. W. Hannah, *Course notes on the interpretation of Infrared and Raman spectra* (Wiley-Interscience, Germany, 2004).
- [78] R. C. Maher *et al.*, *Temperature-dependent anti-stokes/stokes ratios under surface-enhanced Raman scattering conditions*, J.Phys. Chem. B **110**, 6797 (2006).
- [79] C. Kim, J. H. Sim, X. Yan, and J. M. White, *Thermal reactions of 2-naphthalenethiol adsorbed on Ag(111)*, Langmuir **18**, 3159 (2002).
- [80] G. M. Whitesides and B. Grzybowski, *Self-assembly at all scales*, Science **295**, 2418 (2002).
- [81] M. Pileni, *Magnetic fluids: Fabrication, magnetic properties, and organization of nanocrystals*, Adv. Func. Mater. **11**, 323 (2001).
- [82] D. Gatteschi, *Molecular magnetism: A basis for new materials*, Adv. Mater. **6**, 635 (1994).
- [83] P. D. Hallett, A. R. Dexter, and J. P. K. Seville, *The application of fracture mechanics to crack propagation in dry soil*, Eur. J. Soil Sci. **46**, 591 (1995).
- [84] E. Rabani, D. R. Reichman, P. L. Geissler, and L. E. Brus, *Drying-mediated self-assembly of nanoparticles*, Nature **426**, 271 (2003).
- [85] M. Seul and D. Andelman, *Domain shapes and patterns: The phenomenology of modulated phases*, Science **267**, 476 (1995).
- [86] Y. Sahoo *et al.*, *Field-directed self-assembly of magnetic nanoparticles*, J. Phys. Chem. B **108**, 3380 (2004).

- [87] M. Tanase *et al.*, *Assembly of multicellular constructs and microarrays of cells using magnetic nanowires*, Lab Chip **5**, 598 (2005).
- [88] K. Balasubramanyam, V. Swaminathan, A. Ranganathan, and T. K. Kundu, *Small molecule modulators of histone acetyltransferase p300*, J. Bio. Chem. **278**, 19134 (2003).
- [89] A. J. Bannister and T. Kouzarides, *The CBP co-activator is a histone acetyltransferase*, Nature **384**, 641 (1996).
- [90] H. M. Chan and N. B. LaThangue, *p300/CBP proteins: HATs for transcriptional bridges and scaffolds*, J. Cell Sci. **114**, 2363 (2001).
- [91] Y. Wang, Y. Li, Z. Zhang, and D. An, *Surface-enhanced Raman scattering of some water insoluble drugs in silver hydrosols*, Spectrochim. Acta - Part A **59**, 589 (2003).
- [92] L. Huang *et al.*, *A simple method for measuring the SERS spectra of water-insoluble organic compounds*, Vib. Spectrosc. **26**, 15 (2001).
- [93] M. J. Frisch *et al.*, , Gaussian 98 (1995).
- [94] P. K. Kim, S. L. Hsu, and H. Ishida, *Normal vibrational analysis of benzanilide. A model for poly(p-phenylene terephthalamide)*, Macromolecules **18**, 1905 (1985).
- [95] C. Zuo and P. W. Jagodzinski, *Surface-enhanced raman scattering of pyridine using different metals: Differences and explanation based on the selective formation of pyridyl on metal surfaces*, J. Phys. Chem. B **109**, 1788 (2005).

- [96] J. Sarkar *et al.*, *Experimental and theoretical surface enhanced raman scattering study of 2-amino-4-methylbenzothiazole adsorbed on colloidal silver particles*, J. Phys. Chem. B **109**, 22536 (2005).
- [97] J. Sarkar *et al.*, *Adsorption of 2-aminobenzothiazole on colloidal silver particles: An experimental and theoretical surface-enhanced Raman scattering study*, J. Phys. Chem. B **109**, 12861 (2005).
- [98] V. M. Hallmark and A. Campion, *Selection rules for surface Raman spectroscopy: Experimental results*, J. Chem. Phys. **84**, 2933 (1986).
- [99] M. Moskovits, *Surface selection rules*, J. Chem. Phys. **77**, 4408 (1982).
- [100] R. H. Giles, D. J. M. Peters, and M. H. Breuning, *Conjunction dysfunction: CBP/p300 in human disease*, Trends Genet. **14**, 178 (1998).
- [101] R. Eckner *et al.*, *Molecular cloning and functional analysis of the adenovirus E1A-associated 300-kD protein (p300) reveals a protein with properties of a transcriptional adaptor*, Genes Dev. **8**, 869 (1994).
- [102] A. Giordano and M. L. Avantaggiati, *p300 and CBP: Partners for life and death*, J. Cell. Physiol. **181**, 218 (1999).
- [103] R. H. Goodman and S. Smolik, *CBP/p300 in cell growth, transformation, and development*, Genes Dev. **14**, 1553 (2000).
- [104] A. J. Bannister and T. Kouzarides, *The CBP co-activator is a histone acetyltransferase*, Nature **384**, 641 (1996).
- [105] V. V. Ogryzko *et al.*, *The transcriptional coactivators p300 and CBP are histone acetyltransferases*, Cell **87**, 953 (1996).

- [106] N. G. Iyer, H. Ozdag, and C. Caldas, *p300/CBP and cancer*, *Oncogene* **23**, 4225 (2004).
- [107] C. Das and T. K. Kundu, *Transcriptional regulation by the acetylation of nonhistone proteins in humans - A new target for therapeutics*, *IUBMB Life* **57**, 137 (2005).
- [108] V. Swaminathan, A. H. Kishore, K. K. Febitha, and T. K. Kundu, *Human histone chaperone nucleophosmin enhances acetylation-dependent chromatin transcription*, *Mol. Cell. Bio.* **25**, 7534 (2005).
- [109] R. A. Varier, V. Swaminathan, K. Balasubramanyam, and T. K. Kundu, *Implications of small molecule activators and inhibitors of histone acetyltransferases in chromatin therapy*, *Biochem. Pharmacol.* **68**, 1215 (2004).
- [110] R. Tuma, P. E. Prevelige Jr., and G. J. Thomas Jr., *Mechanism of capsid maturation in a double-stranded DNA virus*, *Proc. Natl. Acad. Sci. U.S.A.* **95**, 9885 (1998).
- [111] G. D. Chumanov, R. G. Efremov, and I. R. Nabiev, *Surface-enhanced Raman spectroscopy of biomolecules*, *J. Raman Spectrosc.* **21**, 43 (1990).
- [112] E. S. Grabbe and R. P. Buck, *Surface-enhanced raman spectroscopic investigation of human immunoglobulin G adsorbed on a silver electrode*, *J. Am. Chem. Soc.* **111**, 8362 (1989).
- [113] Y. Li, Y. Wang, and J. Cheng, *Interaction effects on surface-enhanced Raman scattering activities in silver sols*, *Vib. Spectrosc.* **27**, 65 (2001).
- [114] O. D. Lau *et al.*, *HATs off: Selective synthetic inhibitors of the histone acetyltransferases p300 and PCAF*, *Mol. Cell* **5**, 589 (2000).

- [115] K. Balasubramanyam *et al.*, *Curcumin, a novel p300/CREB-binding protein-specific inhibitor of acetyltransferase, represses the acetylation of histone/nonhistone proteins and histone acetyltransferase-dependent chromatin transcription*, J. Bio. Chem. **279**, 51163 (2004).
- [116] K. Balasubramanyam *et al.*, *Polyisoprenylated benzophenone, garcinol, a natural histone acetyltransferase inhibitor, represses chromatin transcription and alters global gene expression*, J. Bio. Chem. **279**, 33716 (2004).
- [117] L. Stimson *et al.*, *Isothiazolones as inhibitors of PCAF and p300 histone acetyltransferase activity*, Mol. Cancer Therapeutics **4**, 1521 (2005).
- [118] S. Y. Roth, J. M. Denu, and C. D. Allis, *Histone acetyltransferases*, Ann. Rev. Biochem. **70**, 81 (2001).
- [119] S. L. Berger, *Histone modifications in transcriptional regulation*, Curr. Opin. Genet. Dev. **12**, 142 (2002).
- [120] M. Chevillard-Briet, D. Trouche, and L. Vandel, *Control of CBP co-activating activity by arginine methylation*, EMBO J. **21**, 5457 (2002).
- [121] D. Girdwood *et al.*, *p300 transcriptional repression is mediated by SUMO modification*, Mol. Cell **11**, 1043 (2003).
- [122] M. Arif, G. V. P. Kumar, C. Narayana, and T. K. Kundu, *Surface-enhanced raman scattering studies of human transcriptional coactivator p300*, J. Phy. Chem. B **111**, 11877 (2007).
- [123] <http://hiv web.lanl.gov>, *National Institutes of Health*, (2007).
- [124] <http://hiv-web.lanl.gov/content/hiv db/CRFs/CRFs.html>, *National Institutes of Health*, (2007).

- [125] R. Najera, E. Delgado, L. Perez-Alvarez, and M. M. Thomson, *Genetic recombination and its role in the development of the HIV-1 pandemic*, AIDS **16**, S3 (2002).
- [126] R. B. Lal, S. Chakrabarti, and C. Yang, *Impact of genetic diversity of HIV1 on diagnosis, antiretroviral therapy and vaccine development*, Indian J. Med. Res. **121**, 287 (2005).
- [127] B. Joos, H. Kuster, and R. Cone, *Covalent attachment of hybridizable oligonucleotides to glass supports*, Anal. Biochem. **247**, 96 (1997).
- [128] Z. Guo *et al.*, *Direct fluorescence analysis of genetic polymorphisms by hybridization with oligonucleotide arrays on glass supports*, Nucleic Acids Res. **22**, 5456 (1994).
- [129] N. Kimura, R. Oda, Y. Inaki, and O. Suzuki, *Attachment of oligonucleotide probes to poly carbodiimide-coated glass for microarray applications.*, Nucleic acids res. **32**, (2004).
- [130] J. A. Dieringer *et al.*, *Surface enhanced Raman spectroscopy: New materials, concepts, characterization tools, and applications*, Faraday Discuss. **132**, 9 (2006).
- [131] M. J. Natan, *Concluding remarks: Surface enhanced Raman scattering*, Faraday Discuss. **132**, 321 (2006).
- [132] E. C. Le Ru, E. Blackie, M. Meyer, and P. G. Etchegoint, *Surface enhanced raman scattering enhancement factors: A comprehensive study*, J. Phys. Chem. C **111**, 13794 (2007).

-
- [133] T. Itoh *et al.*, *Second enhancement in surface-enhanced resonance Raman scattering revealed by an analysis of anti-Stokes and Stokes Raman spectra*, Phys. Rev. B **76**, (2007).
- [134] T. H. Wood, *Role of atomic-scale roughness in surface-enhanced Raman scattering*, Phys. Rev. B **24**, 2289 (1981).
- [135] A. Otto, *Comment on - Role of atomic-scale roughness in surface-enhanced Raman scattering*, Phys. Rev. B **27**, 5132 (1983).
- [136] T. H. Wood, *Reply to comment on - Role of atomic-scale roughness in surface-enhanced Raman scattering*, Phys. Rev. B **27**, 5137 (1983).
- [137] J. I. Gersten, *The effect of surface roughness on surface enhanced Raman scattering*, J. Chem. Phys. **72**, 5779 (1980).
- [138] M. Moskovits, *Surface roughness and the enhanced intensity of Raman scattering by molecules adsorbed on metals*, J. Chem. Phys. **69**, 4159 (1978).
- [139] E. C. Le Ru, P. G. Etchegoin, and M. Meyer, *Enhancement factor distribution around a single surface-enhanced Raman scattering hot spot and its relation to single molecule detection*, J. Chem. Phys. **125**, 204701 (2006).